

Université
de Liège



Faculty of Sciences
Physics department

Surface tension and buoyancy in vertical soap films



Dissertation presented by

Nicolas ADAMI

to obtain the grade of
Doctor in Sciences

Academic year 2013-2014

Remerciements

Bien que ce manuscrit soit dédié aux travaux réalisés durant ma thèse, je ne peux m'empêcher de le commencer en exprimant quelques remerciements.

Tout d'abord, je tiens à remercier Yves Couder, José Bico, Alejandro Silhanek et Stéphane Dorbolo d'avoir accepté de faire partie du jury en charge d'évaluer nos travaux.

Je tiens ensuite à vivement remercier Hervé Caps, mon promoteur de thèse, pour l'encadrement qu'il m'a apporté au cours de ces quatre dernières années. Hervé s'est toujours montré très disponible et à l'écoute vis-à-vis des différents défis que nous nous sommes proposé de relever. Tout en me guidant, il m'a toujours laissé libre de développer mes propres idées, tant au niveau expérimental que théorique, m'apportant ainsi un encadrement très formateur vis-à-vis du métier d'apprenti chercheur. Il m'a appris et aidé à développer la physique autant "à la main" que de manière plus formelle, assurant ainsi une description complète des divers phénomènes considérés. A la base, Hervé et moi avons des personnalités et caractères assez différents, si bien qu'au début, il m'est arrivé de douter de mon choix de travailler avec lui. Cependant, tout au long de ces quatre années, je n'ai pu que constater et apprécier ses qualités morales, et surtout humaines. Hervé est honnête, juste, modeste et gentil. Il sait être magnanime sans pour autant pratiquer la langue de bois et surtout, il accorde le bénéfice du doute aux gens, ce qui, à notre époque, est une des qualités les plus remarquable. En plus de ses compétences scientifiques, ces diverses qualités en font un promoteur objectif et dévoué. Ca a été, et ça sera toujours, un plaisir de travailler avec lui. Hervé, merci pour tout.

Je tiens aussi à remercier particulièrement Stéphane Dorbolo. Bien qu'il ne soit pas promoteur de mes travaux, Stéphane a toujours été ouvert aux diverses discussions liées à nos expériences. Au delà des expériences présentées dans le présent manuscrit, il a toujours été ouvert à discuter de ses travaux en cours, de travaux réalisés par des collègues provenant d'autres laboratoires, de résultats

découverts en conférences... Stéphane et moi avons des manières très différentes d'aborder un même phénomène physique, ce qui a eu pour conséquence de parfois mener à des "dialogues de sourds". Quoi qu'il en soit, j'en suis toujours venu à la conclusion qu'une fois décortiquée, sa vision des choses est toujours particulièrement originale et pertinente. Avec le temps, j'ai appris à comprendre, et même un peu à parler la "physique en Dorbolo", ce qui aura été des plus enrichissant pour moi. Même si je sais bien qu'il sera toujours plus fort que moi en répliques de films cultes ("quant on tire, on ne raconte pas sa vie", réplique de Tuco dans Le bon, la brute et le truand, est sa préférée), je ne désespère pas d'un jour atteindre son niveau. Thanks man!

Je remercie également José Bico et Benoit Roman, qui m'ont très aimablement accueilli au sein de leur équipe durant quatre mois. Ce séjour a été pour moi l'occasion de travailler dans un environnement différent de celui auquel je suis habitué, ainsi que d'aborder un sujet différent de celui lié à ma thèse. Ils m'ont ainsi initié à l'élasticité des matériaux solides, aux travers d'expériences décrites au troisième chapitre de ce manuscrit. Comme vous pourrez le lire, cette initiation m'a permis de développer une expérience capitale vis-à-vis des films de savons, ainsi que de découvrir une thématique de recherche amusante, et qui me plaît beaucoup. Merci à vous deux.

Merci à tous les membres du GRASP pour leur bonne humeur, conversations, discussion de couloirs et de coins de tables, temps de midi (bières spéciales et autres)... De manière générale, le GRASP est un laboratoire formé de gens à la fois très compétents et ne se prenant pas trop au sérieux. Ainsi, il est facile d'y plaisanter à longueur de journée tout en travaillant, ce qui procure une ambiance unique et détendue, qui fait qu'on se lève rarement avec les pieds de plomb pour y aller. Merci à Hervé, Stéphane, Geoffroy et Nicolas, les membres permanents, qui permettent de part leur nature aux chercheurs en tout genre d'exister dans le labo.

Le GRASP, c'est également une petite communauté caractérisée par divers histoires et personnages haut en couleur. Je pense notamment à Médéric, le décapsuleur universel, ou encore Martin, le vigneron. Merci donc à Laurent, Julien, Maxime, Ariane, Charles, Martin, Metal, François, Eric, Martial, Médéric, Samuel, Florian et Côte. Merci aussi à ceux qui ne travaillent plus au labo mais qu'on oublie quand même pas, Denis, Eric, Giles, Florian, Damien, Felipe, Ian... et j'en oublie sûrement. Merci à Giles, Charles et Martin, mes collègues de bureau, pour la sympathique cohabitation de ces dernières années. Merci aussi à Metal pour sa sympathie et ses toujours très bonnes pâtisseries.

On envisage difficilement un labo principalement peuplé d'expérimentateurs sans techniciens. Ce sont en effet ces as du tour, fraise et autres machines outils en tout genre qui rendent possible la création de dispositifs expérimentaux uniques, qu'il nous serait très souvent impossible de créer par nous même à partir de pièces disponibles dans le commerce. Merci à Jean-Claude Remy, Samuel Rondia et Florian Allegro pour l'usinage et la fabrication, toujours très minutieuse et adaptée à la demande, des différents dispositifs que j'ai utilisé tout au long de ma thèse. Merci à Médéric et Sébastien, nos techniciens électroniciens, pour leurs compétences et leur sympathie. Merci aussi Chouaib d'avoir assuré le bon fonctionnement des divers appareillages électroniques.

Merci aux amis qui ont toujours été présents pour me distraire. Merci aux gais lurons, avec qui il est toujours bien sympathique de passer un moment, une soirée... Je pense notamment à Thomas, Julien, René, Jordane, Jordan, Giles, Greg... j'en passe et des meilleurs. Merci également à mes compagnons d'études, que je côtoie depuis notre arrivée à l'université, et même parfois bien avant pour certains, Ariane, Audrey, Marjorie, Maité, René, Jean-Phillipe, Julien et Nicolas.

Je tiens aussi à remercier ma famille, et en particulier mes parents, qui m'ont toujours soutenu, et permis de faire mes études.

Merci enfin au FNRS pour avoir assuré l'entièreté de l'aspect financier lié à mes travaux. Merci aussi à l'Université de Liège pour la mise à disposition des locaux, ainsi que pour ses diverses participations financières.

N.B.A., Liège, Septembre 2013.

Contents

List of the works realized	v
Résumé	vii
Summary	ix
Introduction	1
1 State of the art	3
1.1 Size of a liquid	3
1.2 Surface tension	4
1.2.1 Laplace pressure	8
1.3 Surface tension variations	8
1.4 Surfactant molecules	9
1.4.1 Surfactants used in the present thesis experiments	10
1.4.2 Surface concentration and surface pressure	12
1.5 Adsorption layer and dynamical equilibrium	14
1.5.1 Critical micellar concentration (CMC)	14
1.5.2 Dynamical equilibrium at the interface	15
1.6 Monolayer elasticity	18
1.7 Soapy objects and curvature	20
1.7.1 Soap film thinning	22
1.7.2 Surface viscosity and interfacial equilibrium	24
1.8 Marginal regeneration	26
1.9 Some previous experiments	29
1.10 Position of the problem	33
2 Thickness profiles of fed soap films	35
2.1 Experimental setup	37
2.2 Soap film formation procedure	40
2.3 Thickness profiles of fed soap films	40
2.4 Infrared thickness measurements	44

2.4.1	Thermal camera	45
2.4.2	Quantitative characterization of thickness profiles	51
2.4.3	Velocity profiles	52
2.5	Conclusion	54
3	Surface tension profiles in soap films	55
3.1	Mechanical equilibrium in vertical soap films	55
3.2	Surface tension probe	59
3.2.1	Elasticity	59
3.2.2	Elastic polymer	60
3.2.3	Elasto-capillary and elasto-gravitary lengths	61
3.3	Surface tension probes in Langmuir tank	70
3.3.1	Rectangular probes : Langmuir tank calibration	71
3.4	Rectangular probe : soap film configuration	74
3.4.1	Deflection measurements	77
3.5	Conclusion	80
4	Two-dimensional buoyancy in vertical soap films	83
4.1	Context	83
4.2	Buoyancy in vertical soap films	85
4.3	Floating hair rings	86
4.3.1	Link with surface tension profiles	90
4.4	Dynamics of buoyant rings	92
4.4.1	Mass of the meniscus	94
4.4.2	Viscous drag	95
4.4.3	Lubrication of the meniscus	97
4.4.4	Dynamical analysis	98
4.5	Equilibrium height and effective mass	100
4.5.1	Liquid front and momentum	102
4.6	Floating rings trajectories	105
4.6.1	Critical ring radius	106
4.6.2	Discussion on the mass problem	107
4.6.3	Discussion on the interfacial viscous drag	109
4.7	Conclusion	111
5	Thermal plumes in vertical soap films	113
5.1	Thermal plumes	113
5.1.1	Thermal plumes in vertical soap films	114
5.2	Single thermal plumes in soap films	116
5.2.1	Experimental setup	116
5.2.2	Thermal rising criterion	122

5.3	Dynamics of thermal plumes in soap films	123
5.3.1	Marangoni effect	124
5.3.2	Three-dimensional buoyancy	124
5.3.3	Two-dimensional buoyancy	125
5.3.4	Viscous drag	127
5.3.5	Dynamical model for the heated particles	127
5.3.6	Dimensional estimations	129
5.3.7	Thermal plume trajectories	129
5.3.8	Comparison with the floating rings	133
5.4	Conclusion	135
	Conclusion and perspectives	137
	Bibliographie	147

List of the works realized

Here is a list of the experiments realized during my Phd thesis, in chronological order.

1 : Local thermal constraints on vertical soap films

Those experiments are presented in Chapter 5. The basic idea is to apply a local heating to vertical soap films and to investigate related thermal phenomena. We essentially focused on the study of the behaviors of thermal plumes produced by the heating. This study led to a paper, published in Physical Review E :

N. Adami, S. Dorbolo, H. Caps, *Single thermal plumes in locally heated soap films*, Phys. Rev. E **84**, 046316 (2011).

2 : Thickness measurements in fed soap films

Those experiments were realized in order to characterize soap film thickness profiles. They are fully described in Chapter 2 and in the paper mentioned in point 1.

3 : Bouncing magnet

Those experiments aimed to investigate the behavior of a magnet when submitted to the influence of oscillatory motions of an opposing magnet lying beneath. Those investigations were performed in order to check if chaotic behaviors can be obtained with interaction potentials which are smoother than the one linked to solid contact (bouncing ball). This study is still under investigation, and will be continued soon.

4 : Soft elastic objects submitted to surface pressure constraints

Those experiments were realized in Paris, with José Bico and Benoit Roman, and aimed to study the behaviors of soft deformable rings and rectangles once

submitted to the surface pressure of an ideal surfactant monolayer. Complete description of these experiments are presented in Chapter 3. They led to the following paper, which should be submitted for publication soon :

N. Adami, A. Delbos, B. Roman, J. Bico, *Elasto-capillary collapse of floating structures*, arXiv:1310.0329 [physics.flu-dyn].

5 : Surface tension measurements in vertical soap films

Those experiments were achieved in order to probe the surface tension profiles in fed vertical soap films. They use the results of experiments presented in point 2 and 4. Results are in agreement with thickness profiles measurements, as presented in Chapter 3. Those results led to the following paper :

N. Adami, H. Caps, *Surface tension profiles in vertical soap films*, arXiv:1310.0454 [physics.flu-dyn cond-mat.soft].

6 : Floating rings in vertical soap films

Those experiments were inspired by previous works of Couder and coworkers, and aimed to get insights on the buoyancy forces in fed soap films in function of experimental parameters. They led to the identification of buoyancy in soap films as being the resultant force of surface tension forces acting on soft light rings plugged in the films. The corresponding results appeared to be in good agreement with thickness and surface tension measurements. Those results led to the following paper :

N. Adami, H. Caps, *Floating rings in vertical soap films*, arXiv:1310.0320 [physics.flu-dyn].

Résumé

Depuis plusieurs décennies, les interfaces liquides liées aux solutions de surfactants font l'objet de nombreuses études. En effet, ces interfaces se retrouvent dans des systèmes physiques complexes tels que les mousses ou les émulsions. Ces mousses et ces émulsions sont de nos jours impliquées dans de nombreuses applications industrielles telles que la prospection pétrolière, la maîtrise d'incendies dans des situations précaires (sur ISS entre autres) ou encore l'isolation thermique. Afin de rendre ces applications aussi performantes que possible, une compréhension complète et précise de ces systèmes est requise.

Une mousse peut être vue comme une collection de films de savon liés entre eux. Il est connu à l'heure actuelle que les comportements de ces films, tant au niveau individuel (drainage, fluage...) que collectif (échanges au travers des bords de Plateau, éclatement...) influencent grandement le comportement global des mousses. Avant de vouloir caractériser ces dernières, il est donc nécessaire de posséder une solide connaissance des comportements de ces films de savon sous divers contraintes et situations. Le présent travail s'inscrit dans cette optique. Nous nous sommes proposé de réaliser diverses expériences impliquant des films de savon verticaux, en vue caractériser le comportement des grandeurs qui les décrivent (épaisseur, tension de surface...) en fonction des conditions expérimentales. Les films de savon tels qu'obtenus en tirant un cadre fermé hors d'une solution d'eau savonneuse sont caractérisés par un temps de vie allant de quelques secondes à quelques heures, suivant le surfactant utilisé. Suivant la grandeur physique considérée et la nature de l'expérience à réaliser afin de l'étudier, il est souvent nécessaire de trouver un compromis sur la nature du surfactant à employer afin que le film vive assez longtemps pour réaliser la mesure. Pour nous affranchir de cette contrainte temporelle, nous avons construit un dispositif expérimental permettant de maintenir des films de savon verticaux sur des temps outrepassant largement leur temps de vie typique. Ce dispositif assure le maintien temporel des films et leur permet de conserver des caractéristiques proches de celles liées à leur état naturel. Bien qu'il soit théoriquement envisageable d'utiliser ce dispositif pour maintenir des films obtenus avec divers surfactants, nous nous sommes focalisés sur une solution décrite dans la littérature [14],

car elle semble à la fois proche des surfactants habituellement trouvés dans le commerce (shampoing, détergent...) et contrôlée chimiquement. Sa composition chimique précise est en effet connue et il est possible d'ajouter des espèces chimiques caractérisées afin de modifier ses propriétés. Nous avons ensuite mis au point une expérience visant à caractériser l'épaisseur de ces films en fonction des divers paramètres expérimentaux liés à leur maintien. Forts de ces mesures d'épaisseurs, nous nous sommes penchés sur l'équilibre mécanique des films verticaux, et plus particulièrement sur le rôle joué par le profil de tension de surface vis-à-vis de cet équilibre. Nous avons construit une sonde basée sur l'élasticité des matériaux déformables afin d'obtenir une mesure de profil de tension de surface dans nos films maintenus. Nous nous sommes ensuite intéressés à la flottabilité dans ces films. Nous avons mis au point une expérience visant à illustrer le rôle des profils d'épaisseur et de tension de surface vis-à-vis de cette flottabilité. Enfin, nous avons développé une expérience ayant pour but d'étudier l'influence d'une différence de température locale sur nos films maintenus; montrant notamment l'influence de cette contrainte thermique sur la flottabilité. En résumé, nous nous sommes intéressés à des phénomènes et grandeurs macroscopiques liés aux films de savon verticaux. Au vu de nos résultats, nous pouvons affirmer que la description des phénomènes liés aux films de savons verticaux peuvent s'interpréter à partir de modèles impliquant leur profils d'épaisseur et/ou de tension de surface. D'un point de vue microscopique, ces profils macroscopiques dépendent directement de la physico-chimie interfaciale liée aux molécules de surfactant utilisées pour créer les films. Vu que cette dernière n'est encore que partiellement comprise et intégrée dans les modèles décrivant les films de savon, nos résultats peuvent être considérés comme des cas exemplatifs permettant de tester de nouveaux modèles et concepts concernant la description microscopique du comportement des films de savon.

Summary

Liquid interfaces relative to surfactant solutions have been in the center of numerous studies these last decades. Indeed, these interfaces are parts of complex physical systems such as foams and emulsions. These latter are nowadays implied in many industrial applications such as oil prospection, fire control in precarious situations (e.g. on board of the ISS) or thermal insulation. A full and precise understanding of those systems is required before optimizing those applications. A foam can be considered as an assembly of soap films interacting with each others. It is known that the individual and collective behaviors of those films (drainage, bending, burst...) strongly influence the global behavior of foams. It is then necessary to dispose of reliable knowledge about the behaviors of those films before going further in foam characterizations. The present work has been conducted on this idea. We proposed to realize experiments on vertical soap films in order to characterize their typical physical quantities (thickness, surface tension...) as functions of the experimental conditions. Soap films as obtained by pulling a closed frame out of a soapy water solution present lifetimes ranging from a few seconds to a few ours, depending on the used surfactant. Following the physical quantity to be investigated and the experiment aiming this measurement, it is often necessary to find a compromise on the nature of the surfactant to be used so that the measurement is possible. Since we wanted to avoid those temporal constraints, we built a setup which aims to maintain vertical soap films as long as possible. This setup allows to maintain the film without bringing considerable modifications to their usual behaviors. Even if it is theoretically possible to use this setup with any surfactant, we focused on a surfactant solution described in [14], for its relative similarity with the surfactants found in commercial products (shampoo, detergents...) and the precise chemical knowledge and control it offers. We then built up an experimental setup aiming to characterize the thickness profiles of the maintained films as functions of the experimental conditions. Those measurements allowed us to investigate the mechanical equilibrium linked to the films, especially in terms of the surface tension profiles. We built up an elastic probe in order to perform surface tension measurements in our maintained films. We then focused on the dependency of buoyancy in the film with respect to

the thickness and surface tension profiles of the film. We then came up with an experiment aiming to study the influence of a local temperature difference on our films. These experiments revealed that the temperature difference is prone to influence the buoyancy. As a summary, we considered phenomena and macroscopic quantities linked to vertical soap films. Following our results, we can claim that the characterization of these phenomena can be achieved in terms of models including the thickness and/or surface tension profiles. From a microscopic point of view, those macroscopic profiles directly depend on the interfacial physical chemistry of the surfactant molecules used to build the films. Since this interfacial physical chemistry is not yet fully understood nor included in theoretical models for soap films, our results can be considered as typical tests aiming to help the microscopic description of the behaviors of soap films.

Introduction

According to various sources, common nowadays soaps find their origin several thousands of years ago. People like sumerians were accustomed to mix olive oil with cedar ashes in order to produce a washing mixture. Today, soaps such as Marseilles soap, are still made out of similar ingredients. In addition to those basic recipes, the advent of science and technology has led to the apparition of many kinds of soaps, which are recovered in numerous various fields of human activities (oil prospection, food industry...).

When put in water, soap may lead to the apparition of bubbles, which are liquid vesicles in which air is imprisoned. If soapy water is violently disturbed, bubble collections, known as foams, appear at the water-air interface, and can stay for times ranging from a few seconds to several hours, depending on the nature of the soap. Simpler objects, called soap films, can be obtained by pulling any closed loop out of a soapy water vessel. When withdrawn out, a very fragile and colored liquid sheet is sustained by the loop. The existence of those soapy objects is known to depend on the presence of soap in water since ages.

With the advent of sciences, those soapy objects have awakened the curiosity of scientists. Why is it so fragile and colored? What is the link between their existence and the presence of soap in water? The increasing knowledge in natural sciences and phenomena such as fluid mechanics and optics have led to constantly increasing understandings of the behaviors of such objects. Sir Izaak Newton in the 17th century understood that the color fluctuations of vertical soap films are the signature of a temporal thinning of those films, linked to inner fluid displacements.

The advent of physical and chemical concepts in the 18th and 19th centuries have led to the apparition of atoms and molecules as being the basic component of matter. Soaps have been identified to be composed of diluted surfactant molecules, which specific features have been intensively used in order to explain why soaps allow the existence of pre-cited soapy objects.

Even if overall comprehension regarded to the role of surfactant molecules are acquired, there are still considerable lacks of precise understanding with respect of soapy objects. Those lacks come from the difficulty, both theoretical and experimental, to characterize the behaviors of surfactant molecules in such systems. In fact, very complex chemical equilibria arise at water-air interfaces for surfactant molecules. Nowadays technologies allow to probe those equilibria only very superficially. Additions of secondary perturbative effects (from molecular, thermal, biological origins) considerably tend to increase the complexity of the interfacial dynamics, making the devoted theories rather difficult to confirm experimentally.

In the last decades, soap films have been intensively used for the purpose of experimental bi-dimensional fluid dynamics, because of their ability to easily product nearly-two-dimensional channels. In those experiments, soap films are rather used like convenient tools due to their ideal hydrodynamic features than particular physical objects. Domains like turbulence have led to numerous experimental and theoretical works involving those channels. A few examples of such uses of soap films are given at the end of Chapter 1.

Since they are not fully understood as physical objects, soap films are still the subject of experimental and theoretical works nowadays. Wise utilizations of present scientific equipments and technologies have proven to be suited for the study of soap films features and phenomena such as drainage, marginal regeneration, thickness fluctuations under constraints... The present thesis has been performed in this idea, and presents several experiments aiming to characterize relatively basic features of vertical soap films, both experimentally and theoretically. Chapter 1 presents the state of the art in terms of concerned fluid mechanics and surfactant science. Chapter 2 explains why and how vertical soap films can be maintained in time. We propose an experiment in order to characterize the thickness profiles of such films as a function of the experimental parameters. Chapter 3 describes an experiment which aims to probe surface tension profiles in soap films by the mean of elastic objects introduced into the films. Models are proposed to calibrate elastic sensors, as well as to relate surface tension and thickness measurements. In Chapter 4, we re-interpret the concept of buoyancy in soap film, and show how it is possible to use previous measurements (thickness and surface tension) to predict observed phenomena. Chapter 5 is devoted to the study of thermally constrained soap films. Thermal plumes arising in the films due to thermal gradients are in the center of our investigations, and compared to their three-dimensional analogs.

Chapter 1

State of the art

This first chapter is devoted to the description of the basic physical and chemical phenomena involved in our experiments. We mainly focus on the influence of surfactant molecules on the behaviors of liquid interfaces. We show how the particular properties of those molecules at a water-air interface allow for the existence of fluid objects such as soap films and soap bubbles. The main influences of the interfacial physical chemistry of surfactant molecules on the macroscopic behaviors of soap films are presented.

1.1 Size of a liquid

Liquids are defined as materials which embrace the shape of their container. When thinking about liquids, people usually consider everyday-life situations such as water in a glass, gas in a tank, wine or beer in a bottle, or more geological examples like seas, oceans, rivers, etc. Unconsciously, all these examples involve liquid amounts which are so that they all fit with the definition mentioned above. If the glass or the tank is tilted, the liquid is supposed to flow out, spreading on the floor or embracing the shape of another container. Beyond this common and rather naive perception of liquids, interesting phenomena occur if the amount of liquid is substantially reduced. For instance, imagine a glass of water emptied without tilting (with a pipe, or simply by evaporation). The water level decreases until the water/air interface gets close to the bottom. If one asks what happens if the water level is further decreased, the answer might not be obvious to give. For simplicity, we suppose that the surface of the glass containing the water is hydrophobic [1]. First of all, let us consider the case where there is just not enough water in the glass to fill the bottom. If the liquid is further removed, the remaining amount of water forms a puddle on the bottom of the glass, such as presented in Figure 1.1, with no contact with the lateral walls. The puddle forms a water layer characterized by a radius R and a constant thickness h , except near

the edges where it adopts a rounded shape (see Fig. 1.1). This configuration may appear counterintuitive at first glance. In fact, one would expect the puddle to spread under the action of its internal pressure profile defined as :

$$P_{\text{int}} = P_{\text{atm}} + \rho gh, \quad (1.1)$$

with P_{atm} the atmospheric pressure, ρ the density of water, g the gravity constant. Following this pressure reasoning, the water should always spread and be in contact with the lateral edges of the glass. Therefore, there must be an additional pressure or force in the system preventing the puddle from spreading under its own weight. This pressure originates in the surface tension, as explained in the next Section.

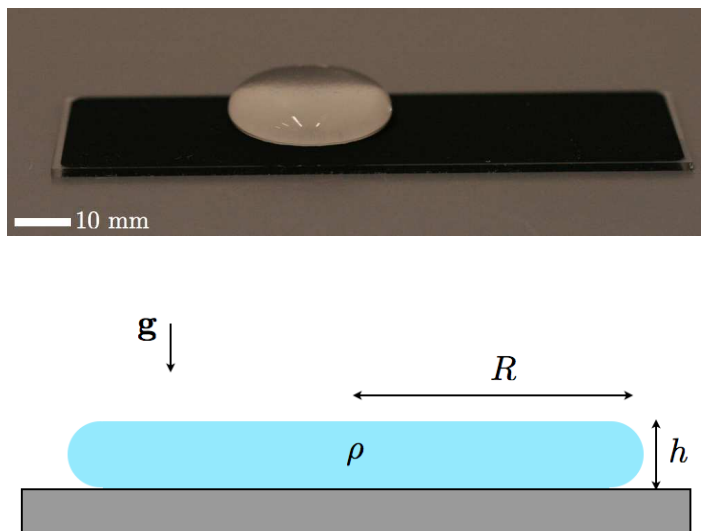


Figure 1.1: Top : view of a water puddle deposited on a hydrophobic surface. Bottom : scheme of a transverse view of the same puddle.

1.2 Surface tension

Let us consider the water of a lake, at rest, without any wave at the air/water interface. If one throws a rock into the lake, it penetrates the water surface under the action of its weight (the density of the rock is supposed to be higher than the one of water). A few instants after the collision, circular waves develop from the impact point (Fig. 1.2), spreading out circularly [1–3].

It is known from wave propagation theory in continuous media that tension forces must exist in the medium in order for waves to develop under the action of a perturbation [4, 5]. This tension can either be exerted by a devoted, external

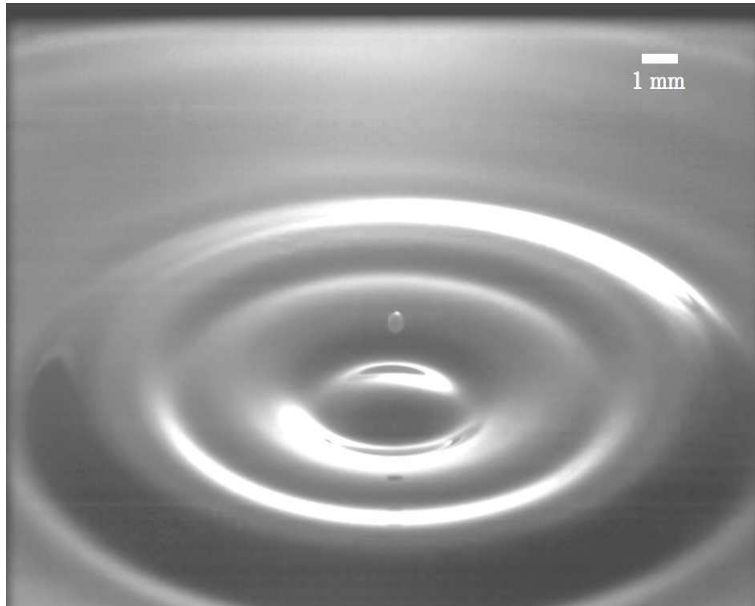


Figure 1.2: Surface waves at a milk-air interface. The perturbations have been caused by the impact of a milk droplet on the interface, a few milliseconds before the picture was taken.

device (e.g. guitar strings), or results from cohesive forces inside the medium (e.g. solid media such as glass, iron...). This situation of the perturbed lake is analogous to the one of a rope with one extremity submitted to a sinusoidal motion. The sinusoidal motion propagates from the excited extremity through the length of the rope. The speed v and the wavelength λ of the perturbation depend on both the tension force in the rope and its physical properties, so that :

$$v = \sqrt{\frac{T}{\mu}}, \quad (1.2)$$

with T the tension force in the rope, μ its linear mass, and $\lambda = \frac{v}{\nu}$, where ν is the frequency of the sinusoidal motion [4, 5]. Following those (well-known) facts and everyday-life experiments, a tension force must be present at the air/water interface of the lake in order for the waves to propagate. This tension force is called the surface tension of the interface [1, 2]. Its origin arises from the molecular energetic default at the air/water interface [1]. Any water molecule in the bulk is characterized by a cohesive energy, resulting from its interaction with its surrounding molecules [6]. At the interface, this cohesive energy decreases because the interaction between water and air molecules are weaker than the interaction between water molecules. This energy default at the interface is usually

used to define the surface tension. If ε represents the cohesive energy of a water molecule and S the area of the interface, the surface tension γ of this interface reads [1] :

$$\gamma = \left. \frac{d\varepsilon}{dS} \right|_{\text{interface}}. \quad (1.3)$$

From a dimensional point of view, expressing γ as an energy default per unit area is equivalent to express γ as a force per unit length. Thus, the surface tension linked to a given interface can equivalently be considered as one or the other, following the considered phenomenon.

Returning to the problem of the non-spreading puddle (Fig. 1.1), one understands that surface tension is facing the gravitational pressure field in the puddle. The rounded shape of the interface at the edges comes from the fact that the energy default, and so the area of the interface, must be minimized. It can be shown that the sphere is the geometrical entity which satisfies this condition for a given volume [1–3]. Including surface tension in the problem of the spreading puddle means that the thickness h of the puddle results from a competition between the hydrostatic pressure and the surface tension. Observation of puddles on a hydrophobic surface reveals that $h \sim 10^{-3}\text{m}$ (see Fig. 1.1). The pressure difference at the rounded edges of the puddle can be approximated by the hydrostatic pressure linked to h , say $\Delta P \sim \rho gh$. The interfacial force opposing this pressure can be expressed as $F \sim \Delta P S$, with S the surface of the rounded edge. Approximating this latter by half a sphere area, one can then estimate $F \sim \rho gh^3$. Adimensioning F by h leads to an estimation for γ , being :

$$\gamma \sim \frac{F}{h} \sim 10^{-2} \text{ N/m}. \quad (1.4)$$

Measurement methods, such as the Wilhelmy plate and pending droplet methods [1,7,8] have been developed in order to get accurate measurements of γ . They have revealed that the surface tension of an air/water interface is 72.8 mN/m, which is of the same order of magnitude than our simple estimation. Table 1.2 presents typical surface tension values for common liquid interfaces [1]. It is instructive to focus on the considerable difference between the values of usual liquids such as water and the case of mercury. This difference originates in the fact that water, glycerol and acetone are liquids, while mercury is a metal. The nature and the magnitude of the molecular bondings are thus different. Liquids are mainly characterized by covalent, van der Waals and H-bridge bondings while metals are known to present metallic bondings which are among the strongest that can be found [6]. Since γ is defined from the cohesive energy default at the interface, one understands why the surface tension of mercury is so high.

Interface	γ (mN/m)
air/water (25°C)	72
air/water (100°C)	58
water/oil (25°C)	50
air/mercury (25°C)	485
air/glycerol (25°C)	63
air/acetone (25°C)	24

Table 1.1: Surface tension values for some usual interfaces [1].

We can now wonder what would happen to the puddle (see Fig. 1.1) if its volume is modified. If water is added to the puddle, it is quite obvious that its radius R will rise in order to satisfy the mechanical equilibrium described above (i.e. to keep h constant). But if water is removed, the rounded edges of the puddle will get closer and closer until they come into contact. Beyond a given critical volume, the puddle becomes a droplet, characterized by a spherical shape, and no more spreading is observed [1,3]. This transition from a (spread) puddle to a (unspread) droplet is the signature of a transition in the competition between interfacial and volume forces. Imagine the case of a water amount which is not submitted to gravity. Following the definition of surface tension in terms of cohesive energy density, it is supposed to adopt a spherical shape in order to minimize the interfacial potential energy γ . But in presence of gravity, the ideal spherical shape collapses under its own weight, until the internal hydrostatic pressure is weak enough for the surface tension forces to oppose it. Since these surface tension forces oppose the in-volume gravity effects, the surface forces become stronger than the volume forces under a given volume. Below this limit, spherical droplets will always be observed, even in presence of gravity [1,3].

It is possible to determine the critical volume below which the surface tension forces become preponderant. At the transition, the equilibrium between hydrostatic pressure and surface tension still holds. If the spherical droplet is characterized by a radius R , its weight reads $F = 4\pi\rho gR^3/3$, while its surface energy is given by $4\pi R^2\gamma$. The transition then occurs when the puddle radius is close to a critical length scale l_c expressed as :

$$l_c \sim \sqrt{\frac{\gamma}{\rho g}} \quad (1.5)$$

and called the capillary length [1–3]. From Table (1.2), typical values of this capillary length are estimated for water and mercury at 25°C to 2.7 mm and 1.91 mm, respectively. This estimation reveals that even if the surface tension of mer-

cury overpasses the one of water, the volume forces are so important than water droplets are bigger than mercury ones.

Another convenient way to describe the competition between volume and interfacial forces is to consider the Bond number, defined as the ratio of both magnitudes :

$$Bo \sim \frac{\rho g R^2}{\gamma}. \quad (1.6)$$

If Bo is larger than unity, the volume forces are preponderant and spreading is observed. On the other hand, a value smaller than unity corresponds to dominant surface tension forces and spherical droplets. Note that $Bo=1$ gives the capillary length defined by Eq.(1.5).

1.2.1 Laplace pressure

Let us consider a soap bubble. Similarly to the case of the droplet, soap bubbles always tend to adopt a spherical shape. Following the reasoning made about the puddle in the previous section, it implies that a pressure difference exist between the inside and outside of the bubble, otherwise it would collapse on itself due to surface minimization. It can be shown [1, 2] that the pressure difference is linked to the surface tension of the interface as :

$$\Delta P = \frac{2\gamma}{R} \quad (1.7)$$

if R is the radius of the bubble. This expression, known as the Laplace law evidences that curved liquid interfaces are always coupled with pressure differences between the phases in contact. Equation (1.7) is actually a simplified expression of a more general law, being [2] :

$$\Delta P = \gamma \left(\frac{1}{R_1} + \frac{1}{R_2} \right), \quad (1.8)$$

where R_1 and R_2 are the curvature radii of the interface at the considered point.

1.3 Surface tension variations

Since surface tension originates in the molecular interactions at the interface, any modification of these interactions leads to a modification of γ [1, 6]. There are two main effects opposing cohesion in a liquid : (i) chemical impurities, i.e. the presence of atoms or molecules which are different from the main constitutive species, and (ii) thermal agitation, which tends to destabilize the cohesive interactions between constituents [6]. These latter can be evidenced easily at home, by dropping ground pepper on a water interface, and then bringing a heat source (a soldering iron for example) close to the interface. The pepper immediately moves

away from the heating point. The same effect can be obtained by adding chemical impurities. For instance, dropping a drop of commercial soap in the center of the interface will result in the same spreading of the pepper grains. In both cases, the motion of the pepper grains comes from an inhomogeneity in γ , induced by the thermal or chemical perturbation. Those perturbations tend to decrease the magnitude of the cohesive interactions between the water molecules at the interface. This leads to a decrease of γ in the vicinity of the perturbation point, resulting in a radial net force on the perturbed area. This force acts until the perturbed area extends over the whole interface. The appearance of interfacial flows due to surface tension gradients is called the Marangoni effect [1, 2].

A quite stunning feature of this simple experiment is that the pepper dispersion is more efficient with soap than with heat. The soldering iron has to be very hot in order to create Marangoni flows, while only a small droplet of soap, even dilute, is enough to get remarkable effects. Actually, the thermal agitation at ambient temperature (25° C) is given by $\varepsilon_{th} \sim k_B T \sim 0.025$ eV, with k_B the Boltzmann constant and T the temperature [9], while the typical cohesive energy for water molecules is $\varepsilon \sim 1$ eV [6]. It is therefore more easy to disturb the interface by adding chemical species than by heating. To conclude on this point, we have to mention that thermal perturbations are reversible in time, while chemical ones are not.

1.4 Surfactant molecules

Surfactant molecules are chemical agents which tend to localize at the surface of a liquid [10, 13]. For instance, commercial soaps, toothpastes and many other everyday-life products contain surfactant agents.

Surfactant molecules are constituted of two different parts : a hydrophilic head and a hydrophobic tail (see Fig. 1.3). Usual surfactant molecules are characterized by a head which present an electric dipolar torque, due to the presence of ionic compounds, which release ions when set in solution [11–13]. If the released ion is positive, the surfactant is called anionic. This is the case of the widely used Sodium Dodecyl Sulfate (SDS) (see Fig. 1.4) [1, 10, 13]. In opposition, if the ion is negative, then the surfactant is called cationic (e.g. cetyl trimethylammonium bromide (CATB), see Fig. 1.4). The polar head can also result from the presence of both signs. Those surfactants are called zwitterionic (e.g. Cocamidopropyl betaine (CAPB), see Fig. 1.4). Non-ionic surfactants also exist and present the usual surfactant properties, but with no ion released in solution (Triton X-100 for example, see Fig. 1.4).

Knowing the nature of the surfactant is important, especially if they are mixed. Anionic and cationic surfactant are incompatible due to the opposite nature of the ions they release in the solution. However, they can be mixed with zwitter-

ionic surfactants, or non-ionic surfactants [10]. It is usual to find mixtures of several surfactants in commercial soaps, detergents, shampoos... for the purpose of industrial care products [10].

On the other side of the surfactant molecule, tails are made of a carbon chain, which length is usually of several to a few tens of atoms [1, 10–13]. In opposition to the head, those tails usually do not exhibit an electric dipolar torque. This implies that the heads are soluble in water, while the tails are not. Such molecules are called amphiphilic : when set in aqueous media, they tend to organize in order to satisfy the hydro affinities of both extremities, leading to organizations such as sketched in Figure 1.3. If the aqueous medium presents an interface with air, then surfactant molecules will tend to organize in a (mono)layer at the interface : the heads pointing toward the aqueous phase and the tails pointing toward the air [10–12]. If no interface is present, or if the air-water interface is saturated, surfactant molecules may form in-bulk structures called micelles (see Fig. 1.3), also satisfying polar affinities. Several structures can be observed, following the nature of the surfactant (micelles, cylinders, bilayers...) [10–12].

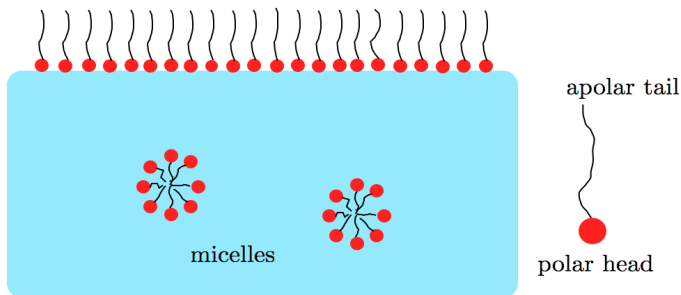


Figure 1.3: Surfactant molecules organization in water. Due to hydro affinities of heads and tails, micelles form in the bulk, while a (mono)layer develops at the interface.

Common surfactant, like those used to manufacture shampoos and home detergents adopt those kinds of configurations in solution. Nevertheless, insoluble surfactants, such as CF_{12} , exist. Insoluble means that they can only be localized at the interface and do not form micelles in bulk [10–12]. Those kinds of surfactant are used to study the behaviors of ideal surfactant monolayers (i.e. Langmuir monolayers) [1, 11].

1.4.1 Surfactants used in the present thesis experiments

For the purpose of our experiments, we chose to use the surfactant mixture described in a paper by Golemanov and collaborators [14]. This mixture is made of

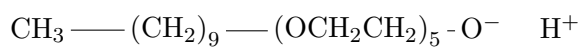
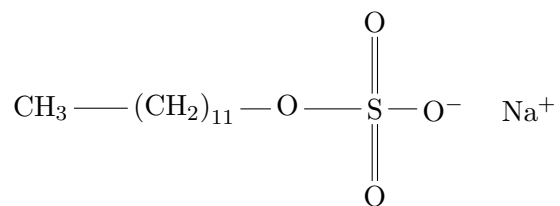
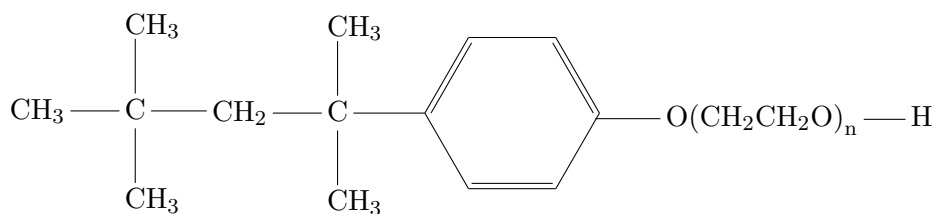


Figure 1.4: Semi-developed chemical formulæ for Tritton, SDS, and Neodol 91-5.

sodium lauryl-dioxyethylene sulfate (SLES), an anionic surfactant, and cocoamidopropyl betaine (CAPB), which is a zwitterionic surfactant. This mixture is close to usual commercial soap recipes, with the advantage of a precise knowledge about the chemical composition and the possibility to tune the viscosity and the surface modulus of the interface by adding chemical species (glycerol, fatty acids...) [14]. Moreover, this mixture has been pointed out to avoid typical issues linked to surfactant solutions, such as the presence of insoluble surfactant precipitates or time-dependant interfacial dynamics (see [14]). Figure 1.5 shows the semi-developed chemical formulæ of those surfactants.

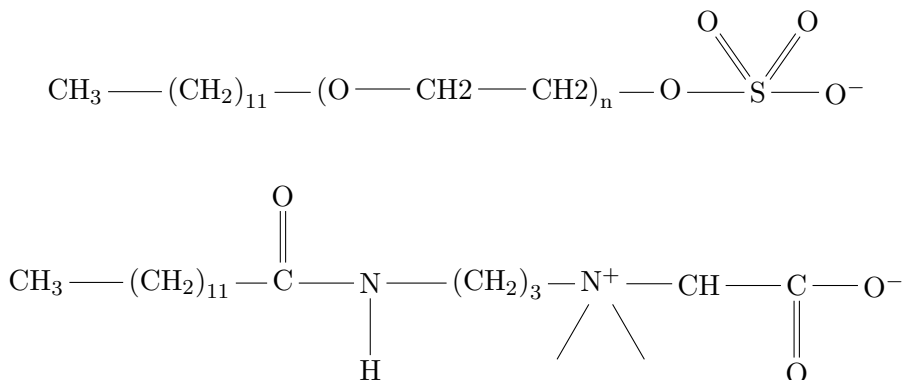


Figure 1.5: Semi-developed chemical formulæ for SLES (top) and CAPB (bottom).

1.4.2 Surface concentration and surface pressure

Consider a pure water-air interface on which surfactant molecules are progressively added. The surface concentration (or surface coverage) Γ is defined as the number of surfactant molecules per unit area at the interface [1, 10–12]. Let us consider two ionic surfactant molecules on a uni-dimensional interface, apart from a distance which is large compared to their size. If those molecules are brought closer to each other, their heads start to repel. Following the separating distance, the repulsion can be electric or steric, or both [6, 10–12]. Coming back to an entire air/water interface, one understands that surfactant molecules tend to drive away from each other due to their repulsive interactions. Assuming that only steric repulsion can occur, the situation of surfactant molecules at the interface becomes quite analogous to the situation of a perfect gas. This vision, known as the gas model for surfactant layers, has been widely used in theoretical descriptions of surfactant (mono)layers and led to thermodynamical approaches for interfacial quantities [10–12, 15].

Following this gas description for surfactant monolayers, one can define the surface pressure linked to the surfactant layer, as :

$$\Pi(\Gamma) = \gamma_0 - \gamma(\Gamma), \quad (1.9)$$

with γ_0 the surface tension of the unperturbed interface [1, 10–13, 15]. This definition is in agreement with the common definition of a gas pressure, Γ being the particle density. In fact, Π increases with Γ , since γ decreases with Γ . This is compatible with the usual gas pressure dependence on the number of particles [4]. Following the remark made in Section 1.3 about perturbations brought by thermal agitation on molecular cohesion, Π implicitly depends on the temperature. Since γ decreases with temperature, Π increases with temperature, which is, once again, in agreement with common gas models [4].

Some surface pressure effects can be demonstrated by rather simple experiments. Assume a air/water interface on which a light plastic barrier is deposited. This barrier defines two independant interfaces, as exposed in Figure 1.6. The barrier is prone to move freely in the lateral direction. If a drop of surfactant is added on one of the interfaces, a surface pressure develops on the loaded interface, and the barrier starts to move towards the non-pertubated interface. This effect can easily be evidenced thanks to non-soluble surfactants such as CF_{12} . The same experiment performed with soluble surfactant may not work as easily, since the surfactant molecules may pass under the barrier and re-equilibrate both interfaces. Those observations were made in Paris, with J. Bico and B. Roman, for the purpose of the experiments described in Chapter 3.

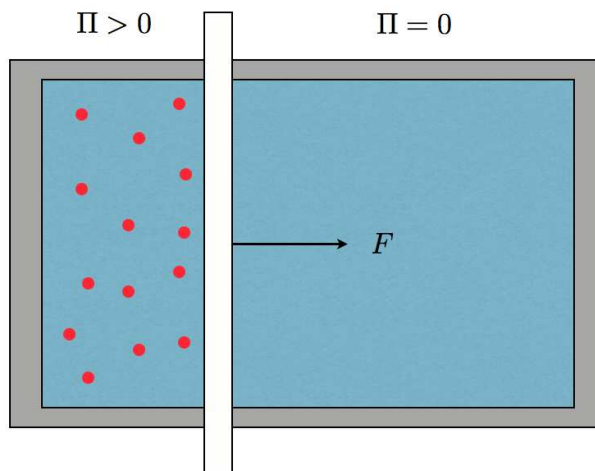


Figure 1.6: Scheme of a Langmuir tank. A water-air interface is divided by a mobile barrier. The dots represent the surfactant molecules at the loaded interface.

The net force applied on the barrier due to the surface pressure can be expressed as :

$$F = \delta\Pi L = (\gamma_0 - \gamma(\Gamma))L, \quad (1.10)$$

which is exactly what one would get by reasoning in terms of surface tension forces acting on the mobile barrier. This setup can also be used with a barrier which displacements are imposed thanks to a devoted device. The loaded area can either be increased or decreased, leading to the opposite behaviors for the surface pressure. This setup is known as the Langmuir tank [1,10,12]. It has been widely used in order to realize surfactant monolayer compressions. Those experiments allow to study the behavior of surfactant molecules with imposed pressure, bringing insights on their organization in the presence of external constraints (see for example [16] and [17]).

1.5 Adsorption layer and dynamical equilibrium

1.5.1 Critical micellar concentration (CMC)

We consider the air/water interface of the previous sections progressively loaded with surfactant molecules. Along the loading, the surface concentration Γ increases, the surface pressure $\Pi(\Gamma)$ increases as well, while the surface tension $\gamma(\Gamma)$ decreases. As emphasized previously, several methods exist to measure the surface tension evolution as a function of parameters such as the temperature or the surfactant concentration (pending droplet method, Wilhelmy plate...) [1,7,8]. Figure 1.7 is a plot of the evolution of the surface tension versus the surfactant concentration for the surfactant mixture used for the experiments described in the next chapters. We obtained this curve thanks to a pending droplet device. At very low concentrations, Γ is just too weak for surface tension to be significantly modified by soap molecules. As the concentration is increased, the surface tension monotonously decreases, due to the progressive filling of the interface in surfactant molecules. Then a second change in slope is observed. It corresponds to the saturation of the interface. Beyond this value, the surface tension variations are less important. The transition corresponds to the critical micellar concentration (CMC) which is related to the surfactant [1,10–12]. The CMC is followed by the apparition of micelles and other structures in the bulk [10]. Even if the curve presented in Figure 1.7 allows to determine the CMC of our solution, the nature of the organized structures appearing beyond the CMC remains unknown. Precise knowledge about those structures requires scattering experiments (neutrons or X rays, see for example [18]). To our knowledge, such studies have not yet been performed on the surfactant solution we used in our experiments. The CMC

value of our solution is 10^{-3} mol/L.

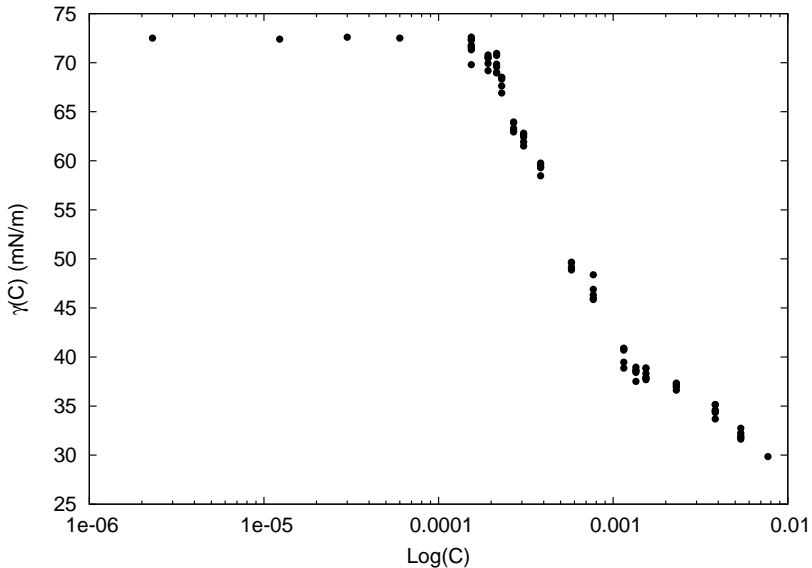


Figure 1.7: Surface tension γ versus surfactant concentration C of the solution SLES+CAPB described in [14], diluted in pure water and added of 0.3% glycerol.

1.5.2 Dynamical equilibrium at the interface

Let us come back to the water tank as presented on Fig. 1.6, with a typical surfactant concentration of several times the CMC. We suppose that the area of the interface can be increased at a glance and that a surface tension sensor provides the surface tension value at any time. If the area is progressively increased, the surface tension measured by the sensor will indicate the value measured at the CMC, even for large area increments (we do not take interfacial organizations and phase transitions into account in the present reasoning. See [10–12] for related effects.). This means that Γ remains unchanged even if the area is increased. In order for Γ to remain constant, surfactant molecules must be added to the expanding interface. In the present case, these added molecules can only come from the bulk, suggesting that there are surfactant molecule exchanges between the bulk and the interface. A saturated interface must then be seen as resulting from a dynamical equilibrium between in-bulk and interfacial molecules. In addition to micelles presented in Figure 1.3, it is possible to find isolated surfactant molecules in the bulk, i.e. which are not englobed in self organized structures [10–12, 19–22]. There is an equilibrium between the molecules at the interface and the molecules which are close to the interface and would like to adsorb at this interface (see

Fig. 1.8). These molecules define a layer which is located in the bulk, just beneath the interface, and called the adsorption layer [10–12]. The equilibrium between the bulk and the interface can then be described as [10–12, 15] :

$$\Gamma = kC, \quad (1.11)$$

where C is the bulk concentration and k the equilibrium constant. This expression is analogous to any expression describing a dynamical chemical equilibrium, excepted that the equilibrium constant k is expressed in meters.

Figure 1.7 shows that γ still decreases with C above the CMC, which is not compatible with the concept of dynamical equilibrium. The fact is that k is not constant with C , due to surfactant-linked phenomena occurring both in the adsorption layer and at the interface. For example, above the CMC, the micelles present in the bulk can adsorb at the interface. Those adsorptions can lead to micelle ruptures at the interface. Figure 1.8 is a scheme of the situation extracted from [20]. Those ruptures induce the apparition of extra surfactant molecules at the interface, thus modifying the pre-supposed equilibrium value of Γ [10–12, 19–22]. Those kinds of phenomena can be evoked to justify the fact that surface tension keeps on decreasing above the CMC (see Fig. 1.7).

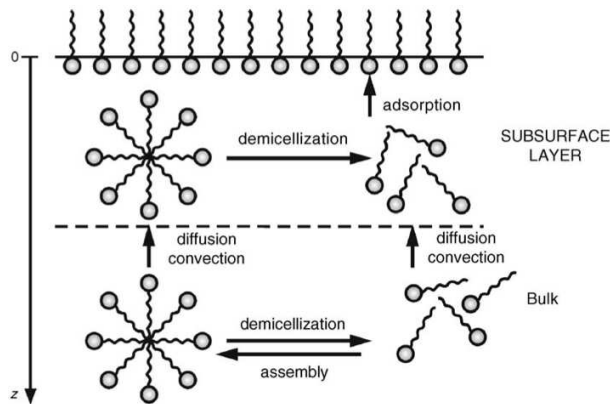


Figure 1.8: Schematics of the micelle rupture process near the interface (from [20]).

In addition to those in-bulk organized structures, interfacial organized structures may develop as well. Compression tests performed with CF_{12} showed that highly compressed monolayers lead to the apparition of surfactant puddles at the interface, very similar to the ones obtained by dropping oil in water. These qualitative observations were made during the compression experiments presented in Chapter 3, in Paris. Monolayer compression experiments revealed that phase transitions can be observed in surface pressure isotherm curves, attesting for modifications

in the organizations of surfactant molecules at the interface [23–25]. As presented in Figure 1.9 (top), these phase transitions represent violent modifications of the evolution of the surface pressure linked to the interface. The different phases are linked to various behaviors for the interface (see [23–25]), which may lead to a modification of the chemical equilibrium (i.e. k depends on the phase of the interface).

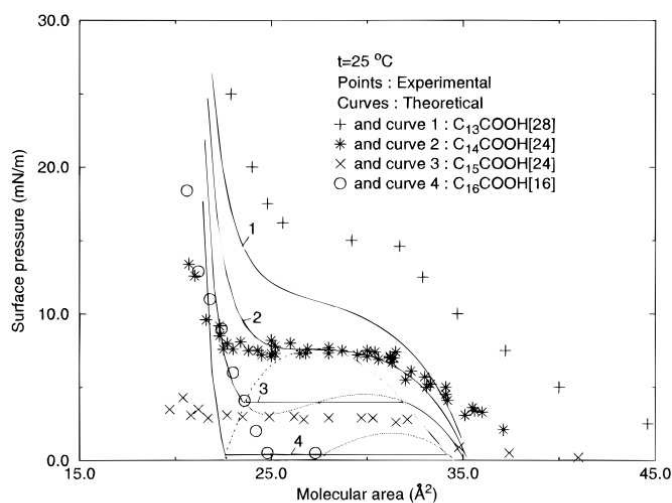


Figure 2. Comparison between theoretical and experimental π - A isotherms for the C_{14} - C_{17} fatty acids.

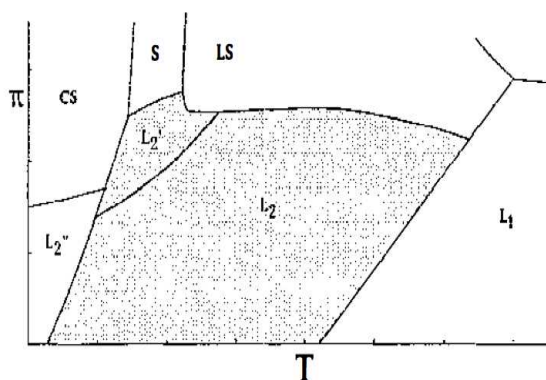


Figure 1 Generalized monolayer phase diagram for long-chain acids, acetates, and ethyl esters. From Bibo et al (15).

Figure 1.9: Top : isotherms for the surface pressure of various surfactants (from [25]). These isotherms present the typical shape resulting from the phase transitions of a medium (see [9]). Bottom : phase diagram built on the basis of isotherm curves (from [23]).

Even if initially simple, the behavior of compressed surfactant layers can become rather complicated, following the properties of the corresponding molecules, and their behaviors as function of the experimental conditions (temperature, PH... [10–12,14]). To conclude on this point, let us mention that the surface tension of a loaded interface is supposed to be (logically) limited by the surface tension of the pure surfactant.

1.6 Monolayer elasticity

In this section, we consider a layer composed of insoluble surfactant molecules, which is not constrained in any way (surfactant molecules organize freely at the interface). In Section 1.4 we emphasized that surfactant molecules disposed at a air/water interface repel each other due to electrostatic and steric interactions. However, attractive interactions also occur. Due to the dipolar electric torque they exhibit, Van der Waals interactions develop between surfactant molecules at the interface [6,12]. Following the characteristics of the molecules, the resulting potential may become negative, so that the molecules attract [12]. Figure 1.10 illustrates a typical example of the potential linked to such interactions [6]. The attractive and repulsive energies add so that the global potential exhibits a minimum. The position of this minimum determines the inter-molecular distance of non-perturbed molecules. If this distance is decreased or increased, the molecules will tend to oppose to those modifications as a result of the existence of the minimum.

From this point of view, the situation of surfactant molecules at the interface appears as if they were linked by springs. In other words, if one tries to bring the molecules closer to each other, they will repel, while they will oppose a separation. As a consequence, a surfactant monolayer characterized by such interactions is subject to present elastic behaviors. The elasticity modulus of a surfactant monolayer is defined as :

$$E = \frac{d\gamma}{d\ln(A)}, \quad (1.12)$$

where A is the surface covered by the monolayer and γ is the corresponding surface tension [10–12,15].

The general case of soluble surfactants may be less obvious. Since the surface coverage is fixed by the dynamical equilibrium at the interface, the elasticity of such layers is influenced by this equilibrium as well. Two different situations can be drawn following the perturbation imposed to the interface. Let us consider an interface to which a stretching is applied on a given timescale. If the stretching is fast, i.e. occurring on a short time scale compared to the typical adsorption time, surfactant molecules might not have the time to diffuse from the bulk to the inter-

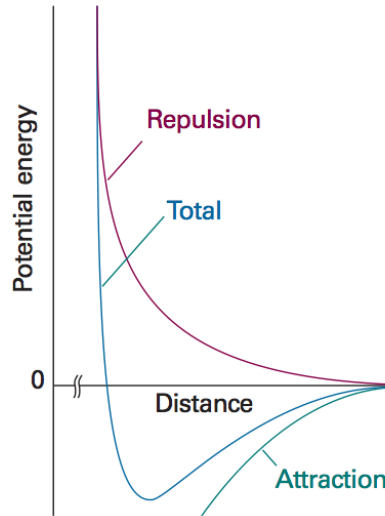


Fig. 18.10 The general form of an intermolecular potential energy curve. At long range the interaction is attractive, but at close range the repulsions dominate.

Figure 1.10: Typical potential energy curve related to inter-molecular interactions (from [6]).

face for covering the gained area. The number of molecules present at the interface thus remains unchanged. This case is analogous to the one of insoluble surfactant : the interface behaves almost as an usual elastic material and comes back to its initial state. This elasticity is called the Marangoni elasticity [10–12, 15]. On the other hand, if the stretching is applied on a long time scale, diffusion occurs between the bulk and the interface. This latter thus have the time to adapt their surface coverage to the area increase during the stretching time. The resulting elasticity refers to the dilatational properties of the interface under satisfied dynamical equilibrium conditions, and is called the Gibbs elasticity [10–12, 15, 26]. For a given monolayer, the elasticity which is observed depends on the ratio of the stretching timescale on the typical adsorption time of surfactant molecules at the interface.

As determined for elastic materials from mechanical traction tests, Young (elasticity) moduli of surfactant monolayers can be determined experimentally. Regarded the definition of the Young modulus for surfactant monolayers (Eq.(1.12)), area variations can be applied to the interface, which magnitudes can be fixed [26] or oscillatory in time [27], depending on the kind of elasticity to be measured. Note that optical methods also exist in order to measure monolayer elastic properties [29].

Following the nature of the surfactant molecules, these moduli can exhibit quite different values. For instance, the modulus of the SLES+CAPB mixture used in our experiments can be increased by adding a fatty acid to the solution. The initial elasticity modulus then goes from 4.2 to 305 mN/m [14] for percentages of fatty acid going from 0 to 0.4%. These elasticity increases can be evidenced by studying the typical lifetime of vertical soap films. Golemanov and coworkers have shown that increasing the surface elasticity of a SLES+CAPB mixture increases the lifetime of the related soap films [14]. The surface elasticity of a surfactant monolayer must then be considered as an influent parameter regarded to the behaviors of the related physical systems. As a comparison, surfactants such as SDS, Dodecyltrimethylammonium bromide (DTAB) and Tetraethylene glycol monoethyl ether (C_8E_4) are characterized by interfacial moduli of 0.79, 2.49 and 19.89 mN/m, respectively, for similar experimental conditions (concentration and temperature) [28]. Note that the C_8E_4 is a nonionic surfactant, which mass is similar to the one of SDS and DTAB. The difference between the Young moduli values of those surfactants reveals different magnitudes for the interactions of their constitutive molecules.

Beyond the ideal case discussed in this section, the shape of the potential interaction energy (Fig. 1.10) and the monolayer elasticity modulus (Eq.(1.12)) depend on both in-bulk and interfacial organizations presented in the previous sections. Experimental measurements made about interfacial quantities must then be associated to a particular state of the interface.

1.7 Soapy objects and curvature

We will now consider the cases where one tries to drift a surfactant monolayer away from an air/water interface. The most common situation is when a frame is pulled out of a bath of soapy water [1,30,31]. As it rises up above the interface, a thin soap film develops inside the frame, what is typical of a surfactant-loaded interface. In fact, if the water interface is pure, no film may develop inside the frame. The film apparition inside the pulled frame is a consequence of the elasticity of the surfactant monolayer. A few instants after the frame has completely been pulled out, the inner soap film starts to exhibit a horizontal fringe pattern, especially visible if the film is lit with a monochromatic light (see Fig. 1.11). Those fringes are equal thickness interference fringes, attesting of the weak thickness of the film. The film is acting as a Fabry-Perrot interferometer and the vertical fringe profile attests from the existence of a vertical thickness profile [4]. The film shown in Figure 1.11 is lit with a Na_2 lamp. Since the sodium typical wavelength is 589 nm, the typical thickness of those film is of the order of 1 μ m.

Let us consider a solution of SLES+CAPB as described in the previous sections. Careful look at the interferometric pattern of a freshly generated film reveals that

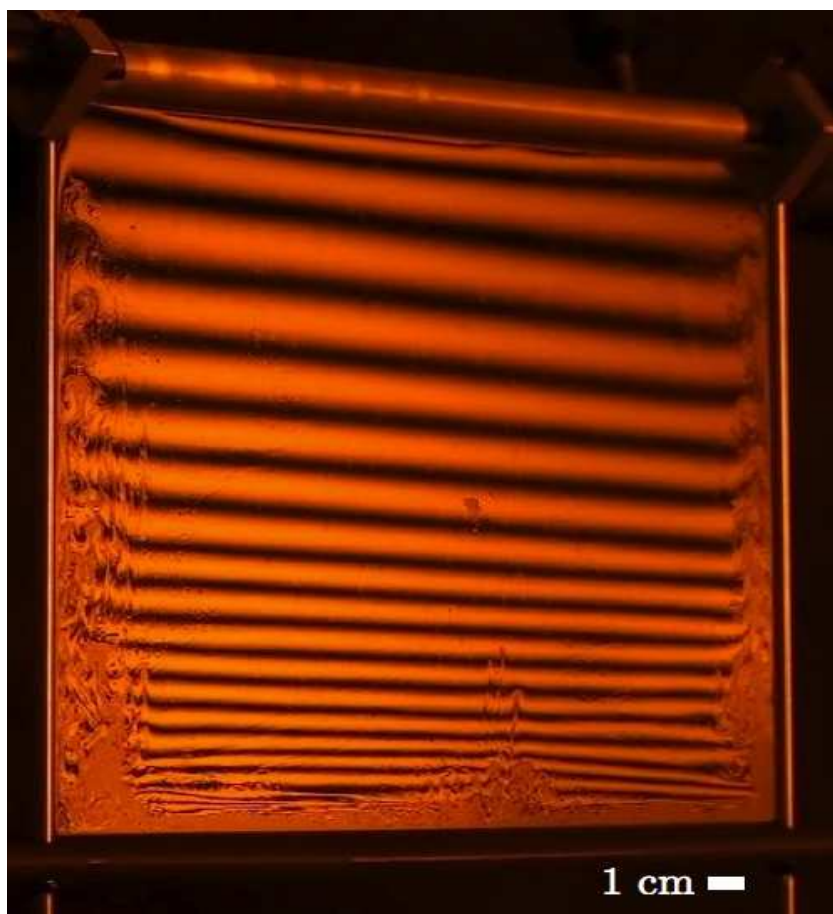


Figure 1.11: Picture of a vertical soap film lit with a sodium vapor lamp.

the fringes are moving downward. Moreover, the distance between the fringes may increase with time. The fringe profile stretches while getting down. Since interference fringes are associated to constant thicknesses values, this downward motion evidences that the thickness profile gets down in the film, i.e. that the film thins with time and space.

If one gently blows on a soap film sustained by a frame, it is possible to create a soap bubble. As evoked in Section 1.2.1, the spherical shape adopted by bubbles results from the surface minimization principle. After their formation, these bubbles exhibit fringe patterns, similar to the one exhibited by soap films [32]. Once again, those fringes move downward, attesting from the thinning of the bubbles walls.

It is interesting to remark that it is impossible to make a sphere out of a sheet of any solid material, while it is possible to obtain a spherical soap bubble out of an initially planar soap film. This feature is indeed specific to soapy objects, and must be regarded as a consequence of the relative weakness of interactions between surfactant molecules at the interfaces.

1.7.1 Soap film thinning

Two different phenomena can be pointed out as responsible for the vertical soap film thickness evolution. First, the fluid imprisoned between the film interfaces flows downward (see Fig. 1.12). This flow leads to liquid lacks between the interfaces, putting them closer to each other. This explanation represents the most common interpretation in order to justify the film thinning, and is usually referred to the drainage of soap films. The second contribution comes from the elasticity of the film interfaces. As evoked previously, surfactant layers are prone to stretch under the appliance of external constraints. In the particular case of vertical soap film interfaces, a constant constraint is applied on every point of the interfaces by the gravity. Depending on the interfacial elasticity linked to the surfactant, the thinning of a soap film can either result from a Poiseuille-like downward drainage flow of the inner film between the interface (high elastic modulus) or a combination of such flows with a gravitational stretching of the film (low elastic modulus). As a consequence, the higher the surface dilatational modulus is, the slower is the drainage. This effect has been evidenced for SLES+CAPB solutions [14], and for other surfactants [28]. Since the elastic modulus linked to our solution is rather low (~ 4 mN/m [14]), the soap films used in our experiments are likely to stretch under the action of the gravity.

Following the nature of the surfactant molecules, the film interfaces can either be mobile (the film elements are prone to displace with respect to the interfaces) or immobile and behave almost like the solid walls of a Hele-Shaw cell [10–12, 30]. Small surfactant molecules like SDS are known to generate mobile interfaces, while

bigger molecules such as Triton X-100 and proteins lead to immobile interfaces. This mobility is formalized by the interfacial viscosity of the surfactant layer [33]. By analogy with the usual viscosity, the interfacial viscosity represents the losses linked to the shears and the dilatations encountered by the interface.

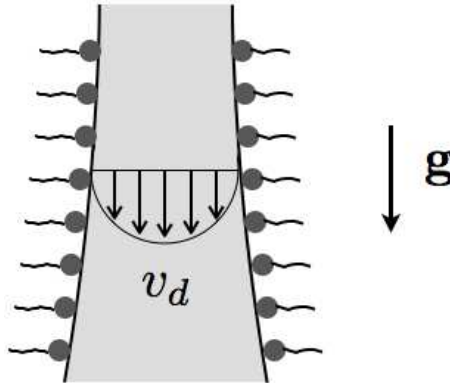


Figure 1.12: Schematics of a transverse cut of a draining soapy object. Following the mobile or immobile nature of surfactant molecules, this cut is either drawn in the lab or in the interfaces referential.

The mobility of the surfactant molecules (the viscosity of the film interfaces) influences the drainage occurring between the film interfaces. If the interfaces are covered with mobile surfactant molecules (low surface viscosity), they are dragged by the draining fluid, leading to a global plug flow. On the other hand, if the interfaces are immobile (high surface viscosity), then the drainage flow reduces to a Poiseuille flow. From a phenomenological point of view, the inner fluid should drain easier if the film interfaces are mobile. Mobile surfactant should then lead to faster drainages. Different works have emphasized the influence of the surface viscosity on fluid systems such as soap films during their drainage [34] and formation [35]. Recent studies on antibubbles [36] made with different surfactant solution, among which a SLES+CAPB solution similar to the one we used in all our experiments have shown that the surface viscosity plays a crucial role in the drainage mechanism responsible for the aging of the antibubbles. As a consequence, and even if not further taken into account in our modelings, the surface viscosity of the interfaces of soap films should be kept in mind. The SDS surface viscosity has been measured to be of the order of $3 \cdot 10^{-6} \text{ Pa} \cdot \text{s} \cdot \text{m}$ by various authors [35, 37, 38]. As a comparison, the surface viscosity of the SLES+CAPB solution has been determined by Scheid and coworkers to be of the order of $2 \cdot 10^{-3} \text{ Pa} \cdot \text{s} \cdot \text{m}$.

In the end, since our soap films are built out of a soap solution characterized by a low elasticity modulus and a low surface viscosity [14], their thinning must be considered as resulting from both stretching and drainage of the inner fluid between the interfaces.

1.7.2 Surface viscosity and interfacial equilibrium

Let us consider a solution made of small surfactant molecules with a low surface viscosity (e.g. SDS, SLES+CAPB...). Even if the surfactant is characterized by a low surface viscosity, the fact that this solution leads to soap films with mobile interfaces might not be that obvious. Vassilief and coworkers have investigated the lifetime of soap films as a function of the surfactant solution [19]. The observations brought increasing soap film lifetimes with increasing concentrations below the cmc. The larger lifetimes are obtained with the concentrations close to the cmc. Beyond the cmc the lifetime decreases again. Those results are interpreted by the authors by evoking the dynamical equilibrium between the interstitial fluid and the film interfaces. Below the cmc, the interface elasticity is governed by the equilibrium between the bulk and the interfaces [10–12, 19, 30]. Close to the cmc, both the adsorption layers and the interfaces are saturated in surfactant molecules, so that exchanges between the bulk and the interfaces become limited. This case leads to the most stable state for the interfaces, which are said to be tangentially immobile [10–12, 19, 30]. This case is somehow similar to the one of rigid interfaces obtained with big molecules, but results from a particular case of chemical equilibrium. Above the cmc, structures present in the bulk may adsorb and disintegrate at the interfaces, similarly to what happens on a planar interface (see section 1.5.2 and Fig. 1.8). Once again, those structures may act as extra-amounts of surfactant molecules, and may be responsible for elasticity and/or surface viscosity modifications, leading to a decrease of the soap film lifetime [19]. Those results evidence that the viscosity and the elasticity of soap films interfaces can exhibit consequent variations with the concentration and composition of the solution, even for small surfactant molecules which are *a priori* supposed to lead to mobile and stretchable interfaces.

Note that such phenomena can be observed with our solution. Monochromatic lightning of fed soap films (see next Chapter) have revealed that their interfaces can appear to be very viscous and fixed following the surfactant concentration of the solution. The corresponding fringe pattern does not seem to exhibit any stretching, as awaited with mobile interfaces. Figure 1.13 illustrates the case of a film made out of a SLES+CAPB+0.3% of glycerol. The top of the film is characterized by the awaited mobile interfaces, while the bottom exhibits quite frozen interfaces. This is evidenced by the difference in morphology of the fringe pattern between the top and the bottom of the film. On the other hand, more diluted or

concentrated solutions exhibit stretchings of the fringe patterns, as well as homogeneous interfaces such as presented in Figure 1.11. Those phenomena are very important for our experiments. The convection experiments presented in Chapter 5 have revealed that the experimental results drastically change if obtained with homogeneous or non-homogeneous soap films. It is thus very important to check the homogeneity of the film interfaces before starting any experiment using the corresponding solution. For the particular case of the SLES+CAPB, the interface homogeneity can be obtained by artificially aging the solution. This is achieved by mixing the solution during a few hours (typically 3) right after it was built. Repeating this procedure before using the solutions in experiments allowed to obtain homogeneous interfaces. Images such as Figures 1.11 and 1.13 were systematically used before starting the experiments in order to ensure of the interface homogeneity. If necessary, the sodium lamp was then turned off before the experiment is started.

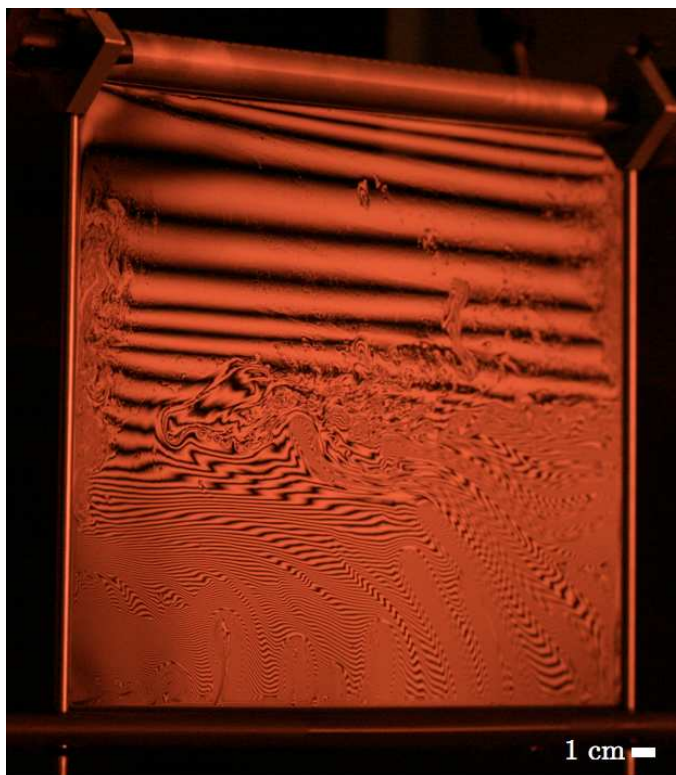


Figure 1.13: Image of a film presenting inhomogeneous interfaces. The bottom part of the film is characterized by viscous interfaces, what is evidenced by the important inhomogeneity of the fringe pattern versus the horizontal coordinate. In opposition, the fringes present at the top of the film do not exhibit such inhomogeneities, what is the signature of mobile interfaces.

1.8 Marginal regeneration

Until now, we did not discuss on the boundary conditions linked to a soap film. However, typical phenomena occur in the vicinity of the frame sustaining the film. We will consider the example of a soap film as obtained by pulling out a square frame out of soapy water. Frames are usually made of stainless steel rods or fishing lines, depending on the experiment to be performed. As previously mentioned, the typical soap film thickness is a few micrometers. Except for extreme cases, the physical borders of the frame are always thicker than the film they define. As a consequence, menisci are present between those borders and the soap film. This is sketched in Figure 1.14. Those menisci are called the Plateau borders of the film [39], and result from the hydro affinities of the surfactant solution with respect to the frame material [1]. Figure 1.14 illustrates that such menisci induce local curvatures of the soap films. They can also exist without the presence of physical boundaries. For example, bubbles forming a foam always link to each other by forming menisci [13, 40]. The meetings of those menisci create fluid channels between the foam bubbles, known as the Plateau borders in foam, and accounting in numerous foam phenomena such as drainage, elasticity... [13, 40].

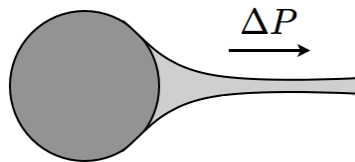


Figure 1.14: Sketch of a transverse cut of the Plateau border linking the film (light grey) to the sustaining frame (dark grey-not to scale).

Due to the induced curvature, pressure gradients exist between the Plateau borders and the “bulk” of the film, as schematized in Figure 1.14, implying that the “bulk” film regions are perpetually sucked toward the borders [1, 30, 41–43]. Those suction influences the film thinning in two different ways. First, as liquid is injected from the bulk toward the Plateau borders, downward flows appear in the channels they define. This effect must be considered as an indirect enhance of downward drainage phenomena, and is known to drastically influence foam properties [13, 40]. The second effect can be evidenced by simple observation of any vertical soap film in free drainage state, as is illustrated in Figure 1.15. While the upper and central regions of the film present homogeneous fringe patterns, the lateral and bottom edges present inhomogeneities. Careful observations also evidence that these inhomogeneities are film elements which are released by the borders of the frame and are driven by an upward motion, whatever the release

place in the film. Note that such releases by the borders are especially observed when the film is set vertically. In any case, the existence of menisci in the films imply fluid losses in Plateau border. As a consequence, soap films always drain, and so, are unstable in time, whatever their geometrical configuration.

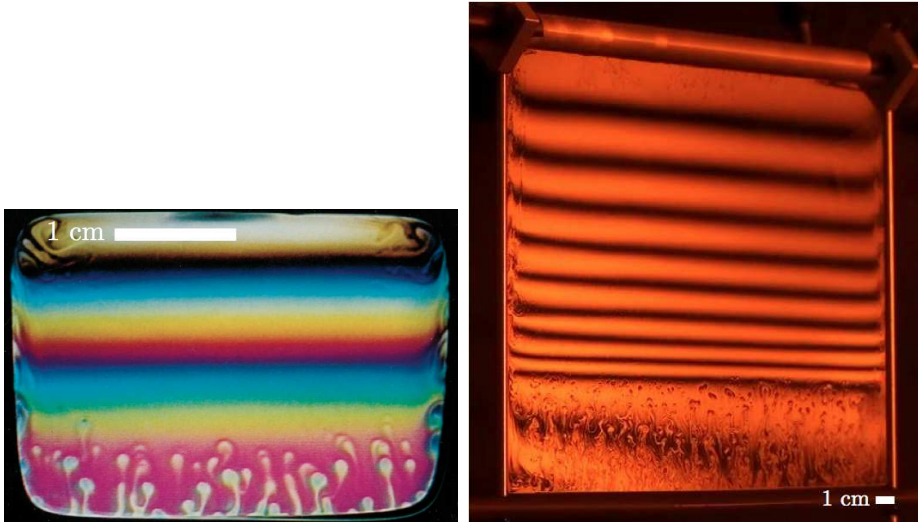


Figure 1.15: Pictures of vertical soap films in free drainage state illustrating the marginal regeneration phenomenon. Left : picture extracted from [41,42]. Right : picture taken with HD camera. The soap film is built from the solution described previously. Those pictures show that film particle flows develop from the bottom border of the frame to higher regions of the film. The fact that the color of these particles is different from the one of their surroundings illustrates the corresponding thickness difference.

Figure 1.15 left shows that the color of those released film elements is different from the one of their surroundings, which is the optical signature of a thickness difference between both [4,30]. The common interpretation of this phenomenon is that central film elements are sucked in the borders by capillary pressure gradients in the first time, and are then released from those borders with a different thickness than their surroundings [30,41,42]. This phenomenon is called the marginal regeneration of film elements and can be evidenced in the vicinity of any meniscus present in the film, whatever the origin of the meniscus [30,41,42]. The fact that regenerated film particles are buoyant comes from the existence of those thickness differences and will be discussed in more details in Chapter 4 [15,44]. Analyses of the buoyant forces acting on the regenerated particles show that they must be thinner than their surroundings for rising up. Consequently, marginal regeneration tends to thin the film by creating thin film elements, which occupy the upper

regions of the film acting as enhancing agents for the film thinning.

As explained by Nierstrasz and coworkers [41,42], the release of thin particles originates in an instability of the particles sucked in the menisci. Let us consider a film particle in the vicinity of the meniscus. We assume that the molecules present at the particle interfaces remain at the interface whatever the phenomena encountered by the particle. We also assume that the volume of the particle remains constant during the meniscus entry. As the particle enters in the meniscus, its thickness increases while the area sustained by its interface decreases, as schematized in Figure 1.16 extracted from [42]. This interfacial area decrease implies that the surface pressure of the particle increases as it enters in the meniscus. The fact that the number of surfactant molecules remains unchanged while particle enters in the meniscus is equivalent to suppose that those interfacial molecules do not have the time to dissolve in the particle bulk during the compression.

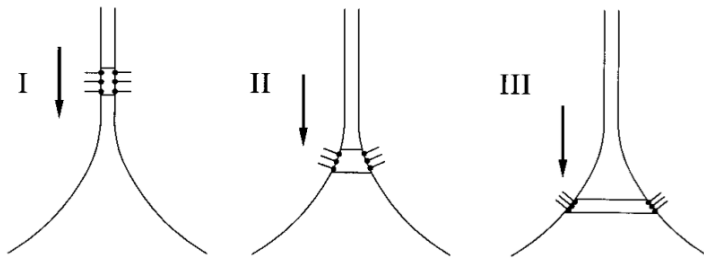


FIG. 6. Compression of a film element at the lower Plateau border (schematic).

Figure 1.16: Schematics of the interfacial compression encountered by a film particle while entering in the meniscus (from [42]).

The particle is then released out of the Plateau border, the release being supposed to result from an interfacial instability due to their large surface pressure regarded to typical values expected in the film [41, 42].

The fact that the released particle goes back into the bulk of the film implies that its characteristics must somehow fit with its surroundings, ensuring the continuity of the film. Since fluid has been released in the Plateau border, regenerated particles must be thinner than their surroundings. In order to have a similar volume to the typical particle volume at the considered position, their area expands. This is the reason why regenerated particles appear as macroscopic film elements, making them easy to see, even by naked eyes. Note that this area expansion right after the release is compatible with both the fact that inner liquid is lost in the Plateau border and that the surface pressure of the particles in the meniscus is higher than the typical surface pressure at the considered position. That is to say, the released particle must encounter Marangoni stretches. Eventually, it should

be mentioned that the marginal regeneration phenomena only concern films with mobile interfaces. In fact, rigid interfaces are incompatible with the compression encountered by film particles while entering the meniscus, as well as the relaxation they exhibit after the release [30].

1.9 Some previous experiments

Even if interesting by themselves, vertical soap films have been widely used in the last decades because of their ability to materialize almost ideal bi-dimensional fluid systems. Basically, the idea is to use vertical soap films as bi-dimensional channels in which a magnitude-controlled flow can be injected [15, 45–47]. Those nearly bi-dimensional channels have been intensively implied in experiments about turbulence [15, 45–50], using setups such as schematized in Figure 1.17 (from [50]). The right part of Figure 1.17 is a picture of the flow pattern obtained by introducing a cylinder normally to the film interfaces. Similarly to the three-dimensional case, the cylinder wake exhibits regular emission of eddies, forming a so-called Von Karman street. Those streets are known to develop for Reynolds number of the order of 1000 [2, 3], implying flow rates in the film of several meters per second.

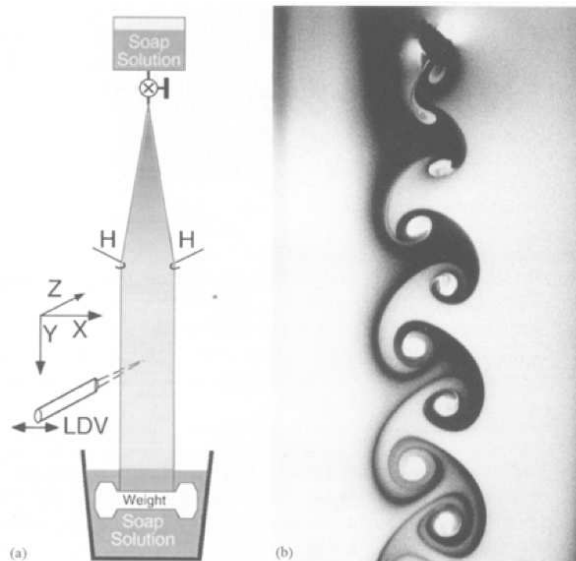


Fig. 1. (a) Experimental setup, (b) film thickness variations behind a cylinder, and (c) film thickness variations behind a comb. The diameter of the cylinder was 0.2 cm and the tooth spacing of the comb was 0.3 cm. The mean speed of the flow was 2 m/s. The snapshots (b) and (c) were taken under a sodium lamp.

Figure 1.17: Left : scheme of a typical setup used to produce nearly bi-dimensional fluid channels. Right : Von Karman street produced by introducing a cylinder in a fast flowing soap film (from [50]).

Figure 1.18 is a picture of the flow pattern obtained by introducing a comb normally to the film [51]. The introduction of such combs through the film generates a mixing of the different Von-Karman streets, leading to the turbulence of the different fields characterizing the perturbed soap film (thickness, velocity...) [52]. Those kinds of experiments have allowed to test bi-dimensional turbulence theories and have confirmed the existence of predicted phenomena such as inverse energy cascade for bi-dimensional turbulence [53]. They also brought confirmations of the validity of the adapted Kolmogorov theories for power spectra of turbulent fields [51–53].



Figure 1.18: Picture of the wake below a comb set into a flowing soap film (from [51]) The visualization of the interference pattern is obtained by lighting the film with monochromatic light (Sodium lamp).

Still in the field of turbulence, soap films can be used to perform bi-dimensional thermal turbulence experiments. Works such as done by Wu [54], Zhang [55, 56], Martin [57] and Zhong [58] have revealed that soap films can be used as bi-dimensional Rayleigh-Bénard cells. Applying a temperature difference to a vertical soap film allows to maintain it during several hours even if no flow is injected [54–57]. This has been pointed as the sign of upward convective motions due to the temperature difference between the top and the bottom of the film.

The thickness and velocity fields of such films have been experimentally investigated and exhibit turbulent behaviors as well [54]. Nevertheless, there is still a lack of confirmation concerning the corresponding thermal turbulence theories (Bolgiano-Ubohkov) [53, 56].

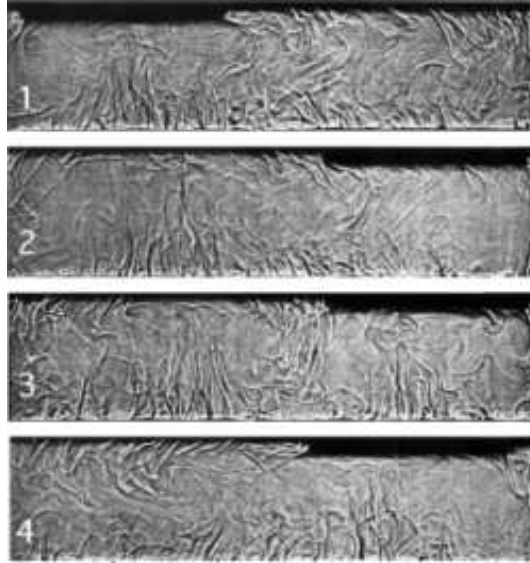


Figure 1.19: Shadowgraphs of a vertical soap film submitted to a vertical temperature gradient (from [58]).

Still in the thermal constraint concerns, Winkler and coworkers have applied a local cooling on vertical soap films. They observed the opposite behavior than for heated films. Indeed, they noticed an increase of the drainage velocity (see Fig. 1.20). Some kind of negatively buoyant flows develop from the cooling point, leading to a substantial increase of the thinning velocity [59].

Bi-dimensional channels have also been used to investigate the behavior of flexible filaments set in fast laminar flows [60, 61]. Following the magnitude of the Reynolds number and geometrico-physical characteristics of the filaments, these latter may start to interact with the flow, due to the Von-Karman street-like perturbations they induce [61]. Figure 1.21 shows several pictures of a filament set in a fast flowing film. Experiments such as described in [60] and using such filaments have shown the influence of elasticity on the drag force acting on a solid object submitted to a fast flow rate.

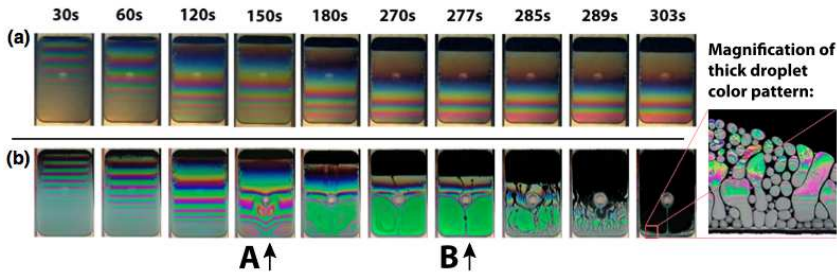
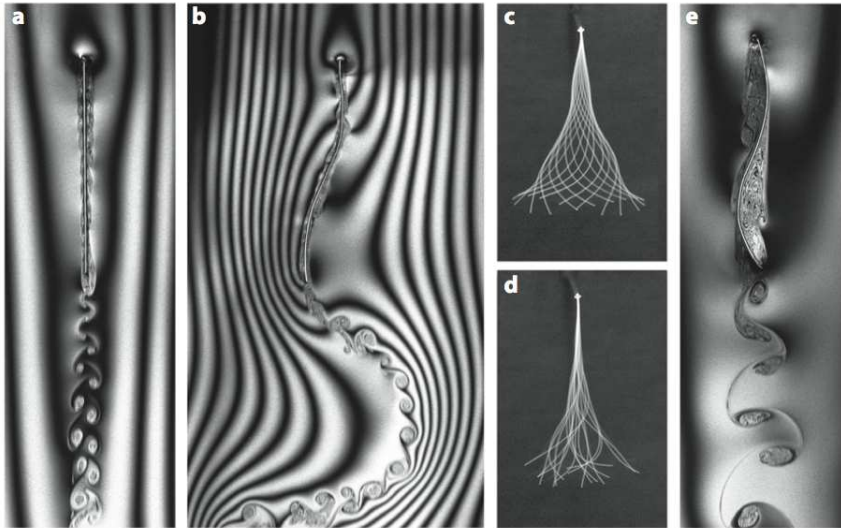


FIG. 2 (color online). Image sequences of foam film thinning. Thinning behavior of a foam film (a) without, and (b) with thermal forcing. While the undisturbed thinning (top) evolves slowly, the thermally driven flow (bottom) exhibits convection, with rapid transport and mixing. A: start of convection, B: onset of exponential thinning. One clearly recognizes the black film spots which are stretched and folded, such that by a rapid conversion the film evolves to the BF equilibrium phase. The magnification at the right shows the following: domains of thick film are surrounded by black film, such that the combination of forces produces an approximately spherical cap, with the lower plane part parallel to the foam film. Consequently, the $(2n + 1)\frac{\lambda}{4}$ condition does not hold anymore since it is based on the reflection between two parallel planes.

Figure 1.20: Comparison of several drainage states between an unperturbed and a cooled soap film (from [59]).

To conclude this brief and non-exhaustive overview on the previous studies, let us mention that several modelings have been developed in order to predict the shape, the lifetime and the dynamical properties of those films. Those models are mainly based on the thermodynamical descriptions of surfactant layers [15], on parameters such as surface elasticity [28] and surface viscosity [34, 35]. Some models have successfully reproduced soap film features as observed in the early works by Mysels and coworkers [30, 35, 62]. Among others, one can cite the concave-in and concave-out nature of the thickness profiles as a function of the bulk concentration in surfactant [62]. Even if *a priori* suited to predict the features of soap films, it is necessary to be careful when using those models. Indeed, they imply physical quantities such as the surface viscosity, which is prone to slightly influence the results. From the experimental point of view, the value adopted by those parameters depends on the physical chemistry of the surfactant used to make the film. It is known that the interfacial rheology of surfactants such as proteins is subject to present considerable evolutions with time and/or experimental solution [14]. As a consequence, it is important that the different hypothesis and conditions considered in the models are experimentally checked before using any theoretical description.

**Figure 2**

(*a,b*) Flow visualization of the wake structure downstream of a flexible filament made of silk thread and immersed in a running soap film. The light-dark bands are interference fringes created by reflection of a monochromatic light source. (*a*) The stretched-straight state. (*b*) Flapping. (*c*) A coherently flapping filament at several time points along its flapping cycle. (*d*) The same filament at higher flow speed, showing aperiodic flapping. (*e*) The flow around a stiff metal wire bent permanently into the shape of a flapping filament.

Figure 1.21: Images of a flapping elastic filament set in a fast flowing vertical soap film (from [61]). The film is lighted by a Sodium lamp.

1.10 Position of the problem

The purpose of the present thesis is to realize innovative experiments aiming to enlighten soap film features which have not been investigated yet. Since consequent work have already been performed on topics such as thinning and turbulence, we challenged ourselves in designing experiments involving our personal view of vertical soap film and which are attached to the basic present questions about soap film phenomenology.

The experiments presented in the previous section are so that they are not submitted to the soap film lifetimes, due to the convection they imply (thermal constraints), their flowing nature (bi-dimensional channels) or their solidity, conferred by both their small size and building surfactant (local cooling). As a consequence of their considerable lifetimes, those films are pretty well suited to realize experiments on large timescales. This convenience is attractive, because it allows to design experiments without caring about the solidity of the films. Extreme experiments can then be envisaged.

Except for the case of fast flowing fluids, nearly all the experiments performed with soap film imply very small films (1cm^2), the fact being that smaller films tend to live longer. Observation of soap film behaviors with the size of the sustaining

frame shows that small films tend to live longer than larger ones, what justifies the choice of small soap films in numerous experiments.

As presented in the following chapters, the experiments we realized on vertical soap films systematically imply the introduction of solid objects within the film, i.e. objects which are prone to significantly affect the continuity of the film interfaces (solid rods, pipes, sensors...). Basic tests about the introduction of solid objects in vertical soap films suggest that those intruders are often harmful for the films, in the sense that they cause their burst. For the purpose of our experiments, it was then necessary to build soap films which are as resistant as possible to the external constraints.

The typical size of the objects to be introduced in the films is of the order of several centimeters. In opposition to the previously evoked small-scale experiments, it was then necessary to build soap films which are at least an order of magnitude larger than those objects, say of the order of 10 cm in height. This relatively large size goes across the fact that large film tend to be brittle. We thus proposed a method to enhance those large soap films lifetime.

Experiments such as represented by Figure 1.18 and Figure 1.21 show that introducing large scale objects in soap films is possible if those latter are fed by imposed flows. In opposition to those experiments, we wished to avoid the convective features of those setups, i.e. we wished to work with large scale soap films which are not bi-dimensional channels characterized by high downward flow velocities. We thus designed a setup which aims to stabilize the thickness profile of the soap films in time, i.e. which avoids the thinning which would be observed in any point of a free-draining vertical film. This setup is presented and characterized in Chapter 2. We show that it is possible to fix the thickness profile by using devices such as presented in Figure 1.17 and avoiding fast convective downward flows at the same time. The corresponding thickness profiles are characterized by a method presented in Chapter 2.

In Chapter 3, we explain how it is possible to use the elasticity theory to probe the surface tension profiles in our maintained soap films. This experiment also shows that our films are suited for introducing solid objects within them.

Chapter 4 discusses an experiment aiming to investigate the buoyancy phenomenon in the particular case of vertical soap films. The results brought by these experiments are faithfully modeled using the surface tension profile characterizations presented in Chapter 3.

In Chapter 5, we present an experiment which can be seen as a mix of the experiment described in Chapter 4 with the thermal turbulence experiments presented in the previous section. From a phenomenological point of view, this experiment is the opposite of the one realized by Winkler and coworkers (see Fig. 1.20) in the sense that we applied a heating rather than a cooling to our films.

Chapter 2

Thickness profiles of fed soap films

If one pulls a frame out of soapy water, a soap film is generated inside the frame [1, 2, 13, 63]. If enlightened with monochromatic light (e.g. from a Na_2 lamp), the film exhibits an interference fringe pattern (Fig 2.1), attesting for the existence of a vertical thickness profile in the film [13,63]. Temporal investigations of such freely suspended soap films reveal that the fringe pattern (and so the related thickness profile) evolves in time. Figure 2.2 represents the spatio-temporal evolution of the fringe pattern of a freely suspended vertical soap film. This picture is obtained by gluing the images of vertical pixel column, frame by frame. One sees that an almost fixed fringe pattern is present at early times. Then the fringes start to get down toward the bottom of the sustaining frame, until the film bursts (black area for large times). Quantitative analyses show that vertical freely suspended soap films thin with time. This thinning is mainly due to gravitational flow of the solution between the film interfaces [1, 13, 63], eventually coupled to interfacial stretching for surfactant characterized by weak surface moduli. This thinning implies a finite lifetime for the soap films, which depends on the kind of surfactant used, and can vary from a few seconds to several hours [64]. Depending on the phenomenon to be investigated, this relative shortness of the film lifetime can be quite limiting. In this chapter, we describe and characterize the experimental setup we developed and used to extend considerably our soap film lifetimes. We show that it is possible to suppress the temporal evolution of both the fringe pattern and the thickness profile of these films. We then explain how we characterized the time-fixed thickness profiles as functions of the experimental parameters.

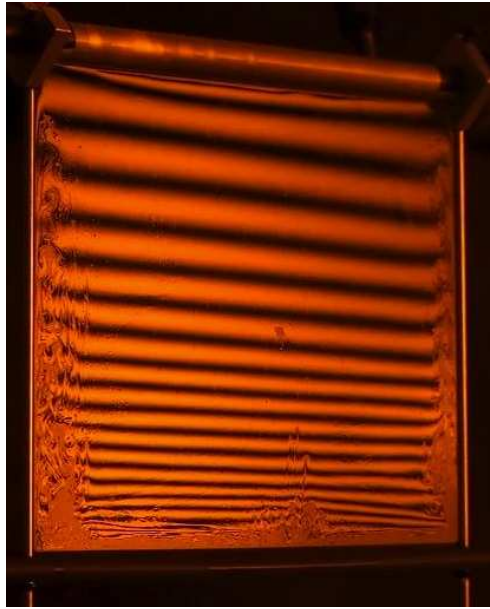


Figure 2.1: Fringe pattern in a soap film illuminated with a monochromatic light (Sodium lamp). The areas near the lateral and bottom edges are marginal regeneration fluxes occurring in the linking menisci (see Chapter 1 for details). Those fluxes are responsible for the perturbation of the fringe pattern in those areas.



Figure 2.2: Spatio temporal diagram of the fringe pattern of a freely suspended vertical soap film. The black area for larger times corresponds to the film rupture.

2.1 Experimental setup

For the purpose of our experiments, we wished to design a setup allowing to generate vertical soap films which can last for several minutes/hours. There are different ways of avoiding the thinning phenomena due to gravity [65–67]. For instance, it has been shown that it is possible to strongly influence, and even to reverse, the drainage by loading the building solution with magnetic particles [65, 66]. The appliance of a carefully chosen magnetic field allows to slow down the inner drainage flows in the film [65]. If strong enough, the magnetic constraint can even be used to reverse the drainage direction, i.e. to make the building solution rising between the film interfaces against gravity [66].

If ionic surfactant molecules are used to build a surfactant solution, this solution contains ions. Electric fields have been applied to study both the electrical properties and the effects of the electric constraint on the corresponding film behaviors. Those studies revealed that it is possible to induce flows which are such that the lifetime of the film is increased [67].

However, the control offered by those methods on soap film inner flows remains quite poor. Moreover, those methods may require additions of designed chemical species in the building solution in order to work efficiently. These additional components may lead to modifications of the interfacial behaviors of the surfactant molecules.

The method we used is based on the hydrodynamics of the drainage itself. Since the drainage phenomenon tends to empty the film from the fluid lying between its interfaces, we thought of continuously filling the film with its building solution, so that the draining fluid is always renewed. This situation is analogous to the one of a vertical pipe filled with water and holed at the bottom. Due to gravity, water comes out of the pipe with a given flow, depending of the radius of the hole as well as of its relative position to the top free interface. It is possible to keep the pipe constantly filled if water is injected with a flow which compensates the drainage. The main difference with our soap films is that the interfaces flow with the inner fluid, as a consequence of the stretching. The re-filling of our films then implies both fresh inner fluid and interfaces supplies.

To maintain our vertical soap films, we built a setup inspired from falling liquid curtain experiments described in [69] and [70]. The idea is to replace the top edge of the sustaining frame by a hollow anodized aluminium pipe (visible in Figure 2.1). A constant flow can then be established in the pipe thanks to a devoted device (constant flow pump, syringe puller...). The feeding is done by a series of holes disposed on a longitudinal axis of the pipe, and equally spaced, as schematized in Figure 2.3. Those holes are set upward, so that a constant overflow comes out of the pipe. The soapy solution then flows along the edges of the pipe until it reaches the top meniscus linking the soap film to the pipe. We tested the con-

figuration with the holes pointing downward, and observed that fast downward streets form in the film. In addition, the solution tends to mainly come out of the pipe by the holes which are close to the pipe extremities, inducing spatial inhomogeneities in the feeding.

The holes diameter has been fixed to $800 \mu\text{m}$, and they are apart from 2.5 mm . With this diameter, we get equal overflows from every hole. For larger holes the soapy solution may overflow by a randomly selected hole, leading to an inhomogeneous feeding. The same kind of problem can arise if the holes are replaced by a slot, as used in [69, 70]. Since the feeding flows used in our experiments are very weak, the width of the slot should be very weak as well in order to get homogeneous overflows. However, even for very thin slots, the system was quite unstable and rapidly led to flow inhomogeneities.

The lateral edges of the frame are made of two 3 mm in diameter stainless steel rods fixed to the pipe. The bottom edge of the frame is made of a 6.35 mm in diameter PVC rod. This rod is mobile in the vertical direction (i.e. the height of the frame can be tuned). This feature is necessary to initialize our fed soap films (see Section 2.2 for details). For all the experiments described in the next chapters, the dimensions are fixed so that the frame defines an area of $0.15 \times 0.15 \text{ m}^2$.

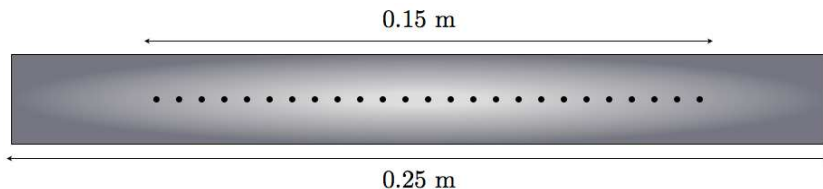


Figure 2.3: Scheme of the holed pipe used to create soft overflows.

We chose to use a surfactant mixture (SLES and CAPB) designed by Golemanov and coworkers to build our soap films [14]. After several tests, we decided to use a solution made of 3% of SLES+CAPB, plus 0.3% of glycerol diluted in bi-distilled water. This concentration represents five times the CMC. The solution is characterized by a surface tension of 29.8 mN/m (measured by the pending droplet method) and a kinematic viscosity of $1.09 \cdot 10^{-6} \text{ m}^2/\text{s}$ [68]. This solution allows to get soap films which are suited for our experiments : unwanted physico-chemical effects such as viscous interfaces or viscosity gradients at the interfaces are avoided (see Chapter 1 for details). Using this mixture allows to obtain soap films which are close to the general freely draining soap film idea, i.e. an interstitial fluid flowing between two soap film interfaces under the action of gravity, as well as mobile interfaces. As evoked in Chapter 1, the stretching of the films under their own weight participates to the global thinning, which is obviously the case for our fed

soap films. The main difference with the freely suspended films is that for any vertical position H in our films, the stretching constraint can be considered as fixed in time, since the thickness profiles are fixed in time (see next sections).

To maintain the film thickness constant, it is necessary to inject the solution in the pipe with an appropriate flow rate Q . Explorative investigations revealed that flow rates smaller than to 1.2-1.3 ml/min are too weak to maintain the thickness of the films. The temporal evolution of the fringe pattern at such small fluxes still shows a thinning. Higher Q values (1.5-1.6 ml/min) revealed suited to maintain soap films for timescales ranging from a tens of minute to an hour approximately. However, the corresponding films were very fragile and it was almost impossible to introduce any sensor or device without leading to their burst. Flow rates ranging from 1.8 to 2.2-2.3 ml/min were pointed to be adapted in maintaining films for large timescales (several hours and even more if wanted). We then decided to consider flow rates values Q included in [1.8-2.3] ml/min for all our experiments. Beyond 2.3-2.4 ml/min, the flow becomes too important to feed the film without imposing a boundary condition on the velocity field in the vicinity of the pipe. The flow coming from the holes becomes forced and cannot be considered as an overflow anymore. This forcing leads to fast downward streets in the film and subsequent strong inhomogeneities in the velocity field. This regime, which is close to the one usually used to create bi-dimensional turbulence in soap films [15, 46], results in some kind of a mix between the freely suspended soap film and free-falling liquid streets as described by Brunet and coworkers in [71, 72]. Though interesting, those cases are not discussed here.

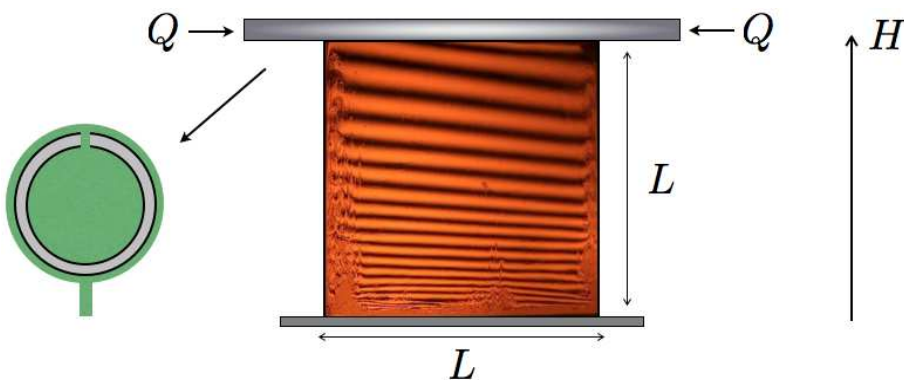


Figure 2.4: Schematics of the experimental setup used to generate maintained soap films ($L=0.15$ m). The left part represents the overflow of soapy solution (green) from the holes, followed by a swelling around the edge of the pipe (grey).

2.2 Soap film formation procedure

Injecting soapy solution with a weak flow (a few ml/min) in a vertical holed hollow pipe as presented in Figure 2.3, leads to droplet formations at the bottom of the pipe. As the flow rate is increased, droplets are generated with an increasing frequency, until the apparition of equally separated streets, as described in [71,72]. Even with high Q values, soap films never appear spontaneously : they have to be artificially initiated. The initialization is performed as follows : an important flow is injected in the pipe (~ 100 ml/min). Then the bottom edge of the frame is brought close to the top pipe in order to reduce the film height to approximately one centimeter. Then the experimenter passes its finger between the pipe and the PVC rod. This process leads to the apparition of a falling curtain between the pipe and the rod, instead of the natural liquid streets. The rod is then brought back to its rest position, so that the height of the film is 0.15 m again. The flow rate is then decreased to the wanted value. Figure 2.5 is a spatio-temporal diagram of the fringe pattern before and after the flow decrease. One sees that the decrease in Q is followed by the apparition of a narrow fringe pattern, which first gets down. After a few minutes (typically 3), the fringe pattern stabilizes. This spatio-temporal diagram was realized with images acquired at an acquisition frequency of 25 Hz, during 8 minutes. Since the fringe profile evolves rather slowly with time, we chose to keep 1 image per second. Figure 2.5 shows that our procedure is suited to obtain a fixed fringe pattern after a few minutes, and that this pattern can be maintained for several minutes after stabilization (at least 4 minutes as shown in Fig. 2.5). Common use of this setup and procedure revealed that the pattern can be maintained as long as wanted within the flow rate range mentioned above (see Section 2.1).

2.3 Thickness profiles of fed soap films

Spatio-temporal diagrams such as presented in Figure 2.5 evidence the efficiency of our setup to maintain stable fringe patterns/thickness profiles. However, they are not sufficient in order to grasp the effects of parameters such as the magnitude of the injected flow Q on the thickness profiles. It is thus necessary to design a method which aims to probe the thickness profiles in the films. Several ways can be used in order to realize such characterizations. Optical methods are the most commonly used. Due to their weak thickness, soap films are prone to behave as Fabry-Perrot interferometers for visible light (this is precisely the reason why interference fringes appear when films are lit with (mono)chromatic light (Fig. 2.1)). It can be shown from simple optics that the difference of optical path between two colored fringes (constructive interference) is an integer times the wavelength of the light used to make the fringes, say :

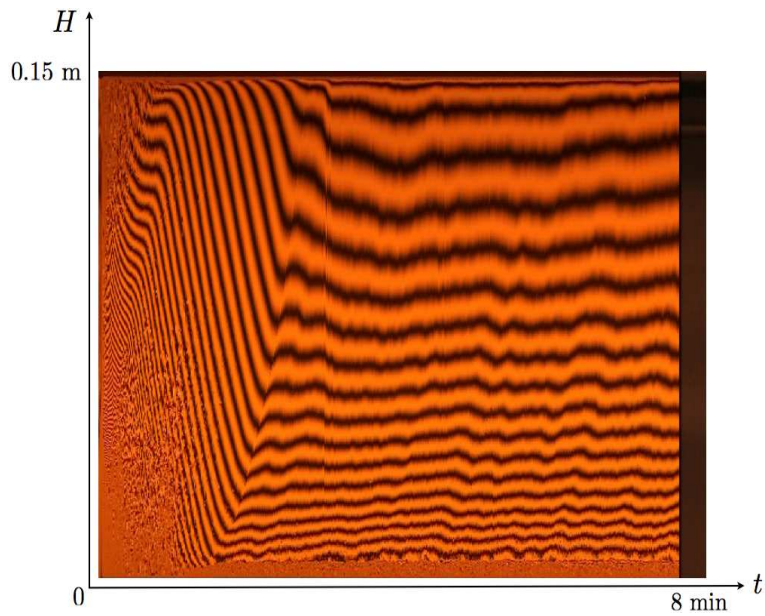


Figure 2.5: Spatio-temporal diagram of the fringe pattern during the soap film creation procedure. The black part for long times corresponds to the artificial film burst (performed by the experimenter). The maintaining flow is set to $Q = 1.9 \text{ ml/min}$.

$$n\lambda \sim \delta e, \quad (2.1)$$

with n an integer, λ the wavelength linked to the light responsible for the interference pattern and δe the thickness difference between the colored fringes. This formula can easily be used to estimate the thickness gradient in our films from images such as presented on Fig. 2.1. Knowing the wavelength of Sodium as being close to 589 nm, if e is the thickness profile in the film, one can estimate the thickness gradient as :

$$\frac{\delta e}{\delta h} \sim n \frac{\lambda}{h} \quad (2.2)$$

if δh is the considered height variation and n the corresponding number of constructive interferences. For $h \sim 10^{-2}$ m, we obtain that $\delta e/\delta h$ is of the order of $5 \cdot 10^{-5}$ for our maintained films. This estimation means that an increase in H of one meter lead to a thickness increase of several tens of microns in fed films.

Theoretically, it would be possible to get absolute thickness measurements from interference patterns. This would require to know a typical thickness state of the film, which could be used to iterate the thickness profile building procedure using Eq.(2.2). From this point of view, one could consider stopping the feeding flow and let the film thin until the common black film arises. Since this latter thickness can be determined from dynamical theory of surfactant molecules bilayers [1, 13], one can use this value to iterate and build the whole vertical thickness profile in the film. However, the thinning of soap film is prone to be rather discontinuous. In fact, as emphasize in [13], parameters such as the disjoining pressure are subject to present oscillatory behaviors versus thickness under the influences of various parameters such as the interactions occurring between surfactant molecules (small thickness) or stratification phenomena due to apparitions of organizations of inner fluid structures like micelles (larger thickness). Those phenomena imply discrete behaviors of the corresponding thickness when the film becomes very thin (close to the Newton black film state) [13, 73, 74]. The lack of knowledge about the disjoining pressure for our films in those thickness regimes makes the precise determination of the first value to be used for iteration rather impossible.

In addition to these phenomena occurring for small thickness values, discontinuities may also appear for thicker regimes. Figure 2.6 illustrates a discontinuity in the fringe profile occurring during the transition to the stable thickness regime of our fed soap films. This discontinuity can be observed in Figure 2.5 as well, appearing as the discontinuous line separating the decreasing and stable fringe regimes. A careful observation of the film interfaces above and below this discontinuity (see Fig. 2.6) suggests a modification of the interface properties between both parts (mobility, viscosity...). We have to underline that those kinds of discontinuities were only evidenced during the establishing regime of the fixed

thickness/fringe profiles, and are no more present once the film is stable. Nevertheless, it has to be considered as a source of ambiguity for an iterative building of thickness profiles from interference fringes.

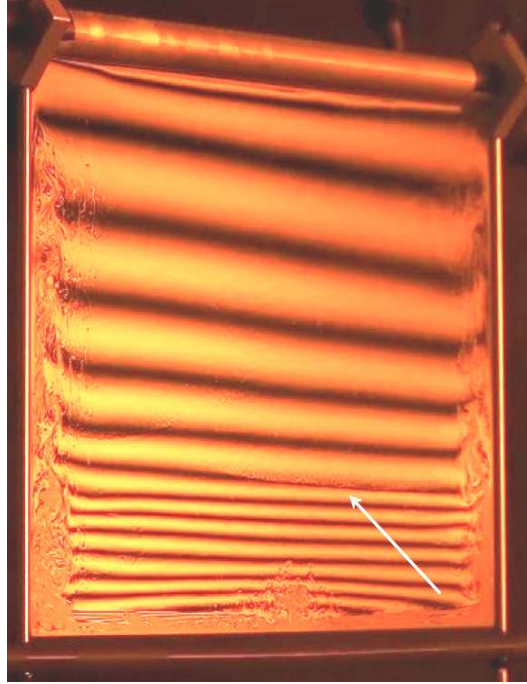


Figure 2.6: Thickness discontinuity in the transition state of a maintained soap film. The arrow indicates the boundary between both regimes.

Even if the pre-cited optic method may not be relevant, other more straightforward optic methods exist. Interferometric devices, such as the one used in [31, 75–78] allow to realize accurate thickness measurements in soap films. Their working principle is almost the same as explained above, with the difference that polychromatic light is used. It can be shown that the thickness is related to interferences corresponding to the different wavelengths present in the incident light, so that there is no more need for a reference value. The advantage of such polychromatic interference techniques is that it brings simple and fast thickness measurements. The disadvantage is that the sensor area is usually small (a few mm^2) compared to the film area, so that it can only provide local thickness measurements. On the other hand, it is very well suited to obtain time series in order to study the temporal thickness dynamics at a given position. Since our wish is to obtain thickness measurements on the whole film area, this method might not be adapted.

Electrical phenomena can also lead to thickness measurements. In fact, the appli-

ance of electric fields to soap films have shown to influence their thickness [67]. In addition, it can be shown that if the electric properties of the film are supposed to be the same as the one of the building solution, it is possible to determine the mean thickness of the film by electric measurements [79]. Similar measurements have been successfully realized in order to characterize the evolution of the liquid fraction in foams versus time [80]. The inconvenient of this technique is that it only gives access to a mean value of the thickness. It could be used, for example, to follow the evolution of the average thickness of the film as a function of the feeding flow, in order to get a partial quantification of the film thickness versus Q . However, it is unsuited to obtain thickness profiles.

2.4 Infrared thickness measurements

An alternative to the previously exposed methods is to use the water infrared absorption properties. Wu and coworkers have successfully experimented this technique in order to determine thickness profiles in fast flowing soap films [54]. It is known from infrared molecular spectroscopy that water molecules present an absorption peak near $\lambda \sim 3 \mu\text{m}$ (see Fig. 2.7). The authors of [54] then built a setup in order to measure the absorption of such a radiation by the soap film. This absorption can be related to the film thickness thanks to the Beer-Lambert law :

$$\frac{I_t}{I_0} = \frac{(1 - R)^2 \exp(-\mu e)}{1 - R^2 \exp(-2\mu e)}, \quad (2.3)$$

where I_t is the intensity transmitted through the film, I_0 is the intensity when no film is present between the source and the receptor, μ is the absorption coefficient of water at the considered wavelength (see Fig. 2.7), e the film thickness and R the reflectance of the film, given by $R = (n - 1)^2 / (n + 1)^2$ if n is the refraction index of water at the considered wavelength. It can be determined [54] that $n \sim 1.17$ for $\lambda \sim 3 \mu\text{m}$, bringing $R \sim 0.61\%$. The general Beer-Lambert law as defined by Eq.(2.3) can then be approximated as :

$$I_t = I_0 e^{-\mu e}. \quad (2.4)$$

If the absorption coefficient μ is known for the considered wavelength, it is then possible to obtain the thickness of the film from simple inversion of Eq.(2.4), say :

$$e = \frac{1}{\mu} \ln \frac{I_0}{I_t}. \quad (2.5)$$

Wu and coworkers used a diode emitting at $\lambda \sim 3 \mu\text{m}$ and an adequate photodiode in order to collect the transmitted light intensities. Since they fixed the wavelength in order to reach the optimal infrared absorption by water molecules,

they were able to make very accurate measurements of thickness in fast flowing soap films. Other studies used infrared absorption in order to perform thickness measurements [55]. The authors showed that the calculations mentioned above are relevant over a wide range of wavelengths extending from 3 to 14 μm [55].

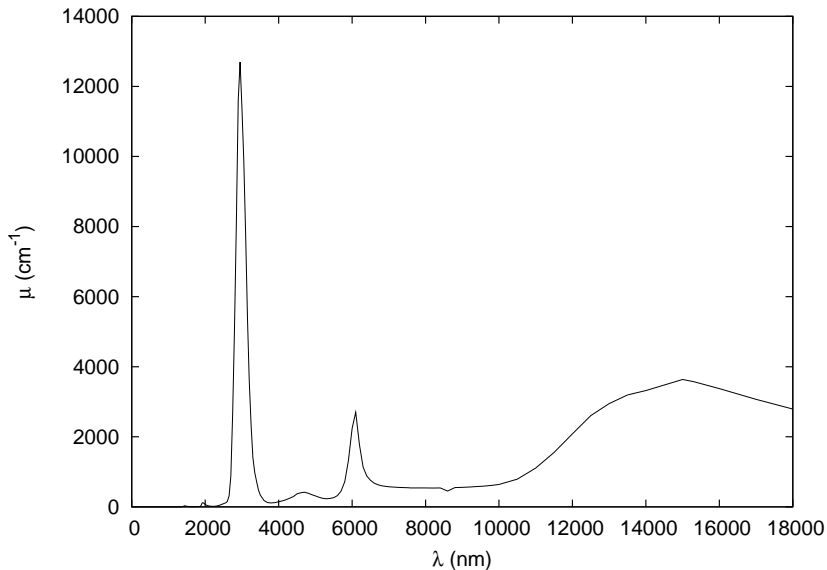


Figure 2.7: Absorption coefficient μ versus wavelength λ for water (extracted from [82]). One sees that μ remains almost constant for wavelengths close to 8 μm .

Although very well suited for thickness measurements, this method presents the same disadvantage than the optic interferometers : only very localized measurements can be performed. The transmitted infrared light is indeed collected over an area of $\sim 1 \text{ mm}^2$. Nevertheless, the general idea to use infrared absorption in order to realize soap film thickness measurements guided us in our developments .

2.4.1 Thermal camera

Rather than using small area sensors, we chose to use a FLIR thermal camera in order to perform extended thickness measurements, which works as follows. A devoted sensor (bolometer) detects the infrared radiations coming from the objects pointed by the camera lens (made out of germanium). Those radiations are then converted into grey levels for constructing a corresponding infrared image, with the intensity of grey levels proportional to the infrared intensity emitted by the object (see Fig. 2.8). Then the grey levels are converted to temperature measurements using a formula involving the distance between the camera and

the analyzed objects, the ambient air humidity and temperature, the infrared emission coefficient for the estimated temperature, etc... The infrared absorption coefficients of usual material are provided by the manufacturer [81].



Figure 2.8: Examples of infrared images obtained by the thermal camera. Up : this image is built with a level of 25°C and a range of 50°C . The settings of the camera are so that the thermalized bath, the lab environment and the experimenter are displayed. Down : the same situation filmed with a level of 65.5°C . Only the thermal bath is visible with these settings. The lab environment and the experimenter, though still present, are not displayed.

Even if the final purpose of the camera is to build thermal maps of given objects, we do not consider this function here. We decided to use this camera as an infrared imaging device rather than a thermometer. Settings proposed by the camera include the possibility to choose both the range and the position of the

temperature interval considered to build the infrared images. It is also possible to fix the “temperature of interest” value, which is the temperature value around which the temperature interval extends. Those functions act as filters which center and width can be tuned by the user. The temperature in the laboratory is typically 20°C, so that every object present in the laboratory is visible with the camera if the interest temperature is close to 20°C, even with a narrow width for the interest domain. On the other hand, if an object presents a higher temperature (say 100°C for example), it is possible to find parameters so that this solely object appears on the infrared images. We designed a setup based on this feature in order to realize thickness measurement of soap films over a wide area (typically $h \times w \text{ cm}^2$), with h and w representing the height and the width along which the measurements are performed. It should be mentioned that the infrared camera optics is quite limited, so that it can be difficult to obtain spatial and thermal resolution at the same time. A good compromise was obtained by setting the camera so that $h = 9 \text{ cm}$ and $w = 15 \text{ cm}$. The fact that h is smaller than L can appear as limiting at first glance. However, we wished to measure the thickness of our films in its central regions, so that the boundary conditions linked to the frame influence as less as possible the measurements. We set the camera so that the thickness measurement were taken from $\sim 1.5 \text{ cm}$ above the bottom edge of the frame to approximately 10 cm. This configuration was chosen in agreement with fringe patterns such as presented in Figure 2.1. Indeed, such images reveal that the distance between the fringes increases as they get closer to the top of the frame. Those regions are then subject to present less thickness variation with respect to the bottom regions. It is then logic to focus on the bottom/middle regions of the film, in order to capture the thickness dynamics as accurately as possible.

To generate a (to be) transmitted light source, we put a tank filled with thermalized water behind the film as schematized in Figure 2.9. We thermalized the water at a temperature of 80°C, allowing to get relevant infrared contrast with the lab environment. The tank was made of Pyrex, characterized by an emissivity of 97% [81]. Once the bath is thermalized, the interface of the tank pointing toward the film can be considered as an homogeneous infrared source.

The dependency of the absorption coefficient μ on the wavelength of the radiation can be found in [82]. Since the emissivity of Pyrex is close to unity (97%), the wall of the tank can be considered as a blackbody in first approximation. The typical wavelength associated to the bath temperature can then be evaluated using the Wien law, which determines the wavelength corresponding to the maximal intensity emitted by a perfect blackbody :

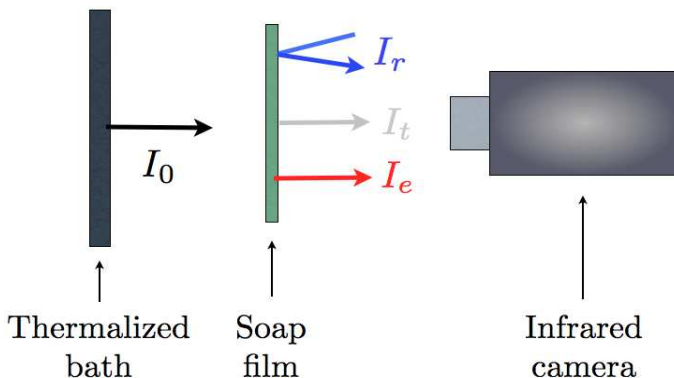


Figure 2.9: Scheme of the experimental setup used to perform thickness measurements on vertical soap films. The emitted I_e , transmitted I_t and reflected I_r intensities represented can be removed by adapted filter tuning.

$$\lambda_{max} = \frac{hc}{4.9651k_B T} = \frac{2.898e^{-3}}{T}, \quad (2.6)$$

with h the Planck constant, c the speed of light, k_B the Boltzmann constant and T the temperature. The typical wavelength associated to the thermalized bath determined by this expression is close to $8.3 \mu\text{m}$. From the tables contained in [82] it is possible to determine the absorption coefficient of water for the bath temperature. This coefficient only corresponds to the peak of maximum intensity of the corresponding blackbody. We performed analyses of the grey level fluctuations versus time at several positions in the film and observed that the displayed infrared intensities remain almost constant in time. The fluctuations were actually of the order of one grey level. Knowing the fact that the thermal camera collects the mean infrared intensity emitted by the object, independently of the intensity distribution of the corresponding blackbody, it is reasonable to consider that the collected intensities are related to a single wavelength given by Eq.(2.6). Moreover, μ remains almost constant around $8.3 \mu\text{m}$ (see Fig. 2.7), so that it can be considered as constant with respect to the wavelengths emitted by the bath. The infrared camera filter can then be tuned so that the intensities emitted by the bath and transmitted through the film are the only ones detected. Doing so, the intensities emitted by the film itself and its surroundings are pushed out of range. An example of the efficiency of such settings is given in Figure 2.8. Reflected intensities are considered as negligible since $R \sim 0.67\%$. Further damping of this component can be achieved by ensuring that no heat source is present in the lab (e.g. incandescent lamps).

The images acquired with this method are then be used to determine the original and transmitted intensities, and further, the corresponding thickness profiles.

From now, we will consider that the vertical coordinate H runs from the bottom to the top of the frame, as presented in Figs. 2.5 and 2.4 (i.e. H goes from the bottom edge of the frame against gravity). The corresponding typical accuracy can be computed from Eq.(2.5) with typical I_0 and I_t values. Considering that the grey values of the transmitted intensities are subject to a few units fluctuations, the typical resolution on the corresponding thickness is of the order of 10^{-7} m. Since the typical thickness of soap films is of the order of several microns, our infrared method can be considered as relevant in order to characterize our fed films.

In order to accurately characterize our films, we recorded long lasting infrared movies of our films in their steady state. We then considered spatio-temporal mappings of the thickness profiles in the films. These mappings averaged on both time and space in order to enhance the accuracy of the measurements. This spatio-temporal average was considered several tens of times for flow rates in [1.8:2.2] ml/min. The fully averaged curves are presented in Figure 2.10.

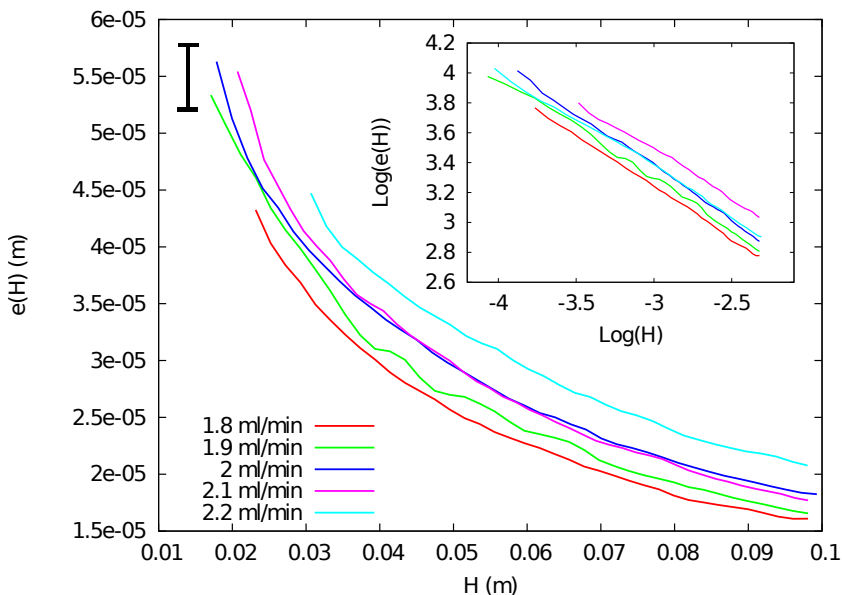


Figure 2.10: Averaged thickness profiles in maintained soap films versus vertical position in the film for several Q values. Inset : the same curve considered in logarithmic scale.

Some comments should be made about those curves. First, it is clear that increasing Q leads to an increase of the thickness for any value of H . This seems natural : the more the film is fed, the thicker it is. The error bar in Figure 2.10 corresponds to the standard deviation of the measurements around the mean pro-

file for each Q value. Its length is almost equal to the thickness range accessible within the considered Q range, what means that isolated thickness profiles corresponding to a fixed Q value are subject to consequent fluctuations. Statistics are thus required to obtain relevant measurements of the thickness profiles of our films. Several origins can be underlined for those fluctuations. First, experimental observation shows that downward flows occur in the lateral Plateau borders of the films. Those flows can be evidenced thanks to the droplets generated at the lower corners of the frame, implying that a part of the feeding flow goes in the Plateau border rather than in the film itself. This phenomenon is related to the marginal regeneration phenomenon evoked in Chapter 1. In order to estimate the influence of this phenomenon on the net feeding flow value, velocity measurements thanks to a PIV method could be correlated to thickness measurements, provided the seeding of the solution does not affect the infrared absorption, nor the intrinsic properties of the films.

At the molecular scale, another effect which could account in this dispersion is the stratification and self-organized structures induced phenomena. In fact, the picture presented in Fig. 2.6 suggests that such phenomena can occur in our maintained films. It has been emphasized in Chapter 1 that the soap film thinning can be influenced by micelle adsorptions at the interface for bulk concentrations higher than the CMC [19]. The typical concentration of our solutions is approximately equal to five times the CMC, so that such phenomena are likely to happen in our films.

Another cause of fluctuation is the history of the surfactant layers defining the film interfaces. In fact, even if the initialization procedure is repeated at identical from one film to the other, the initial state of the interfaces may not always be the same. As previously emphasized, interfacial dynamics of surfactant molecules at soap film interfaces are very subtle, so that the interface history linked to the initialization procedure may play a role in the film thickness and overall dynamics. Except for the downward flows in the Plateau borders, those sources of fluctuations have to be regarded as difficult to quantify with respect to thickness profile behaviors. However, the averaged curves presented in Figure 2.10 contain those fluctuation sources, so that the statistic treatment we made about the thickness profiles should be considered as a relevant characterization of our films, whatever the uncontrolled phenomena implied. Moreover, it avoids in-situ additional measurements which could reveal difficult to adapt to our initial setup (especially PIV devices).

2.4.2 Quantitative characterization of thickness profiles

The thickness profiles presented in Figure 2.10 almost have the same shape, as if an increase in Q led to a shift towards higher thickness values. Figure 2.10 plotted in logarithmic scale shows that the thickness profiles present a linear dependency on H , which is the sign of a scaling behavior, expressed by a power law. We then chose to fit the averaged thickness profiles with a power law in order to obtain a continuous expression for $e(H, Q)$ to be used in the theoretical modelings and numerical investigations of our experiments (see next chapters). We chose to express the thickness versus H as :

$$e(H, Q) = a(Q)H^{-\beta(Q)} + e_0, \quad (2.7)$$

with a the scaling pre-factor, β the scaling exponent and e_0 an offset on the thickness. The scaling exponent β versus Q seems not to depend on Q , at least in the Q range and for the surfactant considered here (see Fig. 2.11, top). On the contrary, a presents an overall increase with Q illustrated on the bottom curve of Figure 2.11. Those behaviors are compatible with the general shape of the thickness profiles. As discussed in the previous section, the behaviors of those two quantities has to be regarded as resulting from a combination of various surfactant phenomena such as interfaces elasticity, dynamical equilibrium of surfactant molecules at the film interfaces, surface viscosity... Even if a and β cannot be expressed as functions of those quantities, their partial knowledge as functions of Q are sufficient to characterize the behavior of the thickness profiles versus H and Q in our maintained soap films. Those parameters will be widely used in the next chapters, since they are implied in almost every model used to describe our experiments. Note that the same kind of behaviors (i.e. unchanged scaling exponent and variable scaling factor) have been observed by Berg and collaborators in temporal investigations of freely suspended soap film drainages [78].

The thickness profiles described by Eq.(2.7) can be used in order to estimate the magnitude of the thickness gradient in our fed soap films. Considering an analogous situation to the one used to estimate the thickness gradient from interference profiles, on gets that $\delta e/\delta H \sim 10^{-4}$, which is in rather good agreement with the magnitude obtained by optical methods.

We have to mention that the quantitative characterization of the thickness profiles described by Eq.(2.7) is only valid in the central region of the film, i.e. for $H \in [1.5 : 10]$ cm. Due to the boundary conditions imposed to the film by the frame, another expression should be used to link the thickness of the films in the vicinity of the frame to the thickness of the central region.

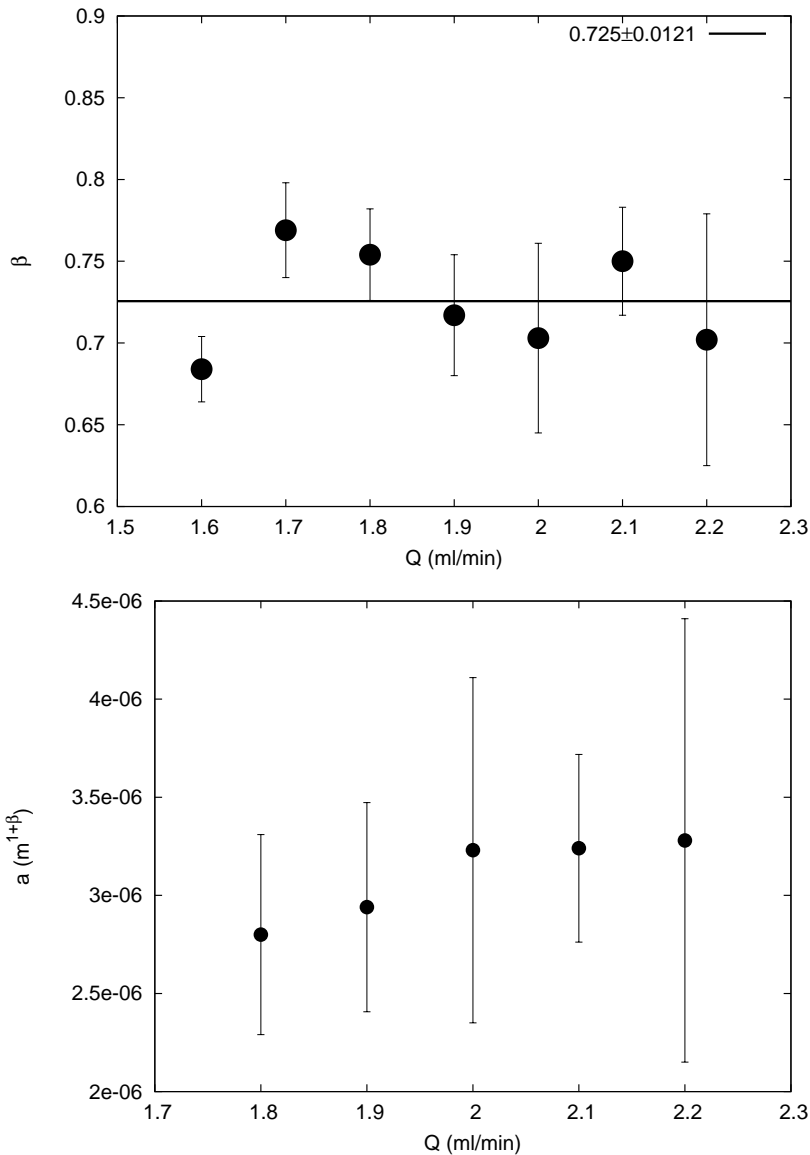


Figure 2.11: Top : Scaling exponent β (Eq.(2.7)) versus injected flow rate Q . The solid line represents a fit thanks to a constant value. Bottom : Scaling prefactor a (Eq.(2.7)) versus the injected flow rate Q .

2.4.3 Velocity profiles

To conclude this chapter, we underline that it is possible to estimate the velocity profile linked to the global downward flow in our maintained soap films from corresponding thickness profile measurements. We here consider that the injected flow rate is equal to Q in first approximation (the losses in the Plateau borders

are neglected). To do so, we consider the mass conservation. As the feeding flux is fixed, the corresponding flow must be recovered everywhere in the film. The mass conservation equation can be written as :

$$Q = e(H, Q)v(H, Q)L, \quad (2.8)$$

where $v(H, Q)$ is the vertical velocity profile. Since $e(H, Q)$ is known from infrared absorption measurements, it is possible to express $v(H, Q)$ from Eq.(2.8) and so to estimate the velocity profiles in our films. Figure 2.12 illustrates the velocity profiles for Q ranging from 1.6 to 2.2 ml/min. One sees that the typical downward velocity is $10^{-3} - 10^{-2}$ m/s. Those profiles evidence that the velocity increases as H increases, and so as $e(H, Q)$ decreases. This is consistent with the mass conservation. One also sees that for Q values larger than 1.8 ml/min, the velocity profiles linked to different Q do not exhibit large magnitude variations. As it could be expected from the similarities between the thickness profiles (see Fig. 2.10), the velocity profiles exhibit general shapes which are quite similar for the different Q values considered here.

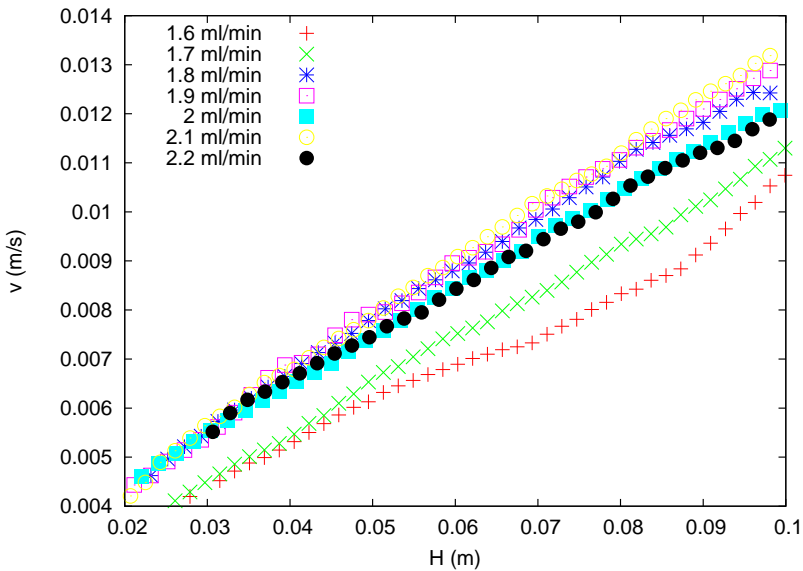


Figure 2.12: Velocity profiles v in maintained soap films versus the vertical coordinate H .

Those velocity profiles present an opposite trend than the free falling liquid curtains or soap films [46,69,70]. The downward velocity in our films indeed increases with H . This observation confirms the fact that our films are in a drainage state, and that their behaviors are controlled by interfacial phenomena rather than by

gravity and inertia. The Reynolds number linked to the downward flow can be estimated as [2] :

$$\text{Re} = \frac{\rho v l}{\eta}, \quad (2.9)$$

where η is the dynamic viscosity of the fluid and l the typical scale linked to the flow. Considering that $l \sim e \sim 10^{-5}$ m, we obtain $\text{Re} \sim 10^{-1}$. This estimation confirms that the global downward flow in soap films can be considered as laminar. Those velocity measurements have been used in several modelings presented in the next chapters. A more accurate way to determine those profiles, and to eventually corroborate the results presented here would be to realize PIV measurements.

2.5 Conclusion

In this Chapter, we have shown that it is possible to build maintained soap films by applying a wisely chosen feeding flow, created from the setup presented in the previous sections. An infrared method allowed us to obtain a quantitative characterization of our maintained soap films. Those thickness measurements allowed to conclude that the thickness profiles of our films behave as power laws of the vertical coordinate. Both the scaling pre-factors and the exponent are seen to depend on the injected flow Q . Eventually, we showed that the mass conservation coupled with thickness measurements gives an estimation of the velocity profiles of the downward flow imposed to the films.

Chapter 3

Surface tension profiles in soap films

Air/water interfaces are characterized by a tension force present everywhere, the so-called surface tension. Adding surfactant molecules at the interface leads to a decrease of the surface tension, and therefore, an increase of the surface pressure. Considering the chemical equilibrium that should exist at the interface, one sees that subtle interactions may take place between the bulk and the interface, depending on both the bulk concentration and the nature of the surfactant molecules. For instance, micelles may adsorb and disintegrate at the interface, leading to extra amounts of surfactant molecules. These effects have been proposed to be responsible for consequent variations in the elasticity of the interface, and therefore affecting the soap film drainage dynamics [19].

This chapter concerns the measurements of the surface tension within soap films. We present the technique we developed for achieving this measurement and show that rather simple mechanical arguments can be proposed for linking the surface tension profiles and the corresponding thickness profiles. This model is based on the pioneer Gibbs idea (1878, [83, 84]) and is confronted with the experimental data.

3.1 Mechanical equilibrium in vertical soap films

Let a vertical soap film be defined by an area $L \times L$ at a given time. Figure 3.1 is a scheme of a transverse cut of such a film. Any film portion located beneath any H value is characterized by its weight. Simple logics imposes that this weight must be counterbalanced by a sustaining force in order to justify the stability of the soap film. In 1878, Gibbs proposed that this role is played by the surface tension forces at the film interfaces [83, 84]. Since the weight of the film beneath a given position H increases with H , there must be a surface tension gradient

along the film vertical. In other words, the surface tension is expected to increase with H . This idea was quite innovative because chemical equilibria of surfactant at liquid interfaces were not yet well grasped at that time. However, they were pointed out as (eventually) being responsible for surface tension variations with H .

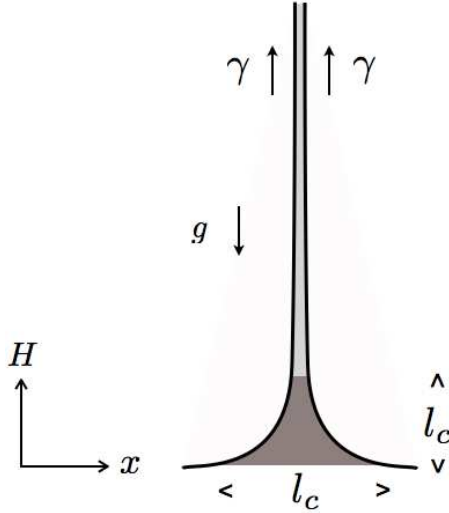


Figure 3.1: Scheme of a transversal cut for a vertical soap film (not to scale). The light grey part is the area in which optical interference fringes develop. The dark grey area represents the bottom meniscus linking the film to the bottom edge of the frame. The H coordinate corresponds to the vertical coordinate in the film, while x corresponds to the transverse coordinate (i.e. normal to the film interfaces).

The transverse cut schematized in Figure 3.1 supposes that the film splits by thinking into two parts : (i) the “usual” thin part where interference fringes are observe and (ii) the meniscus, linking the film to the bottom edge of the frame. Our observations revealed that the bottom meniscus is always thicker than the lateral and the top menisci. This suggests that it should be included in the total weight to be balanced by the surface tension forces. This weight is then a sum of the weight of the meniscus, plus the weight of the film portion lying under H . The mechanical equilibrium then writes :

$$2\gamma(H, Q) L = W_{\text{meniscus}} + W_{\text{film}}(H, Q), \quad (3.1)$$

with clear notations. It is possible to compute both W_{meniscus} and $W_{\text{film}}(H, Q)$ knowing the density and volumes of both parts. The meniscus height and width can reasonably be considered as equal to the capillary length linked to the surfac-

tant. The surface tension of the meniscus interfaces can be considered as equal to the surface tension of the solution and constant everywhere in the meniscus, in a first approximation. The meniscus weight then writes :

$$W_{\text{meniscus}} = \rho l_c^2 L g = \gamma_0 L, \quad (3.2)$$

where l_c is the capillary length defined by Eq.(1.5), and γ_0 the surface tension of the solution, which is equal to its surface tension at the CMC in the present case (see Chapters 1 and 2 for the description of the solution).

Knowing the thickness profiles, it is then possible to express the weight of the film lying below H as :

$$W_{\text{film}}(H, Q) = \rho g L \int_0^H e(h, Q) dh. \quad (3.3)$$

Since all the quantities involved in W_{meniscus} and $W_{\text{film}}(H, Q)$ are known, recalling Eq.(3.1) gives an expression for $\gamma(H, Q)$:

$$\gamma(H, Q) = \frac{\gamma_0}{2} + \frac{\rho g a(Q)}{2(1-\beta)} H^{1-\beta}. \quad (3.4)$$

A few comments can be made about the soap film phenomenology and Eq.(3.4). Both the thickness profile (see Fig. 2.10) and the fringe pattern (see Fig. 2.1) suggest that the film thickness decreases with H , since the interference fringes become more spaced as H increases. However, the total weight of the film is supposed to increase with H . Thus, the surface tension should express as a rising and saturating function of H , what is actually refound in Eq.(3.4). Figure 2.10 also suggests that the thickness of the film increases with Q for every H value. W_{film} is thus supposed to increase as well, what is rightly modeled by $\gamma(H, Q)$. Introducing orders of magnitude in Eq.(3.4) brings that $\gamma(H, Q) \sim 10$ mN/m for $H \sim 10^{-2}$ m, in agreement with the usual surface tension values.

Since all the quantities implied in Eq.(3.4) are known, $\gamma(H, Q)$ can be plotted versus H , as shown in Figure 3.2. We underlined in Chapter 2 that the averaged thickness profiles can be distinguished with respect to the Q values through the value of the prefactor a used to fit those profiles (see Figs.2.10 and 2.11 and Eq.(2.7)). Since we did not build any model for a versus Q , we chose to consider a statistical approach for the a values to be included in Eq.(3.4). This approach is built considering that the dispersion exhibited by the single thickness profiles measurements should somehow be recovered in the surface tension profile, which is consistent with the dependence of $\gamma(H, Q)$ on $e(H, Q)$. The solid line in Figure 3.2 corresponds to Eq.(3.2) plotted for the averaged value of a , named $\langle a \rangle$. This curve represents the averaged behavior of γ versus H linked to our soap films. In order to obtain an estimation of the dispersion of $\gamma(H, Q)$ around this average trend, it is necessary to consider the dispersion σ_a of a around $\langle a \rangle$. The dashed

lines in Figure 3.2 are Eq.(3.4) plotted for $\langle a \rangle + \sigma_a$ and $\langle a \rangle - \sigma_a$, illustrating the dispersion of γ generated by the dispersion of a with Q . The curves presented in Figure 3.2 represent the expression of the dynamical equilibrium of vertical soap films as proposed by Gibbs, in the particular case of our fed films. In order to check the validity of $\gamma(H, Q)$, it is necessary to develop a technique for probing the surface tension profiles in our films, and then to compare the corresponding results to our predictions.

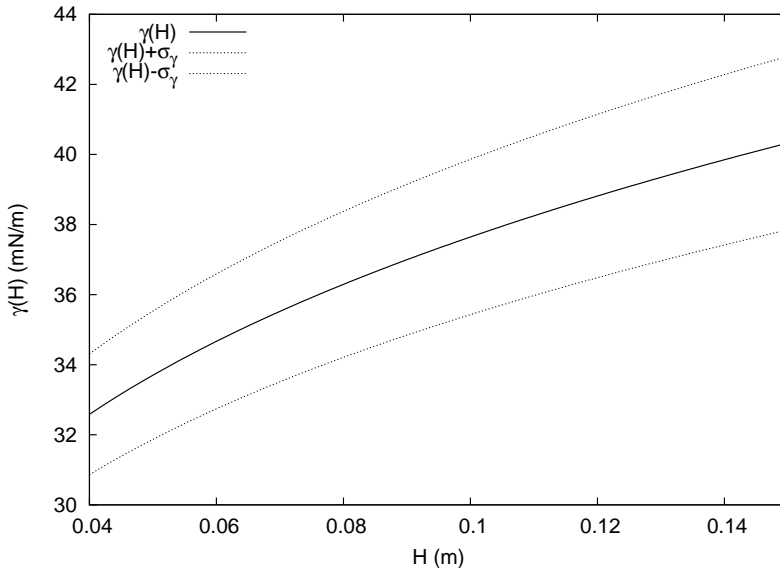


Figure 3.2: Surface tension profile $\gamma(H, Q)$ defined by Eq.(3.4) plotted versus H . The solid line corresponds to the profile obtained by considering the mean a value $\langle a \rangle$. The dashed lines represents the dispersion of $\gamma(H, Q)$ obtained by considering the dispersion of a around $\langle a \rangle$.

Several methods exist for measuring surface tension (see Chapter 1). However, those methods are designed for the purpose of setups such as Langmuir tanks, or are based on the behaviors of droplets in the presence of external constraints such as gravity, air friction... Although very relevant in their respective purposes, those methods are unadapted to vertical soap films. For instance, introducing devices such as Wilhelmy plates in the film would a strong local curvature in the film due to the wettability of the plate. We wished to avoid those effects because of their perturbative action on the film. For the purpose of this measurement, we need : (i) to design a probe which can easily be introduced in the film without generating unwanted perturbative effects, (ii) this probe must be reactive to the surface tension values exhibited by our film interfaces, (iii) the probe must be as

linear as possible, and easy to calibrate thanks to well established measurements or theories. It has been shown in recent studies that soft elastic objects can encounter considerable deformations under the action of capillary constraints [85–100]. Those effects can then be envisaged in order to design a probe. Their building and characterizations are presented in the next sections.

3.2 Surface tension probe

3.2.1 Elasticity

Elasticity refers to the ability of any material to exhibit reversible deformations under the application of external constraints [101,102]. Two classes deformations can be defined, following both the nature of the object to be deformed and the constraints applied on it.

Let an elastic sheet be characterized by a thickness h_0 , a length L_0 and a Young modulus E . This sheet is submitted to a constant constraint named σ . The situation is schematized in Figure 3.3. If the constraint is a traction, the sheet stretches in the direction of the constraint and contracts in the transverse directions. These deformations are formalized thanks to the Poisson coefficient of the object, defined as [101,102] :

$$\nu = \frac{\text{transverse unitary contraction}}{\text{axial unitary length increase}} = \frac{(h_0 - h)/h_0}{(L_0 - L)/L_0}, \quad (3.5)$$

with h and L are the thickness and length of the stretched sheet. The Poisson coefficient ν ranges within [-1: 0.5] and is usually experimentally determined as close to 0.3. The stretching energy can be evaluated by order of magnitude calculation as being $\varepsilon_s \sim Eh_0L_0(L - L_0)$. This calculation shows that the thicker and the longer the sheet is, the harder it is to induce stretching.

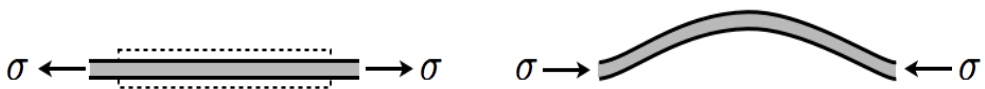


Figure 3.3: Euler's test for a thin elastic sheet of thickness h_0 and Young modulus E . Left : deformation due to a traction constraint. Right : deformation due to a pressure constraint.

If the direction of the constraint is changed, a compression is applied to the sheet and the dynamics becomes a little less obvious. The previous analysis in terms of stretching remains valid in the sense that compression may lead to an increase in h_0 , followed by a decrease in L_0 . This case is simply the symmetric to the traction

constraint. However, under a certain thickness value, at a constant σ value, the sheet exhibits buckling, as presented in Figure 3.3. The energy linked to the bending of the sheet is $\varepsilon_b \sim EI_0(h/L^2)^2L$ where I_0 is the quadratic momentum linked to the sheet, and expressed as $hL^3/12$ [101, 102]. The bending energy is then proportional to Eh^3 since the stretching energy is proportional to Eh . Thus, if the thickness of the sheet is weak enough, a bending will be observed rather than a stretching under the appliance of a pressure constraint. This simple experiment is the so-called Euler's thin sheet test and is used to illustrate the fact that curvature may be the preferred way for a material to deform when submitted to an external constraint. The quantity EI_0 is called the bending stiffness of the object and represents its resistance to an increase of its curvature radius under the action of an external constraint.

3.2.2 Elastic polymer

The term "Elastic material" can refer to numerous kinds of materials (plastic, rubber, glass, concrete, iron...) depending on both the geometrical characteristics of the considered object and the constraint magnitude applied on it. Following their Young modulus values, they can be considered as soft or hard materials. Rubber-like materials are called soft, because it is usually very easy to modify their shapes (most of the time, they can deform under their own weight). Their Young modulus is of the order of a few kPa to a few MPa. Solid materials such as glass or iron are called hard, because consequent constraints are needed in order to deform them. Their Young modulus can reach several GPa.

All the elastic objects used in our experiments are made of vinylpolixilosane. This initially liquid polymer can be reticulated into soft solid elastic objects. The reticulation is realized by adding a liquid catalyzer to the rough polymer. After mixing, the catalyze takes a few minutes, during which the mixture remains liquid. By machining designed molds such as imaged in Figure 3.5, it is possible to create soft elastic objects with the wanted geometrical characteristic. As an anecdote, one can note that this polymer is usually used by dentists in order to obtain toothprints. Those polymers are commercially sold in bottles such as the one pictured in Figure 3.4.

The different colors given to the rough polymers correspond to different values of the Young modulus of the final objects. Those moduli are expressed in Shore units, and are used by dentists rather as an indicative than quantitative information. We will see in the next sections that precise knowledge of these Young moduli is needed in order to obtain accurate descriptions for the dynamical behaviors of the related objects. Let us mention that the different polymers can be classified



Figure 3.4: Pictures of the polymers used to make elastic objects (©Zhermack Elite Double). The colored bottles is the polymer, and the white associated bottle is the catalyzer. Each color correspond to a different value of the Young modulus of the final product.

in function of their color as follows, from the softer to the harder : pink, purple, turquoise and green. The next section is devoted to the description of the method we designed in order to quantitatively obtain the Young moduli of these different polymers.

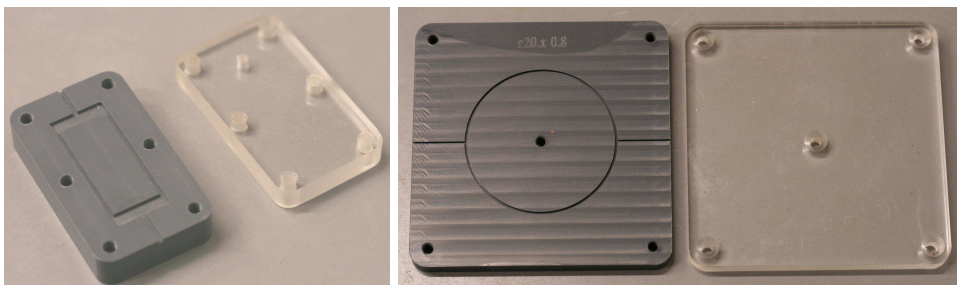


Figure 3.5: Examples of molds used to build elastic objects from the liquid polymer. Left : an example of mold used to build rectangles. Right : an example of mold used to build rings (see next sections for details).

3.2.3 Elasto-capillary and elasto-gravitary lengths

In an attempt of characterizing the Young modulus of a solid material, classic traction tests are usually considered. However, mechanical constraints can be ap-

plied to materials by several other ways. A simple example is given by the case of a soft elastic ring suspended to a needle and deforming under its own weight, as schematized in Figure 3.6. Under the action of gravity, the ring adopts a shape similar to an egg. Observations of different rings made out of the same material, with the same section but different radii revealed that the smaller rings are not deformed. This suggests the existence of a critical radius under which gravity constraints are not strong enough to deform the rings.

For modeling this phenomenon, let us consider a ring characterized by a circular section $S = \pi r^2$ and a radius R hanging on a needle. If R is large enough, the ring deforms under its own weight, as schematized in Figure 3.6. The potential gravitational energy lost by the ring can be estimated as $\varepsilon_g \sim \rho g S R^2$ if one considers that the order of magnitude of the deformation is R . The corresponding bending energy can be estimated as $\varepsilon_b \sim EI_0/R$ [101, 102]. Making the ratio of those energies brings an expression for the typical radius beyond which gravity becomes preponderant. This length scale is called the elasto-gravitary length and reads :

$$L_g \sim \left(\frac{EI_0}{\rho g S} \right)^{\frac{1}{3}}. \quad (3.6)$$

This length is the elastic analogous to the capillary length presented in Chapter 1, and represents an estimation of the size (radius in the present case) beyond which the rings deform under their own weight.

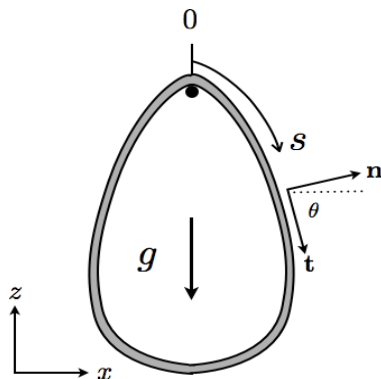


Figure 3.6: Scheme of a elastic ring hanging on a needle and deforming under its own weight.

Beyond these simple order of magnitude calculations, it is possible to obtain a formal description of such elastic objects submitted to an external constraint. This

is done by adapting the usual mechanic equations to continuous media (see [101, 102] for details). The forces and torques equilibria for elastic objects respectively read :

$$\left\{ \begin{array}{l} \frac{d\mathbf{F}}{ds} = -\mathbf{K} \end{array} \right. \quad (3.7)$$

$$\left\{ \begin{array}{l} EI_0 \frac{d^2\theta}{ds^2} = (\mathbf{F} \times \mathbf{t}) \cdot \mathbf{e}_y, \end{array} \right. \quad (3.8)$$

where s is the curved abscissa linked to the system, \mathbf{F} represents the internal forces within the object, \mathbf{K} is the linear density of the external constraints applied to the object, θ the angle linked to s , \mathbf{t} the tangential vector to the curve described by (s, θ) and \mathbf{e}_y the unitary vector normal to the plane in which the deformations occurs (see Figs. 3.6, 3.12, 3.14 for illustrative examples). If the external constraint is known, the system formed by Eqs.(3.7) and (3.8) relates the shape adopted by the object to the constraint considering its geometrical and physical characteristics. Those equations are widely used in order to reproduce the experimental behaviors of constrained elastic objects. Assorted to cleverly chosen boundary conditions, they revealed very relevant in various situations [85,92,105]. Here, the shape adopted by the soft pending ring can be numerically predicted by considering the system formed by Eqs.(3.7) and (3.8) with $\theta(s = 0) = 0$, $\theta(s = l/2) = -\pi$, $d\theta/ds(s = 0) = d\theta/ds(s = l/2)$, to ensure the curvature continuity in those points. The conditions $x(s = 0) = x(s = l/2) = 0$ ensure the vertical symmetry of the ring. Note that this latter condition is equivalent to impose a condition on the internal force in $s = 0$ and $s = l/2$ so that the extremities remain at the same abscissa. The external density force reads $\mathbf{K} = \rho_s S \mathbf{g} = -\rho_s S g \mathbf{e}_z$ if ρ_s represents the density of the polymer and S the section of the ring. Due to the symmetry of the system, only half the ring can be considered. The so-written system can then be made dimensionless. In the framework linked to the lab, the system formed by Eqs.(3.7) and (3.8) writes :

$$\left\{ \begin{array}{l} \frac{dF_x}{ds} = 0 \end{array} \right. \quad (3.9)$$

$$\left\{ \begin{array}{l} \frac{dF_z}{ds} = \rho_s S g \end{array} \right. \quad (3.10)$$

$$\left\{ \begin{array}{l} EI_0 \frac{d^2\theta}{ds^2} = F_x \sin(\theta) - F_z \cos(\theta). \end{array} \right. \quad (3.11)$$

The curved abscissa s can be written as $s = \hat{s}l$ with \hat{s} being the non dimensional abscissa. The system can be re-written as :

$$\left\{ \begin{array}{l} \frac{dF_x}{d\hat{s}} = 0 \end{array} \right. \quad (3.12)$$

$$\left\{ \begin{array}{l} \frac{dF_z}{d\hat{s}} = \rho_s Sgl \end{array} \right. \quad (3.13)$$

$$\left\{ \begin{array}{l} \frac{EI_0}{l^2} \frac{d^2\theta}{d\hat{s}^2} = F_x \sin(\theta) - F_z \cos(\theta). \end{array} \right. \quad (3.14)$$

The quantity $F = \rho_s Sgl$ has the dimension of a force, and represents the typical force applied to the ring by gravity. Dividing each members of each equation of the system by F allows to get a fully non dimensional system, which reads :

$$\left\{ \begin{array}{l} \frac{d\hat{F}_x}{d\hat{s}} = 0 \end{array} \right. \quad (3.15)$$

$$\left\{ \begin{array}{l} \frac{d\hat{F}_z}{d\hat{s}} = 1 \end{array} \right. \quad (3.16)$$

$$\left\{ \begin{array}{l} \frac{EI_0}{\rho_s Sgl^3} \frac{d^2\theta}{d\hat{s}^2} = \hat{F}_x \sin(\theta) - \hat{F}_z \cos(\theta), \end{array} \right. \quad (3.17)$$

where \hat{F}_x and \hat{F}_z are the non-dimensional internal forces acting on the ring and expressed in the lab framework. The system formed by Eqs.(3.15), (3.16) and (3.17) can then be considered for numerical computation, with the non-dimensional quantity $EI_0/\rho_s Sgl^3$ being the only control parameter of the system. This latter can be considered over a wide range (several decades if wanted) during the numerical computation of the problem. The physical interpretations about the physical quantities implied in the problem can then be determined by comparing the non-dimensional values of this parameter with its expression in terms of those quantities. It is interesting to note that the making the original system dimensionless leads to the natural appearance of $EI_0/\rho_s Sgl^3$ as being the unique control parameter of the system. This quantity is nothing but the dimensionless elasto-gravitary length described by Eq.(3.6). This matching ensures that the formal description of any elastic object thanks to Eqs.(3.7) and (3.8) shares the same physical background than the simple order of magnitude description of the problem. The numerical solving of the dimensionless equations can then be achieved for several purposes, i.e. obtaining the numerical shape of the deformed ring or determining a critical physical parameter beyond which the bending occurs.

Beyond the reproduction of the shapes adopted by the rings, the numerical results can be used in order to determine their Young moduli. In fact, it is possible to obtain the theoretical evolution of the perimeter of the ring made dimensionless by the elasto-gravitary length as a function of the aspect ratio of the hanging ring (see Fig. 3.7). Images of the hanging rings can then be used in order to determine

the Young modulus of the corresponding elastic material. Table 3.1 presents a comparison of Young modulus measurements by traditional traction tests and obtained from the precited method for different elastic materials, showing that our hanging ring method can be considered as a simple and relevant way to obtain reliable Young Modulus measurements.

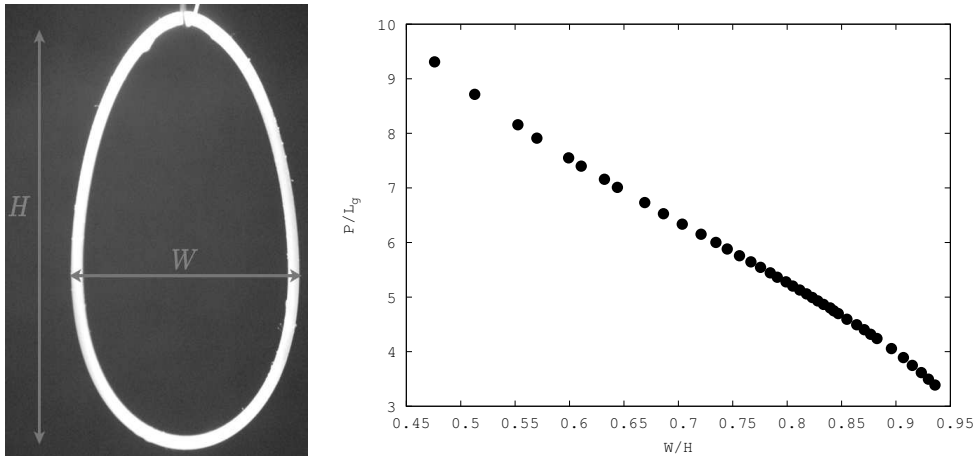


Figure 3.7: Hanging ring method for Young modulus measurement. Left : picture of a hanging ring as used for measurements. Right : calibration curve obtained from solving of adapted elasticity equations.

The shore units given by the manufacturer of the polymers can be converted to conventional units (i.e. MPa) by the following formula [103,104] :

$$E = \frac{0.0981(56 + 7.623365 Sh)}{0.137505(254 - 2.54 Sh)}, \quad (3.18)$$

where Sh is the hardness of the material expressed in shore units. The converted values for the different polymers are presented in Table 3.1. Using Eq.(3.18) reveals that the orders of magnitude of the Young modulus given by the manufacturer matches with the ones obtained by traction tests and the hanging ring method. However, the agreement between the values obtained by traction tests and the hanging ring method is better than the agreement with the manufacturer values. Several arguments can be developed to justify these differences. First, it can be shown by in-lab tests that the proportion of polymer and catalyzer which are mixed slightly influence the hardness of the final object. For example, mixing 40% of polymer with 60% of catalyzer leads to a final object which presence a smaller hardness than an object built from a 50-50 mixture. Since this difference can be evidenced by simply applying a pulling on the object by hand, the

proportion of the mixing must be regarded as a very influent parameter with respect to the final Young modulus value. A second parameter which influences the Young modulus is the age of the object. In fact, observation have revealed that the polymer tend to harden with time. The experimental condition which are imposed to the object may also tend to harden them. For example, wetting the object has proved to increase the time dependence of the hardening. In the end, these sources of variation for the Young modulus of these polymers impose that the experimenter should always dispose of dedicated Young modulus measurement methods in order to ensure of the value of the Young modulus to be used in theoretical descriptions of their experiments.

	pink	purple	turquoise	light green
manufacturer	357kPa	595 kPa	805 kPa	1.239 MPa
Traction	270 kPa	681 kPa	789 kPa	1.2 MPa
Hanging ring	300 kPa	666 kPa	774 kPa	1.332 MPa

Table 3.1: Young Modulus of the different elastic materials obtained from the manufacturer, classic traction tests and our hanging ring method.

Instead of gravity, capillary constraints can also be used to generate bending of elastic objects [85–100]. Imagine the previous soft elastic ring placed on a air/water interface. If the outer or inner interface regarded to the ring is loaded with surfactant molecules, the ring is then submitted to the corresponding surface tension difference $\Delta\gamma = \gamma_{\text{in}} - \gamma_{\text{out}}$. From the surface pressure point of view, the ring is submitted to a surface pressure difference between the outside and the inside. From the definition of the surface pressure as defined by Eq.(1.9), one sees that the surface pressure difference $\Delta\Pi$ reduces to the surface tension difference $\Delta\gamma$. Thus, $\Delta\gamma$ can either be used to refer to surface tension or surface pressure effects. Two cases can be evidenced with this system : (i) if the surfactant is added inside the ring, it may expand under the action of surface pressure, depending on both its geometrical and physical properties (Young modulus and section). Although interesting, this case is not discussed here. (ii) if the outer interface is loaded keeping the inner part free, the ring may start to deflate under the action of the surface pressure, going from a circular to a peanut shape, which is pictured in Figure 3.8.

The energy balance responsible for the deformation can be estimated as $\varepsilon_b \sim EI_0/R$ for the bending and $\varepsilon_\gamma \sim \Delta\gamma R^2$ for the gain of interfacial energy. Equaling both brings an expression for the radius beyond which the ring starts to deform under the action of $\Delta\gamma$. This elasto-capillary length reads :

$$L_\gamma \sim \left(\frac{EI_0}{\Delta\gamma} \right)^{\frac{1}{3}}. \quad (3.19)$$

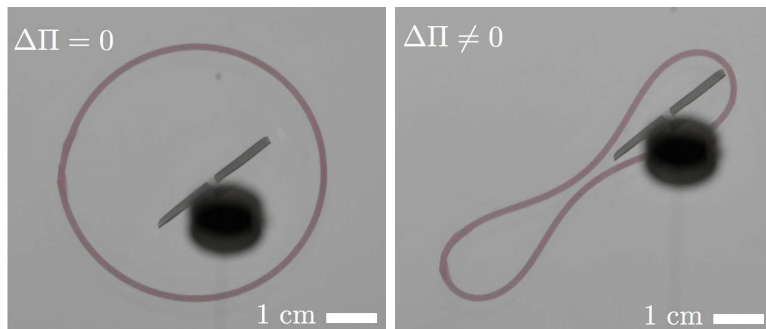


Figure 3.8: Shape adopted by a ring deposited at an air/water interface. Left : both interfaces are surfactant-free ($\Delta\gamma = 0$). Right : the outer interface is loaded by surfactant molecules ($\Delta\gamma \neq 0$).

This length characterizes many physical systems involving bending of elastic objects under the action of interfacial constraints [85–100].

This collapse of the ring can be easily evidenced at home in a sink, by dropping commercial soap on the outer interface to induce the full collapse of the ring (see Figure 3.10 for the largest $\Delta\gamma$). However, a langmuir tank (Figure 1.6) is needed for quantifying the evolution of the shape of the ring versus the surface tension constraint $\Delta\gamma$. The setup we used is schematized in Figure 3.9. The elastic objects are deposited on the water interface. Two Wilhelmy plate sensors are disposed on both the inner and outer interfaces, so that the surface tension difference $\Delta\gamma$ can be measured (see Fig. 3.9). The outer interface is then loaded with an insoluble surfactant (CF_{12}) so that an ideal surfactant (mono)layer is created. Since CF_{12} is insoluble, the interface our of the elastic object is the only one to be surfactant loaded. The surfactant layer is then compressed by reducing its area thanks to the barrier.

Taking pictures of the object while compressing it allows to follow the evolution of its shape versus the constraint, as measured by the Wilhelmy sensors. Figure 3.10 illustrates typical images taken by the camera during a ring compression. A further image analyses is then performed to characterize the shape of the ring. Figure 3.11 presents the area sustained by the ring versus $\Delta\gamma$. For each value of the Young modulus E different geometrical parameters of the rings have been tested. They are reported in the same color in the Figure 3.11 and present a similar shape but different values. Moreover, all curves exhibit a threshold in the $\Delta\gamma$ scale before a deformation is observed. This threshold depends on both E and I_0 . Intuitively, the threshold comes from the resistance of internal forces to local curvature variations (the ring behaves like an arch resisting to external pressure forces).

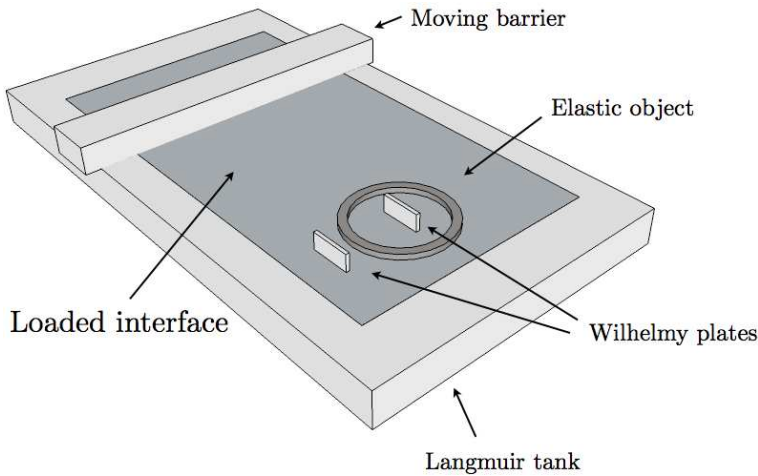


Figure 3.9: Langmuir tank used to apply controlled interfacial compressions on elastic objects. Two Wilhelmy plate sensors are used to determine $\Delta\gamma$ as the barrier is moved. Pictures of the object are taken by a camera (not represented here) in order to link the shape of the object to the corresponding constraint.

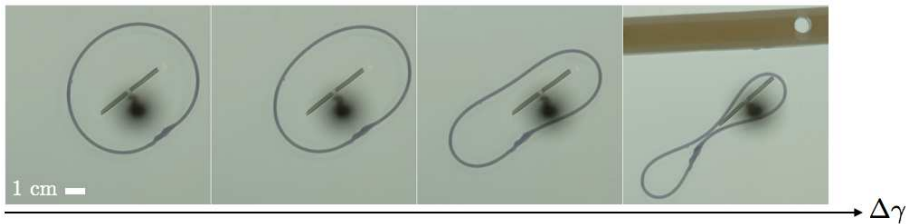


Figure 3.10: Successive pictures of the shape adopted by the rings with growing surface pressure constraint. As $\Delta\gamma$ increases, the ring goes from its natural circular shape to a peanut shape. One can see the moving barrier on the last picture. The inner Wilhelmy plate is also visible.

As previously done for the case of the hanging rings, the elasticity equations (Eqs.(3.7) and (3.8)) can be computed for modeling the shape of the interfacially constrained rings. For symmetry reasons, only a quarter of the object can be considered in the numerical resolution. Figure 3.12 illustrates the coordinates used for this formalization. The boundary conditions in this case write $\theta(s = 0) = 0$, $\theta(s = l/4) = -\pi/2$, $d\theta/ds(s = 0) = 0$ and $d\theta/ds(s = l/4) = 0$. These latter conditions ensure the continuity of the curvature at both extremities of the ring portion. In addition, boundary conditions on the internal forces must be added, being $F_x(s = 0) = 0$ and $F_z(s = l/4) = 0$ (no stretching in the ring), plus $F_z(s = 0) = 2r\Delta\gamma = F_x(s = l/4)$, in order to take into account the influence of

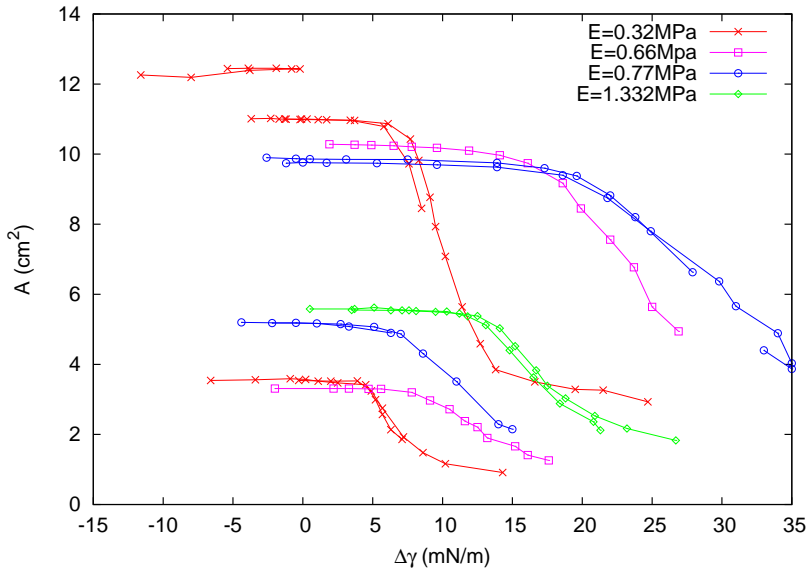


Figure 3.11: Area A sustained by the rings versus surface tension difference $\Delta\gamma$. For each Young modulus E , different ring geometries are presented.

the constraint on internal forces, with r being the radius linked to the ring section.

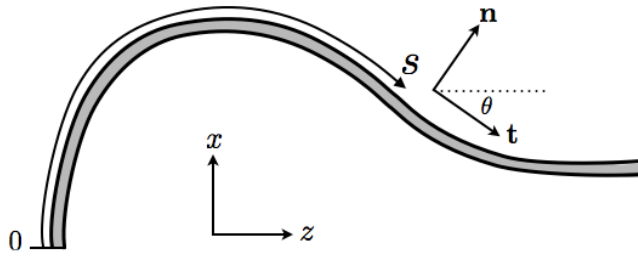


Figure 3.12: Schematics of the ring portion considered for theoretical formalization of compressed rings.

The external force density is the surface tension difference and reads $\mathbf{K} = \Delta\gamma\mathbf{n}$. The so-written equations can be made dimensionless, leading to the appearance of the elasto-capillary length as defined by Eq.(3.19) as a unique control parameter of the system. The procedure is similar to the one used for the case of the hanging ring. Figure 3.13 illustrates the evolution of the dimensionless area of the ring versus the dimensionless surface tension difference. The dimensionless area is defined as A/A_0 with A_0 being the area sustained by the non-deformed ring. The dimensionless constraint is defined as $\Delta\gamma/\Delta\gamma_0$ with $\Delta\gamma_0$ being the typical surface

tension difference leading to the ring collapse, obtained from the elasto-capillary length expression (Eq.(3.19)). These data reveal that the threshold value of surface tension difference to be reached for the rings to buckle is well reproduced. Once the threshold reached, the dimensionless area decreases rapidly, until self contact occurs. The change in the slope indicates that a new regime starts up when self contact occurs. Although interesting, we do not wish to discuss this case here. If interested, the lector can refer to the following reference [106] in order to get more information about extreme regimes for compressed rings. Figure 3.12 shows that the master curve got from dimensionless experimental data is faithfully reproduced by the proposed elasticity theory.

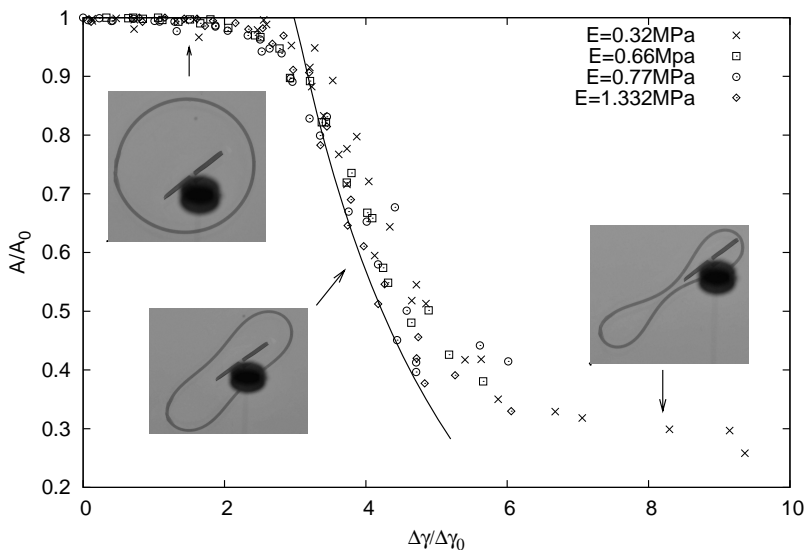


Figure 3.13: Dimensionless area A/A_0 versus dimensionless surface tension difference $\Delta\gamma/\Delta\gamma_0$ acting on the rings. Dots are experimental measurements, while the solid line represents the numerical modeling.

3.3 Surface tension probes in Langmuir tank

The previous paragraph have shown that an elastic ring can be used for probing a surface pressure difference. However, the annular probe present the disadvantage to require a critical surface tension difference in order to exhibit area/shape fluctuations (see Fig. 3.13). Moreover, the area decrease observed beyond that threshold is quite fast, what makes the probe sensitivity range rather narrow. It is then necessary build objects which present softer responses to surface tension constraints.

3.3.1 Rectangular probes : Langmuir tank calibration

Inspired by the case of thin bending objects like soft elastic sheets and rods, we designed rectangles such a presented in Figure 3.14. The lateral arms are characterized by a square section of dimension e , while the top and bottom edges are characterized by a surface $\zeta \times w$, with both ζ and w larger than e . The idea of such a design is that the quadratic momenta of the lateral and the transversal edges are significantly different from each other, the transversal being the largest. These geometrical characteristics are chosen so that only the lateral arms can bend under the appliance of surface pressure constraints. Moreover, since the quadratic momentum of the lateral arms is given by $e^4/12$, we chose to investigate rectangles characterized by thicknesses of 500 and 800 μm , in order to get insights on both influence of the Young modulus and the geometry. The length of the lateral arms l , the width of rectangles w and the height of the top and bottom edges ζ were fixed to 24, 12 and 3 mm, respectively. Those dimensions were chosen such that the rectangles experience considerable deformations when submitted to surface tension constraints. Indeed, the bending energy writes $\varepsilon_B \sim EI_0 \left(\frac{\delta}{l^2}\right)^2 l$. This latter will be opposed to the interfacial energy $\varepsilon_\gamma \sim \Delta\gamma \delta l$, where δ is the deflection of the lateral arms as presented in Figure 3.14. For $\Delta\gamma \sim 10^{-3}$ mN/m, the deflection obtained from comparison of both energies is evaluated as $\delta \sim 10^{-3}$ m, what can easily be seen with an optical camera.

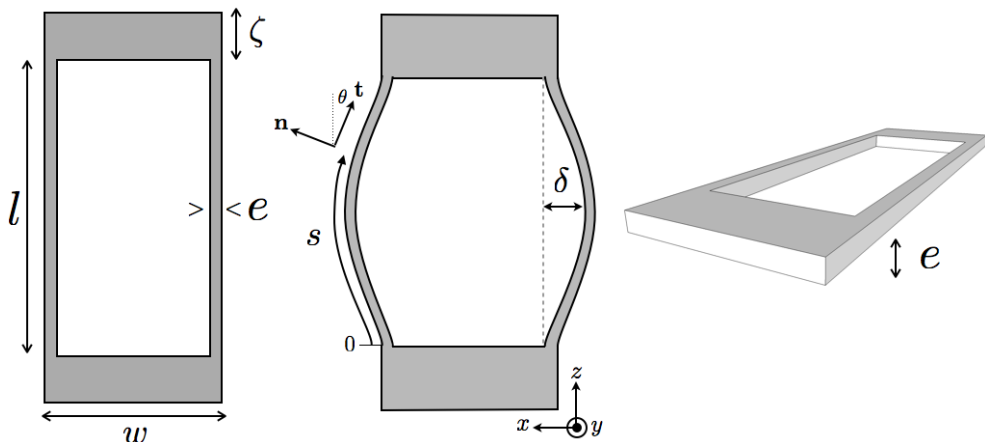


Figure 3.14: Schematics of the rectangles used as sensors for surface tension measurements. Left : undeformed case. middle : adopted shape under the action of a surface tension constraint, in the case where surface pressure is higher inside the rectangle than outside.

Two different surface pressure constraints can be applied to the rectangular probe. If the outer interface is loaded, then the rectangle deflates under the action of the surface pressure. This case has been studied in details in [99] for small deflections and in [106] for more extreme cases, and will not be discussed here. On the contrary, if the inner interface is loaded, the rectangle inflates as schematized in Figure 3.14 [106]. Before using these rectangles into soap films, we wished to test their sensitivity inside a Langmuir tank. From a practical point of view, we proceeded as follows : First, the inner interface of the rectangle was loaded with surfactant, so that it is fully inflated at the beginning of the experiment. Then, the outer interface was loaded in surfactant as well, in such a way that the outer surface tension remains higher than the inner one. This process ensures that the rectangle is still inflated before the compression of the outer interface is started. The Langmuir tank barrier is then progressively moved. This causes the decrease of the outer surface tension, so that the compression tends to bring the rectangle to its natural shape. In other words, along the experiment, the initially inflated rectangle is deflated by the compression. Figure 3.15 shows a few pictures of the rectangle during compression. Rather than considering the area sustained by the rectangle, we chose to focus on the deflection of the lateral arms δ , defined as the distance between the non-deformed and deformed lateral arm at mid height (see Fig. 3.14). The reason of this is that this quantity is easier to obtain from image analysis with a high accuracy than the area. Figure 3.16 presents the evolution of the deflection δ versus the surface tension constraint $\Delta\gamma$. In opposition to the case of the compressed rings, there is no constraint threshold to reach in order for the lateral arms to bend. This means that the sensitivity of the rectangles to weak surface tension constraints is higher than the sensitivity of the rings. In addition, δ varies rather smoothly in comparison to the dimensionless area for the rings. These two observations led us to consider the rectangle as being a good candidate for surface tension measurements.

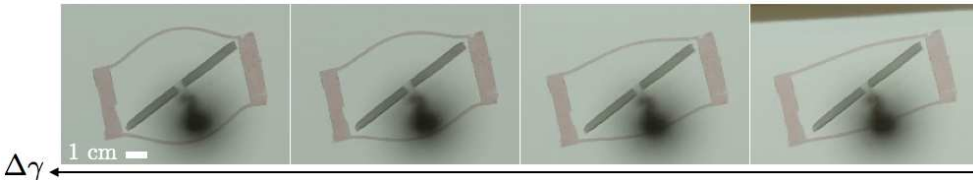


Figure 3.15: Successive images of a rectangle during a capillary compression. The inner interface has been loaded in surfactant, so that the external constraint tends to decrease the surface tension difference as the monolayer is compressed.

As previously explained for the the annular probe, the rectangle deflection can be modeled using the elasticity equations. The boundary conditions write $\theta(s =$

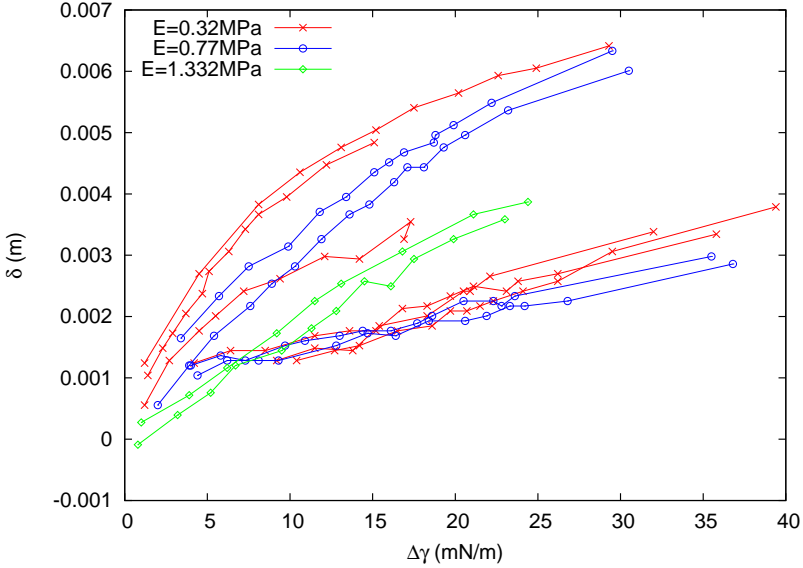


Figure 3.16: Deflection δ of the lateral arm versus surface tension difference $\Delta\gamma$. The different curves for a fixed Young modulus correspond to different I_0 values. In opposition to the case of the rings (see Fig. 3.13), the rectangles exhibit deformation even for weak constraints.

$0) = 0 = \theta(s = l/2)$ and $d\theta/ds(s = 0) = 0 = d\theta/ds(s = l/2)$, where only half the lateral arm is considered for symmetry reasons. The boundary conditions to be applied to the external forces are a little bit more subtle than for the rings. At the extremity of the half arm the internal force must satisfy $F_z(s = l/2) = 0$, expressing that no stretching is present at that position. Moreover, $F_x(s = l/2) = -e\Delta\gamma$ accounts for the influence of the surface forces on the arm. The internal force at the bottom of the arm writes $F_x(s = 0) = 0$, expressing the fact that the bottom extremity of the arm is attached to the bottom edge of the rectangle. Eventually, the condition $F_z(s = 0) = \Delta\gamma w/2$ models the pulling applied by the constraint on the bottom edge of the rectangle. This last condition is very important for the modeling of the deflections. Actually, if the surface pressure acts on the lateral arms, they bend, leading to a non null value of δ . Meanwhile, the same pressure also acts on the bottom edge, what tends to face the increase of δ . The external force density writes $\mathbf{K} = \Delta\gamma\mathbf{n}$, similarly to the annular case.

The so-written elasticity equations can then be made dimensionless, leading to the appearance of the elasto-capillary length as a unique control parameter. Those dimensionless equations can then be solved, leading to the solid curve in Figure 3.17. Once again, quantitative agreement is observed between experimental and numerical data. To end on this point, let us mention that the case of deflate

rectangles can also be both experimentally and theoretically considered, requiring specific adaptation of elasticity equations. Details about those investigations are presented in [99, 106].

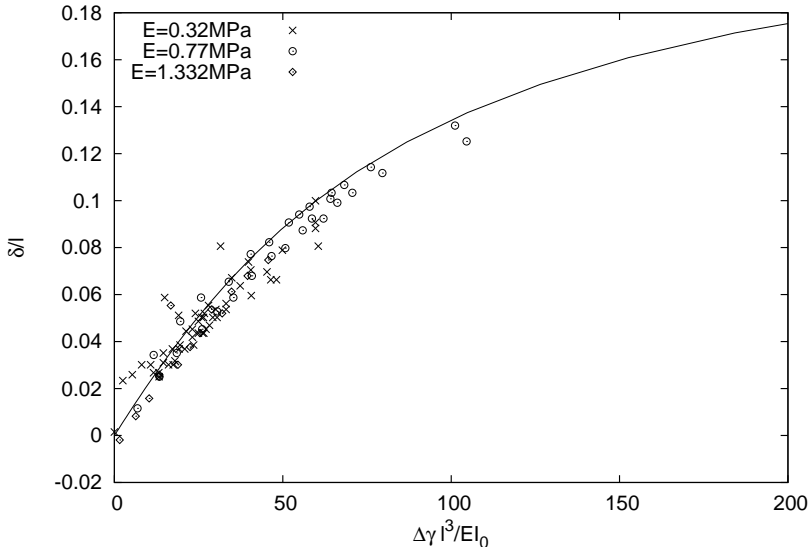


Figure 3.17: Dimensionless deflection versus dimensionless constraint for inflated rectangles. The solid line represents numerical data obtained from elasticity equations.

3.4 Rectangular probe : soap film configuration

Figure 3.18 illustrates two different states of the rectangular probe once plugged in a vertical soap film. If soap films are present both inside and outside the probe (left picture on Fig. 3.18), the shape adopted by the rectangle is the same as the one adopted when disposed on a pure water interface without any deflection ($\delta = 0$). If the inner film is burst, the rectangle suddenly adopts the shape presented on the central picture of Figure 3.18. This shape is reminiscent to the one adopted in the Langmuir tank for the case of a surface pressure difference constraining the rectangle. This picture attests from the ability of the surface tension in soap film to create deflections on the rectangles. The right picture of Figure 3.18 is the superposition of both cases, illustrating that our rectangles are prone to exhibit considerable deflections due to the surface tension constrains applied by the soap films.

Now, if the rectangle is vertically displaced in the film, it should then be possible to measure the deflection variation with the vertical coordinate H . However, the problem is that the constraint responsible for those deflections is unknown. It is then necessary to draw a link between the experimental deflections and the corresponding constraints.

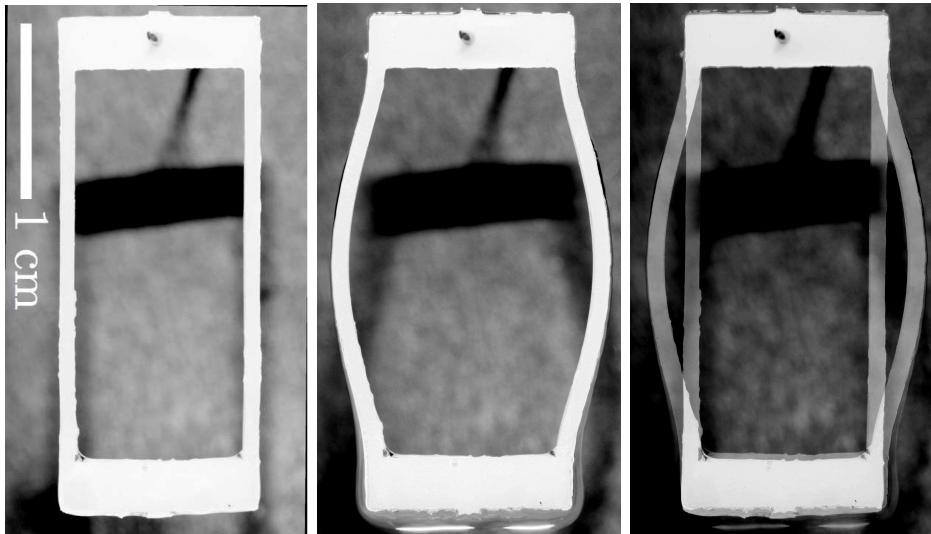


Figure 3.18: Rectangular probe plugged into vertical soap films. Left : soap films are present both inside and outside the rectangle. Middle : shape adopted by the rectangle right after the inner film is burst. Right : superposition of the two first pictures.

In order to obtain a theoretical calibration curve linking $\delta(H)$ to the corresponding $\gamma(H)$, the elasticity equations must be adapted to the case of rectangles plugged in vertical soap films. The boundary condition on θ and its derivative remains the same as the horizontal case, say $\theta(s = 0) = 0 = \theta(s = l/2)$ and $d\theta/ds(s = 0) = 0 = d\theta/ds(s = l/2)$. The first quantity to be modified is the density of the external force, which must be added the gravity. This density then writes :

$$\mathbf{K} = 2\gamma \mathbf{n} - \rho_s g S \mathbf{e}_x \quad (3.20)$$

if ρ_s is the polymer density and \mathbf{e}_x the unitary vector defined as $\mathbf{e}_x = -\mathbf{g}/g$. The prefactor 2 stands for the fact that both interfaces of the film are pulling on the rectangle. The internal forces at the end of the half arm writes $F_x(s = l/2) = 0$, expressing that no stretching occurs. Along z , we have $F_z(s = l/2) = 2\gamma e$. The boundary condition on the internal force at the bottom of the arm needs more modifications. As mentioned for the ring, the transverse internal force obeys $F_z(s = 0) = 0$. The condition on $F_x(s = 0)$ implies different forces. First,

the weight of the bottom arm, which can be expressed as $\rho_s g e \zeta w / 2$ must be taken into account. Second, the traction applied by the surface tension on this part, which can be expressed as γw , must also be considered. In addition, the weight of the meniscus linking the film to the bottom arm must be considered. This quantity can be expressed as $\rho_l g l_c^2 w / 2$ with ρ_l the density of the solution and $l_c = \sqrt{\gamma(H)/\rho g}$ the local capillary length. Eventually, the total boundary condition on the bottom edge of the rectangle must satisfy :

$$F_x(s=0) = \frac{w}{2} (\rho_s g e \zeta + 3\gamma). \quad (3.21)$$

Introducing dimensionless variables leads to the appearance of $EI_0/2\gamma l^3$ as a unique control parameter of the system. This parameter is the dimensionless elasto-capillary length expressed in the particular case of soap films.

We have to mention that another control parameter could appear, being $EI_0/\rho_s g e^2$, if the polymer density or the length or thickness of the lateral arms were subject to variations. This parameter is a constant in our case since we decided to fix the precited quantities.

All the physical and geometrical quantities involved in the problem are known, except γ . The system can then be numerically solved over a wide range of the control parameters. Figure 3.19 shows the results of the model for the evolution of the dimensionless deflection δ versus the dimensionless constraint.

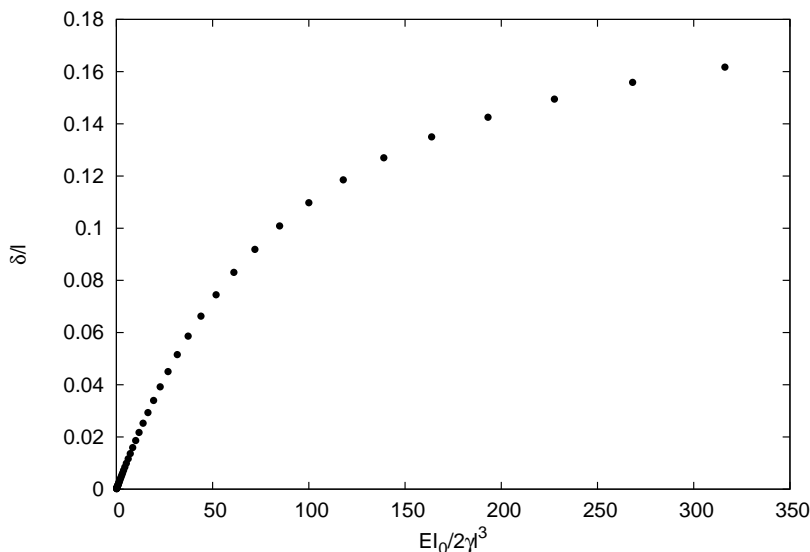


Figure 3.19: Theoretical dependency of dimensionless deflection δ versus dimensionless constraint.

Experimentally, we evaluated the evolution of δ with H from image analysis and used the curve presented in Figure 3.19 to obtain the corresponding value of γ . In so doing, we came up with a measurement of the vertical surface tension profiles in our soap films.

3.4.1 Deflection measurements

We have presented in section 3.4 that the inner film burst leads to consequent deflections of the rectangles plugged in the films (see Fig. 3.18). Those deflections are due to the constraints applied by the outer soap film on the rectangle. Since the surface tension is expected to vary with H , the deflection is supposed to vary with H as well. These are those fluctuations of δ with H which have to be used to determine the corresponding surface tension profiles via the calibration curve presented in Figure 3.19. The position H at which the surface tension measurement is considered corresponds to the center of mass of the rectangle once plugged in the film. It is instructive to estimate the different quantities involved in our experiments by order of magnitude calculations. Figure 3.20 shows that the traction applied by the surface tension γ on the lateral arms lead to a weak ascent l' of the bottom edge of the rectangle.

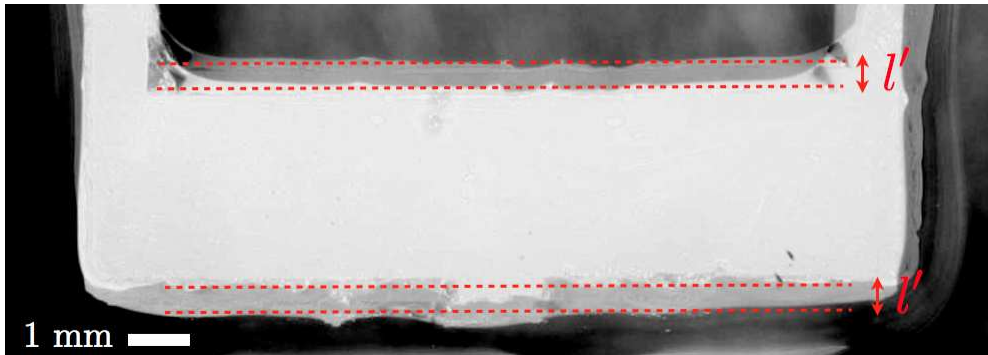


Figure 3.20: Zoom on the low part of the image showing the superposition of the rectangle inside and outside the soap film (Fig. 3.18). The dashed red line are guides for the eyes showing that when the rectangle is plugged in the film, its bottom edge tends to rise up as a consequence of the pulling applied by the surface tension of the lateral arms.

This ascent is followed by an increase of the potential energy of both the bottom edge and the meniscus linking the probe to the soap film. Those energies write $\rho_s V_s g l'$ and $\rho_L V_L g l'$, respectively. The related interfacial energy loss writes $\gamma w l'$ while the bending energy is expressed as $E I_0 \left(\frac{\delta}{l^2} \right) l$. Simple tests about trans-

verse tractions applied to soft rectangles in the air revealed that l' evolves quite smoothly with δ , i.e. consequent δ values are needed in order to obtain weak l' . From a geometrical point of view, it is then possible to express the ascent $l' \sim \delta^2/l$. The total energy balance for the rectangles in soap films is then given by :

$$2\gamma\delta l \sim \frac{\delta^2}{l} \left(\frac{EI_0}{l^2} + \gamma w + \rho_s V_s g + \rho_L V_L g \right). \quad (3.22)$$

This equation expresses the energy balance when the rectangle is plugged in the film with no soap film inside it.

The estimations made introducing order of magnitudes in this formula bring typical δ and γ values due to the soap film lack inside the rectangles. First experimental investigations for the behaviors of δ versus H revealed that very weak variations are observed between the bottom and top of the film. This implies that the l' fluctuations can be neglected, following their weakness and the geometrical expression of l' as a function of δ . The weakness of the δ fluctuations implies that the potential and interfacial energies involved in Eq.(3.22) only present very weak variations between the top and the bottom of the film. It is then possible to simplify Eq.(3.22) by considering the only term which does not depend on l' , namely the bending energy. After simplification, the energy balance linked to both fluctuations of δ and γ brings :

$$\Delta\delta \sim \frac{\Delta\gamma l^4}{16Ee^4}. \quad (3.23)$$

This expression suggests that the smaller the Young modulus, the larger the fluctuation of Δ . The Young modulus measurements summarized in Table 3.1 suggest that the pink rectangles are the most adapted to probe those fluctuations. We then chose to use pink rectangles characterized by a thickness of $800\mu\text{m}$. This thickness value was preferred to the $500\mu\text{m}$ because the experimental tests revealed that the thinner rectangles tend to exhibit large δ values, which do not exhibit discernible fluctuations with H .

Equation (3.4) can be used to estimate the typical expected surface tension variations on a given height. For $\Delta H \sim 10^{-2}$ m in the upper regions of the film (i.e. where surface tension shows weakest variations with H), surface tension varies from an amount of $\Delta\gamma \sim 0.1$ mN/m. The corresponding fluctuation for the deflection is $\Delta\delta \sim 10^{-5}$ m, which is quite small. In order to see such fluctuation, we used a microscope objective mounted on a digital still camera. For each different Q value, we took several pictures of δ at a given H . In order to verify the reproducibility of our measurements, the film was burst, then rebuilt, and a new measurement was then taken for the considered H . Those measurements were performed for feeding fluxes $Q \in [1.8 : 2.2]$ ml/min. The typical resolution accessed with our camera is $4.5 \cdot 10^{-6}$ m, leading to an accuracy of 20% on the δ measurements.

Figure 3.21 presents the experimental averaged γ values versus H for the different flow rates. As previously discussed, γ tends to increase with increasing H . On the other hand, for a given height H , γ is supposed to increase with Q , what is not shown by our experimental results. As explained in Chapter 2, the thickness profiles obtained with a given Q are subject to present considerable fluctuations, even if their overall shape remains unchanged. The general increasing trend for the thickness profiles (Fig 2.10) could only be emphasized by statistical averages. The same approach seems to be insufficient to discern the different flow values through the surface tension measurements. We have to mention here that the sensitivity of the surface tension measurements is less important than the one of the thickness measurements. This, added to the inherent physico-chemical fluctuations, may explain the poor sensitivity of our method to discern the different flow values.

Nevertheless, the solid curves presented in Figure 3.21 are the mean surface tension profile and the corresponding fluctuations presented in Figure 3.2. Despite the rather limited resolution of our measurements with respect to Q , the general trend exhibited by the averaged experimental values is well captured by considering the mechanical equilibrium in the film coupled with the statistical description of the thickness profiles fluctuations with Q . This quantitative agreement confirms the pioneering Gibb's idea about the link between surface tension forces and mechanical equilibrium in vertical soap films.

From a phenomenological point of view, the dependency of γ with H must be considered as a consequence of the stretching of the film interfaces. To conclude the discussion about these surface tension measurements, let us mention that a better agreement between the surface tension measurements and the mechanical equilibrium involving thickness profiles could be have been obtained by increasing the number of γ measurements at any height H . Such improvements may lead to separated surface tension profiles for the different Q values. This would surely strengthen the validity of our model to describe the mechanical equilibrium in vertical soap films.

The measurements presented on Figure 3.21 concern H ranging from 0.04 to 0.12 cm. This range has been chosen in order to avoid that the rectangle enters in contact with the top or bottom menisci. Since the rectangles are 3 cm tall, the bottom part of the rectangle was located 2.5 cm above the bottom edge of the frame for $H = 4$ cm, and its top was distant of 1.5 cm from the top edge for $H = 12$ cm. Note that this range is consistent with the one of the thickness measurements. Near the menisci, Eq.(3.4) is no more valid since we did not include any boundary conditions in our model. Moreover, the thickness profiles have not been characterized out of that range, so that it is not possible to conclude on the shape of $\gamma(H, Q)$ in the vicinity of the frame.

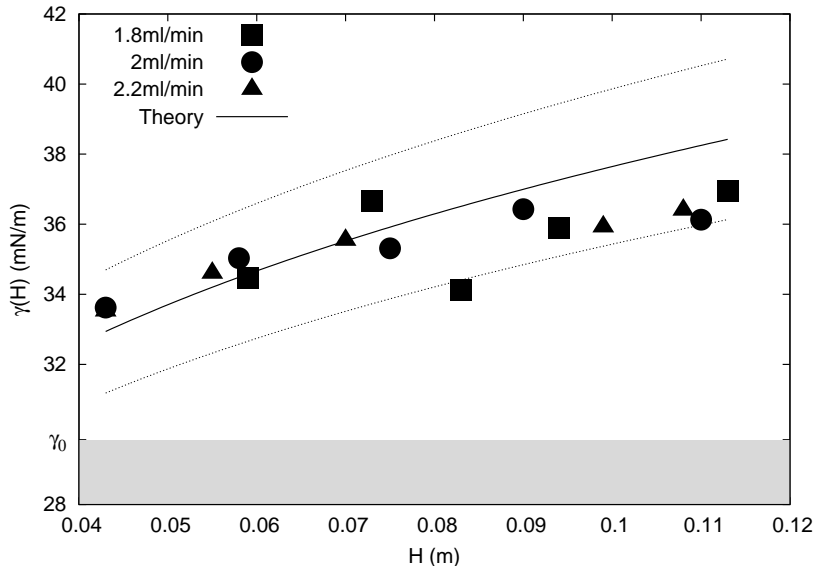


Figure 3.21: Surface tension γ versus the vertical coordinate H . Dots represent the averaged experimental values of γ for the different Q values. The solid and dashed lines are the curves presented in Figure 3.2, illustrating the quantitative agreement between Eq.(3.4) and the experimental values.

We did not consider the temporal evolution of the surface tension, since all our surface tension measurements were performed using maintained soap films. Nevertheless, our method could be applied using freely suspended soap films. Note that the corresponding temporal fluctuations of the thickness profiles would be required in order to check the validity of Eq.(3.4).

3.5 Conclusion

In this Chapter, we have shown that the elasticity of soft deformable objects can be used to build surface tension probes. We designed devoted sensors, which were theoretically characterized in order to link the shape they adopt once plugged into the films to the related surface tension value. Measurements of the surface tension profiles thanks to this method exhibited behaviors which are in agreement with simple logical considerations and the thickness measurements. The increase of the surface tension with H as been modeled by considering the mechanical equilibrium in the film, expressed recalling the thickness measurements presented in Chapter 2. Comparison between the experimental and the predicted surface tension profiles have shown that this model is suited to reproduce the experimental

data. This quantitative agreement confirms the role played by the surface tension in the mechanical equilibrium of soap films, as proposed by Gibbs in the late 1870 's.

Chapter 4

Two-dimensional buoyancy in vertical soap films

In this chapter, we re-consider the concept of buoyancy in the particular case of vertical soap films. Pioneering works from people like Couder [15] and Bruinsma [107] have evidenced that local thickness differences may play the role of the density-difference leading to the apparition of a buoyant force experienced by the film particles.

The fact that the thickness difference is the driving ingredient for two-dimensional buoyancy clearly indicates that it originates in the nearly 2-D nature of soap films. Thus, it should somehow be linked to the film interfaces. In the followings, we show that buoyancy in soap films can be re-interpreted in terms of the vertical surface tension gradients described in the previous chapter. We show that both approaches are strictly equivalent. In order to comfort this idea, we re-consider an experiments proposed by Couder and coworkers [15] in the particular case of our fed vertical soap films. We then show how it is possible to model the two-dimensional buoyancy in order to predict the motion of 2-D buoyant particles.

4.1 Context

Buoyancy is a basic phenomenon occurring when a compact physical medium (fluid or not) of density ρ_1 is immersed into a fluid of density ρ_2 [1,2]. Let a sphere immersed in water be (see Fig. 4.1). Two kinds of behaviors may occur, following the ρ_1 and ρ_2 values. If $\rho_1 > \rho_2$, the sphere sinks into water, as it can be observed if it is made of high density material such as lead, iron, mercury... On the other hand, if $\rho_1 < \rho_2$, the sphere rises up against gravity to the water surface. This is observed with low density woods, plastics, oil... Objects exhibiting those uprising motions are said to be buoyant. Simple dynamical considerations can be used in order to identify the parameters leading to buoyancy. Let us first consider the case

of a water sphere in water. The weight of this sphere is given by $\rho_2\Omega g$ if Ω is its volume. In order for the sphere not to move, it is necessary that an upward force compensates this weight. This force is called the buoyancy force, and is applied to any immersed objects by the surrounding fluid. Since this buoyancy force B must compensate the weight of the sphere, it is then expressed as $B = \rho_2\Omega g$ for the case of the water sphere. This force originates in the hydrostatic pressure applied to the sphere by the surrounding fluid. Now consider what happens if the inner density of the sphere is changed, i.e. if another material is immersed in the water. The weight of the sphere is given by $\rho_1\Omega g$. Since the buoyant force leading to the steadiness of the water sphere can only come from its surroundings, this force acts whatever the value of the inner density. The net force acting on the sphere then writes :

$$F = B - \rho_1\Omega g = \Delta\rho\Omega g, \quad (4.1)$$

where $\Delta\rho = \rho_2 - \rho_1$. This expression shows that the direction of the net force acting on the sphere only depends on the sign of the density difference $\Delta\rho$, in agreement with everyday experience.

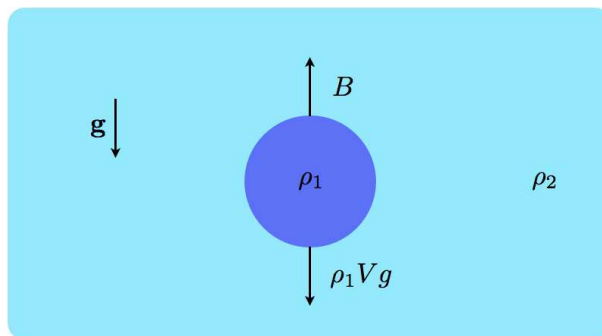


Figure 4.1: Scheme of the forces acting on a spherical object of density ρ_1 immersed in water (or any fluid medium) of density ρ_2 . The sphere volume is Ω .

If $\rho_1 < \rho_2$, the sphere rises up until it reaches the interface. Once the top of the sphere reaches the interface, the immersed volume Ω decreases and the the upward buoyancy force B does so. The upward motion stops when B exactly compensates the weight of the sphere. Note that this equilibrium at the interface can be reached even if $\rho_1 > \rho_2$, actual boats being a good example. If thin enough, materials such as iron, or even lead can float. In fact, if the immersed volume is large enough, the buoyancy force can become larger than the total weight of the body to be immersed, which then floats.

4.2 Buoyancy in vertical soap films

As emphasized in Chapter 1, soap film particles may become buoyant under particular conditions. The marginal regeneration phenomenon (see Section 1.8) is an example of naturally buoyant particles in the film. Careful observations of those buoyant particles during their rising show that they are always thinner than their surroundings [15, 30, 41, 42]. Figure 4.2 is a picture of regenerated particles rising up in a vertical soap film lit with a sodium lamp. The color of the rising particles is the opposite of the one of the fringes they are crossing, confirming the existence of the thickness difference.

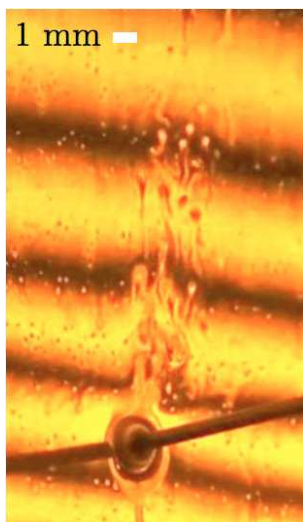


Figure 4.2: Image of regenerated particles rising in the film. The color difference between the film and the particles makes them visible and attests from the thickness gradient they exhibit with respect to their surroundings.

In order to draw a link between the density fluctuations and the thickness differences, a two-dimensional density for the case of two-dimensional soap films has been defined [55–57]. This density reads :

$$\rho_2 = \rho e, \quad (4.2)$$

where ρ is the density of the soapy solution and Δe the thickness difference. The resulting upward force writes :

$$B(H) = \rho g \int_S \Delta e(H) ds, \quad (4.3)$$

with S the area sustained by the buoyant particle [15]. This force is nothing

but the usual buoyancy expressed in the particular case of soap films. If Δe is a known function of H , it is then possible to express the buoyancy force acting on regenerated particles. As emphasized in Chapter 2, several ways exist for measuring the thickness of a soap film. Therefore, the behavior of Δe versus H may then be experimentally characterized. However, depending on both the experimental conditions and the thickness measurement technique, measuring the position and the thickness of a buoyant film particle at the same time might be difficult to realize experimentally. In fact, both measurements may not be possible to realize at the same time. An example is given in Chapter 5, where the position of the particle is accessible, while its thickness is impossible to measure due to the experimental conditions. In the next Sections, we will focus on a simpler experiment, which does not require thickness difference measurements and particle position at the same time.

4.3 Floating hair rings

In the followings, we re-consider an experiment realized by Couder and coworkers in 1989 [15]. The idea of this experiment is based on a common demonstration for the existence of surface tension in soap films by introducing a soft deformable ring in the film, as illustrated in Figure 4.3 (extracted from [1]) [39, 109]. As soap films are present both inside and outside the ring, this latter stays at rest in the film, with no particular shape (left picture in Figure 4.3). This situation is explained by the fact that the surface tension force acts equivalently on each side of any ring element, so that the interfacial net force acting on them is null (i.e. the pulling applied by the inner film is the same than the pulling applied by the outer film, for each ring element). But once the inner film is burst, the outer soap film applies a net radial surface tension force $2\gamma dl$ on every ring element, conferring a circular shape to the ring. In addition to its illustrative value, this experiment shows that it is necessary to create mechanical equilibria ruptures for experiencing the effect of surface tension forces linked to air/liquid interfaces.

Couder and coworkers have shown that if the ring is light enough and set into a vertical soap film, it may rise up in the film, as regenerated particles do [15]. The rising motion begins right after the inner film is burst. From an interfacial point of view, this burst leads to the apparition of a net interfacial force acting on the ring. From a two-dimensional buoyancy point of view, this burst creates a thickness difference between the fluid particle defined by the ring and the surrounding soap film, leading to a net upward force if the ring is light enough. The absence of soap film inside the ring simplifies the thickness difference calculation since it reduces to the thickness profile considered in the area defined by the ring. It is then possible to know the driving buoyancy force for any value of H , as :

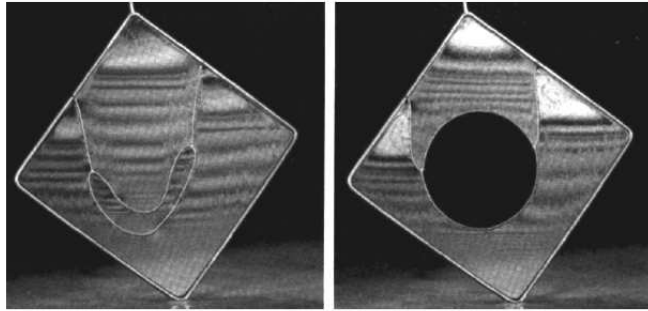


Figure 4.3: Pictures of a soft deformable ring introduced in a soap film. Left : soap films are present both inside and outside the ring. Right : after the inner film burst, the ring adopts a circular shape, as a consequence of the radial net force applied by the surface tension of the outer soap film on every ring element. Those picture are extracted from [1].

$$B(H, Q) = \rho g \int_S e(H, Q) ds, \quad (4.4)$$

with clear notations. Note that B increases if S and e increase, which is analogous to the volume dependency of the 3-D case. It is thus possible to investigate the motion of such buoyant rings in soap films as a function of both the ring and the film characteristics.

In order to realize such experiments, we had to find a material which is so light that we could build rings which are large enough to be easily tracked and buoyant at the same time. Human hairs appeared very well suited in this context. In fact, human hairs simply need to be glued to themselves for obtaining rings, which can then be introduced by hand in the vertical soap film. Four ring radii were considered : 8.69, 13.07, 14.56 and 16.39 mm. Observations thanks to a high resolution microscope showed that the hair diameter D is close to 100 μm . The rings were then weighted with an electronic balance with a sensitivity up to 10^{-5} g. The physical characteristics of the rings we studied are presented in Table 4.1. The corresponding density ρ_{hair} and the linear mass χ_{hair} are 657 kg/m^3 and 1.23e-5 kg/m , respectively.

The soap films were generated as usually, using the technique presented in Chapter 2. In order to follow the motion of the rings within the films, a high speed camera was used. Preliminary tests evidenced that the typical rising time τ_{rise} for the rings is approximately 0.1 s. We then chose to acquire frames with a 250 Hz frequency. Figure 4.4 presents a typical sequence of images of a buoyant ring acquired during its rise. The spatial resolution is $\sim 10^{-4}$ m.

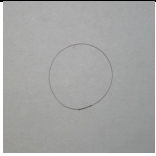
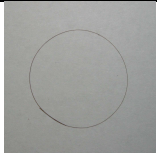
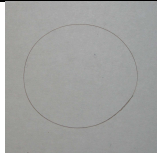
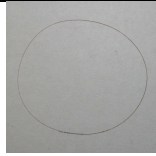
Ring pictures				
Radius (mm)	8.69	13.07	14.56	16.39
Mass (10^{-7} kg)	5.1	6.7	8	9

Table 4.1: Pictures of the different rings used in experiments. The corresponding radii and masses are presented.

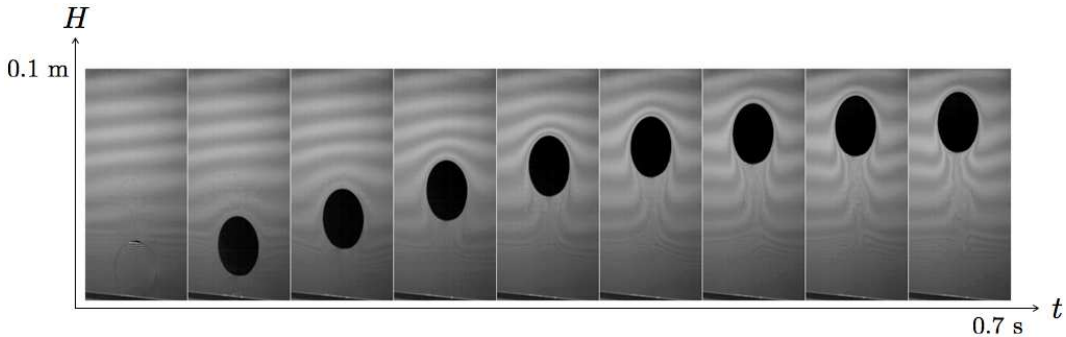


Figure 4.4: Shots of a ring at several times of its rise, for $R = 14.56$ mm and $Q = 2$ ml/min. The time interval between images is 80 ms.

When the ring is initially set in the film, soap films are present both inside and outside the ring (see first image in Figure 4.4). The inner film can then be bursted by the experimenter if necessary. In the particular case of our experiments, the inner film bursts naturally a few tens of seconds after the ring was set in the film. This spontaneous burst comes from the fact that the ring defines its inner soap film, which is not fed by the imposed flow. As a consequence, this film must be considered as a free suspended one, characterized by a limited lifetime. Right after the inner film is burst, a rapid rise of the ring is observed and followed by a saturation at an equilibrium height noted H^* . This latter quantity increases with both the radius R of the ring and the magnitude of feeding flow Q , as illustrated in Figure 4.5. Note that those observations are in agreement with the dependency of $B(H, Q)$ on the sustained area and thickness differences (see Eq.(4.4)).

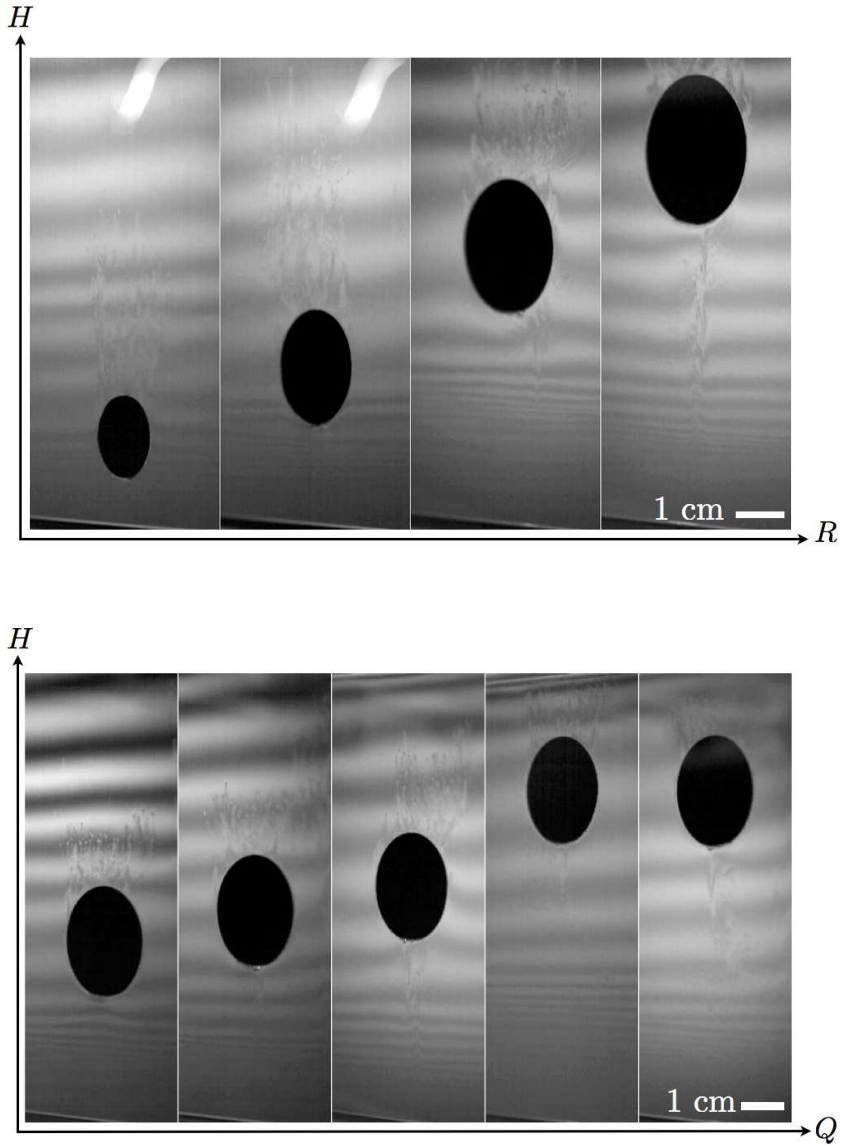


Figure 4.5: Pictures of the rings right after their rise. Top : these pictures correspond to films maintained with $Q = 2\text{ml}/\text{min}$. The radius of the ring increases from left to right. This figure illustrates that H^* increases with R . Bottom : these picture correspond to a ring of 14.56 mm in radius. The feeding flow rate increases from left to right. This picture shows that H^* increases with Q .

4.3.1 Link with surface tension profiles

We now consider the mechanical equilibrium of a ring plugged in the film, with no soap film present in the inner area. We showed in Chapter 3 that vertical surface tension gradients exist in our fed soap films. Any object plugged in a vertical film should somehow feel those gradients, as far as its size is significantly large in comparison with the typical variation scale of those gradients. Figure 4.6 illustrates the surface tension forces acting on a ring when plugged in such a film.

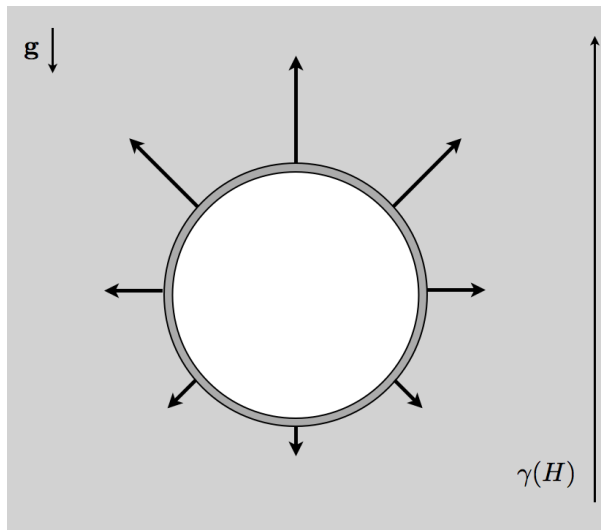


Figure 4.6: Schematics of the surface tension forces acting on a ring plugged in a vertical soap film. Due to the vertical surface tension gradient, those forces are larger on the top than on the bottom of the ring. The length of the arrows represent the strength of γ at the considered position.

Surface tension gradients imply that surface tension forces acting on the ring are larger at the top than at the bottom, what leads to a upward net force F_γ on the ring. We can use Eq.(3.4) in order to evaluate this net forces :

$$F_\gamma(H, Q) = \oint 2\gamma(H, Q)\mathbf{n} \cdot \mathbf{u} dl, \quad (4.5)$$

where \mathbf{n} is the normal unitary vector associated to the circular coordinate defined by the ring, and \mathbf{u} is a unitary vector defined as $\mathbf{u} = -\mathbf{g}/g$.

Let us now consider a circular film particle in the film, as defined by the ring, and located at a height which is so that the particle is not in contact with the lower border of the frame. From a mechanical point of view, if the particle is steady,

its weight must be counterbalanced by an upward force. The net surface tension force defined by Eq.(4.5) actually plays this role. Moreover, the two dimensional buoyancy applied on the ring by its surroundings as defined by Eq.4.4. In other words, those mechanical considerations bring that the surface tension forces must be identified as being the physical origin of the two-dimensional buoyancy in soap films. In terms of driving forces, we can then write :

$$B(H, Q) = F_\gamma(H, Q). \quad (4.6)$$

Since both thickness and surface tension profiles are known from experiments (see Chapters 2 and 3, respectively), it is possible to compute both $B(H, Q)$ and $F_\gamma(H, Q)$ in order to check the validity of Eq.(4.6). Figure 4.7 shows a superposition of both expressions versus H for fixed R and Q values. If H is smaller than R , both forces increase with H . In terms of surface tension forces, this growth is due to the fact that only the top part of the ring is set in the film. From the buoyancy point of view, this increase can be seen as a consequence of the progressive increase of the immersed volume with H . When H becomes higher than R , both forces begin to decrease. In terms of surface forces, this is due to the fact that the forces acting on the lower part of the ring have to be taken into account in the total net force for those H values. In terms of buoyancy, this is a consequence of the decrease of the immersed volume linked to the decrease of the thickness with H . For high values of H , both forces decrease with H . This is a consequence of the decrease in magnitude of both the thickness and surface tension gradient with H .

The inset of Figure 4.7 represents the difference of both forces as a function of H . For $H < R$, a non null difference is observed, while for $H > R$ this difference is equal to 0 whatever the H value. The non-null value of the difference for weak H comes from the fact that the ring is not fully set in the film if $H < R$. The negative value of the difference in this H domain means that the surface tension forces are stronger than the corresponding buoyancy. This can be interpreted by the fact that surface tension forces mainly act upward if the ring is not fully plugged in the film (i.e. forces acting downward on the bottom of the ring are not involved in the net force). As the ring is progressively introduced in the film, the force difference decreases as the surface tension pulls further on the lower part of the ring. From a phenomenological point of view, the non-null value of the difference for $H < R$ can be seen as a consequence of the vectorial nature of the surface tension force, in opposition to the unidirectional nature of the buoyancy. The equilibrium is reached once the ring fully plugged in the film, and holds whatever the position of the ring in the film. Note that the negative value of the difference for $H < R$ implies that the film tends to suck the ring toward upper regions when this latter is not fully plugged in.

The most important fact about Figure 4.7 is that these independently computed forces perfectly match for any value of R and Q . This confirms the validity of Eq.(4.6). Note that the previous analyze made in terms of surface tension could also be made in terms of surface pressure, via Eq.(1.9). Form this point of view, the interpretation of the buoyancy force as resulting from the pressure gradient acting on the ring is analogous to the interpretation of three-dimensional buoyancy with respect to the hydrostatic pressure gradient.

It should eventually be underlined that this phenomenon is also responsible for the regenerated particle motion (see Fig. 4.2 and Chapter 1). The thickness difference created by this regeneration reduces the weight of the particle, breaking its mechanical equilibrium. Therefore, the surface tension gradients act as an upward driving force, responsible for the rising of regenerated particles.

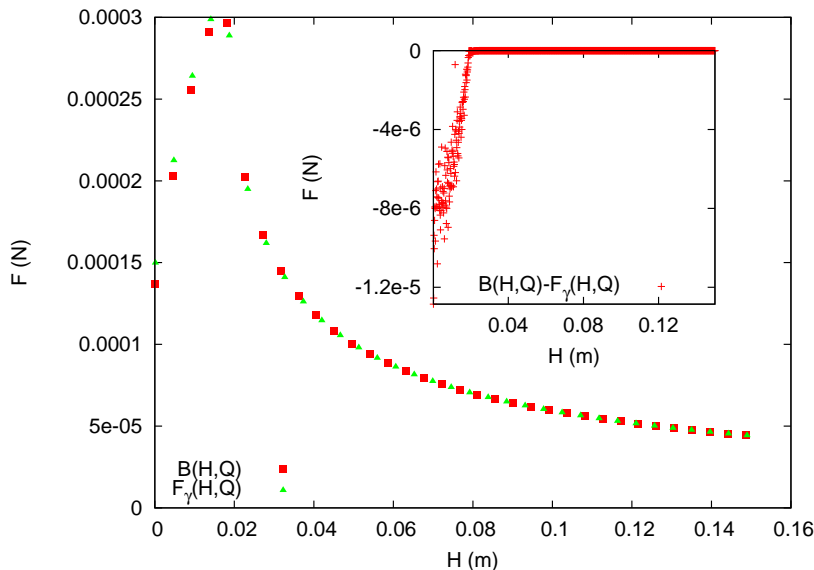


Figure 4.7: Buoyancy B and surface tension force F_γ versus the vertical position H in the film for a ring radius $R=22\text{mm}$ and a feeding flux with $Q=2\text{ml/min}$. Inset : difference $B(H,Q) - F_\gamma(H,Q)$ as a function of H . The non-null values for $H < 0.022$ m come from numerical integration of those forces when the ring is not fully plugged in the film. This difference arises from the vectorial nature of the surface tension force, opposed to the unidirectional buoyancy.

4.4 Dynamics of buoyant rings

We now focus on the rising dynamics of the hair rings in our vertical soap films. Figure 4.8 illustrates three typical measurements for H versus time, associated

with three different (Q, R) couples. For large (Q, R) values, the ring rises straight to the top of the film, with no transition regime between the rise and the following equilibrium. For intermediate values, the rise is followed by oscillations of $H(t)$ around H^* . Those oscillations are damped within a few seconds. Smaller Q and R values are characterized by larger oscillations around H^* , but with a damping time being of the same order of magnitude than in the intermediate case. As a summary, the experiments show that for any value of Q , the smaller the radius, the lower the ring rises.

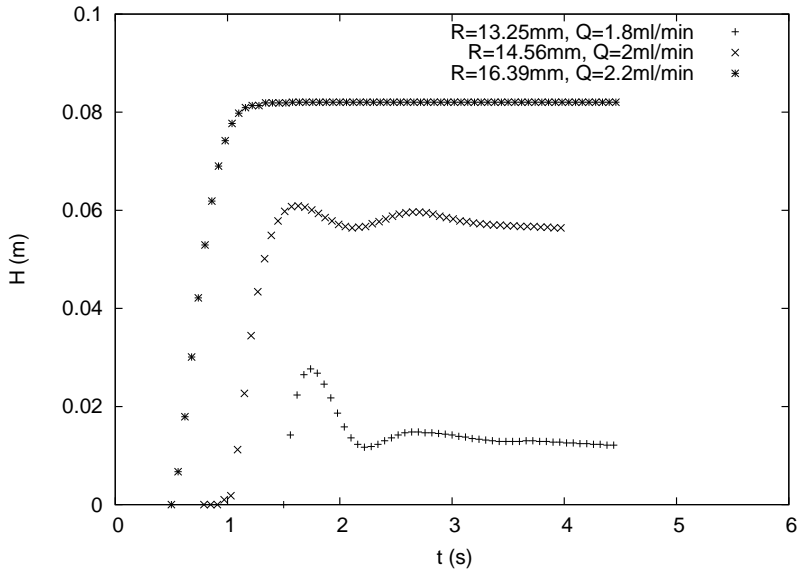


Figure 4.8: Typical examples for height versus time for three different (Q, R) couples. Time origins of each curve have been shifted for visibility.

A first attempt of dynamical description for the ring rises can be proposed by opposing the driving force F_γ to the weight of the ring, namely :

$$m \frac{d^2 H}{dt^2} = F_\gamma(H, Q) - mg, \quad (4.7)$$

where m represents the mass of the rising ring. Numerical tests realized with m values as measured from the ring weighting lead to $H(t)$ curves such as presented in Figure 4.9. One clearly sees that Eq.(4.7) computed for the mentioned forces and masses fails to reproduce the experimental behaviors presented in Figure 4.8. From an experimental point of view, $H(t)$ should saturate to a value fixed at 0.15 m at most, since this latter value is the height of our films, kept constant for all the experiments. The curve $H(t)$ presented in Figure 4.9 either comes from an

overestimation of the driving force or from an underestimation of the ring mass. To obtain further insight on this issue, it is instructive to note that the mass of the rising ring should be refined by considering the mechanical equilibrium of the ring right after its rise. This mechanical equilibrium roughly writes :

$$mg = F_\gamma(H^*, Q), \quad (4.8)$$

so that it is possible to estimate m from experimental H^* values as obtained from Figure 4.8. When performing such estimations, we saw that all the masses of the rising rings at equilibrium are of the order of 10^{-5} kg, which is two order of magnitude higher than the masses as weighted outside the film! The consideration of the mechanical equilibrium after rise suggests that the mass of the ring once plugged in the film must be re-considered in order to find an extra-contribution, coming from the film itself.

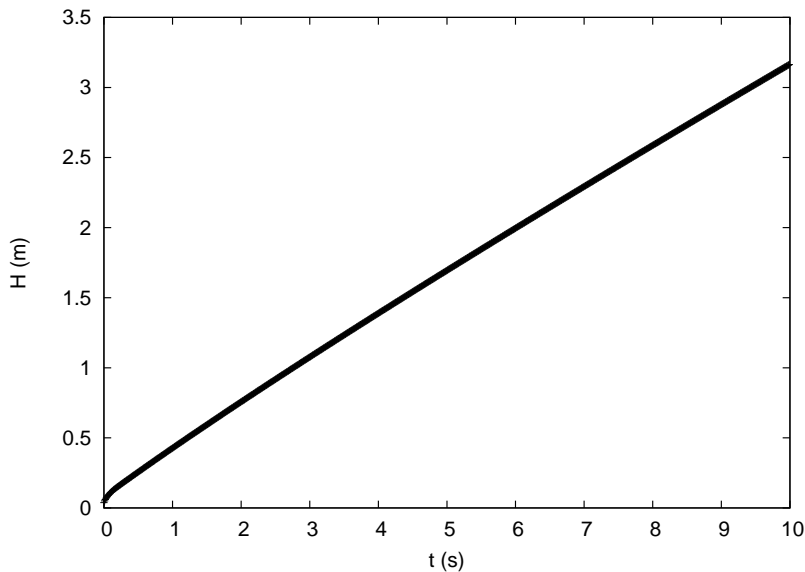


Figure 4.9: Rising curve $H(t)$ as computed from Eq.(4.7) for a ring characterized by $R = 14.56$ mm, $Q = 2$ ml/min and $m = 8 \cdot 10^{-7}$ kg as weighted outside the film. One clearly sees that Eq.(4.7) fails to reproduce the experimental saturation of $H(t)$ as presented in Figure 4.8. Numerical tests reveal that similar non-relevant results are obtained for any other rings.

4.4.1 Mass of the meniscus

Since the ring diameter D is larger than the typical film thickness, the film and the ring are linked thanks to a meniscus. Since this meniscus rises with the ring,

its mass must be considered as part of the apparent mass of the ring. This total mass m thus reads :

$$m = m_0 + m_{meniscus}, \quad (4.9)$$

where m_0 is the mass of the ring outside the film and $m_{meniscus}$ is the mass of the meniscus. This $m_{meniscus}$ quantity is determined as follows. The height of the meniscus can be evaluated by the capillary length $l_c(\gamma)$ (Eq.(1.5)) as a function of the ring position. Since the ring section is smaller than l_c , the width of the meniscus reduces to D . The mass of the meniscus can then be expressed as :

$$m_{meniscus} = \rho 2\pi R D l_c. \quad (4.10)$$

Introducing typical order of magnitude in this expression reveal that $m_{meniscus} \sim 10^{-5}$ kg, what is in agreement with the estimation of the ring masses obtained thanks to Eq.(4.8). This estimation shows that the mass displaced during the ascending motion of the ring mainly lies in the meniscus. It is now possible to re-consider Eq.(4.7) with the total mass of the rings. The numerical result are shown in Figure 4.10.

As one can see, even if the mass has been corrected, our dynamical description for the ring dynamics still fails in generating faithful reproductions of experimental behaviors. Among the dynamics itself, the spatial scale is badly predicted. We thus need to add extra dynamical contributions to Eq.(4.7). The fact that the numerical maximum height reached by the ring overpasses the height of the frame suggests that damping effects coming from the films should be considered for obtaining a relevant description of the ring dynamics.

4.4.2 Viscous drag

Since the ring moves in a liquid medium, it must somehow be submitted to viscous frictions from this fluid. We thus wished to express the viscous drag applied on the ring by the soap films, as a function of both the films and the rings characteristics. We chose to start from the basic definition of viscous forces as defined in [1] and [2] as :

$$F_f = \eta S \frac{dv}{dz}, \quad (4.11)$$

with η the dynamic viscosity of the fluid, S the total surface on which the friction applies, and dv/dz the transverse velocity gradient [1,2]. The viscosity of the surfactant solution can be obtained from tables contained in [14,68] to $\eta = 1.09 \cdot 10^{-3}$ Pa · s for the solution we used. For a ring, the surface S can be approximated by $2\pi R D$, where D is the diameter of the cross section of the hair the ring is made out. The velocity gradient can be approximated by v/z if v is the typical flow velocity and z the typical spatial extension of the velocity gradient. The

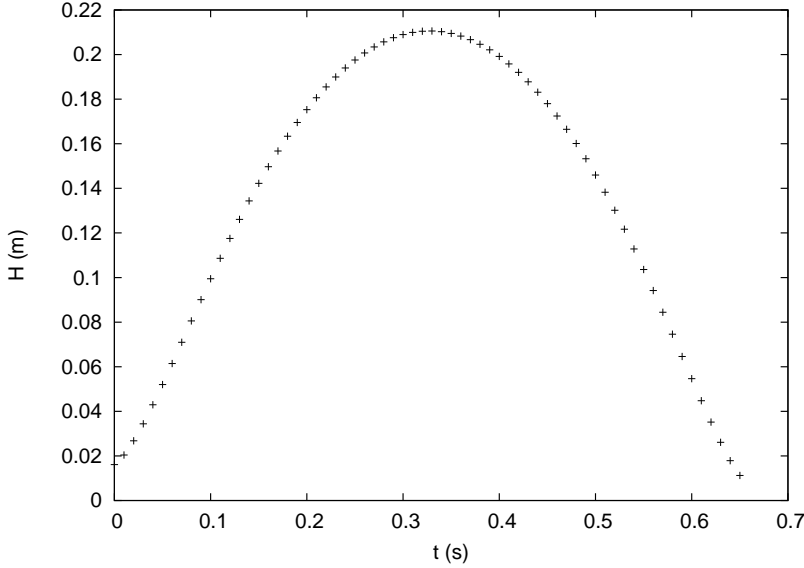


Figure 4.10: Evolution of $H(t)$ versus time as obtained by numerical computation of Eq.(4.7) with the mass of the ring expressed thanks to Eq.(4.9), for $R = 14.56$ mm and $Q = 2$ ml/min. Once again, the dynamical description of the ring dynamics we propose fails in reproducing the experimental data.

relative velocity, defined as the sum of the downward drainage flow velocity plus the rising velocity of the ring, must here be considered. As previously mentioned, the typical rising time scale τ_{rise} is of the order of 0.1 s, what means that the rising velocity is of the order of 0.1 m/s, which is at least one order of magnitude more important than the typical drainage velocities (see Fig. 2.12 in Chapter 2). To a first approximation, the film can thus be considered at rest during the rise of the ring. This fact coupled with the weak viscosity of the solution allows to approximate the typical spatial extension of the velocity gradient by D . In the end, the viscous drag acting on the ring writes :

$$F_f(H, Q) = 2\pi\eta R \left(\frac{Q}{e(H)L} + \frac{dH}{dt} \right). \quad (4.12)$$

This expression suggests that the larger is the radius and the larger is the flow rate imposed to the film, the larger is the friction on the ring. Note that the additional source of friction dH/dt comes from the film itself as well, since it is supposed to depend on both the surface tension profiles in the film and the mass of the ring once set in the film.

Added from the viscous drag, the dynamical equation for the ring rises then writes :

$$m \frac{d^2 H}{dt^2} = F_\gamma(H, Q) - mg - F_f(H, Q). \quad (4.13)$$

Numerical computing for the ring trajectories can then be re-considered using this expression. A typical result is presented in Figure 4.11. It can be seen that the consideration of the viscous drag as expressed by Eq.(4.12) leads to numerical trajectories which are pretty similar to the experimental ones presented on Figure 4.8.

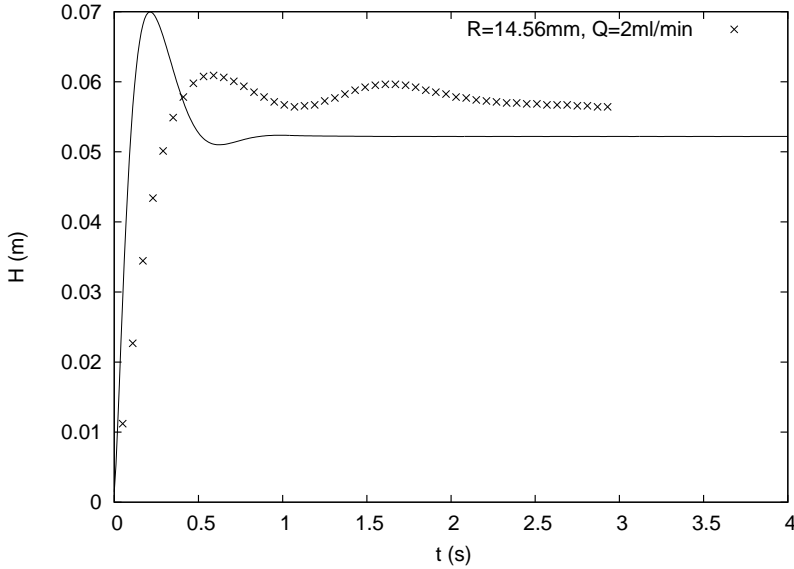


Figure 4.11: Comparison of the numerical $H(t)$ as obtained from Eq.(4.13) for $R = 14.56$ mm and $Q = 2$ ml/min (solid line) with an experimental corresponding curve. The consideration of the viscous drag applied by the films on the rings and described by Eq.(4.12) brings numerical trajectories exhibiting similar features with respect to experimental data.

4.4.3 Lubrication of the meniscus

Since the hair diameter is one order of magnitude larger than the typical thickness of the films, a meniscus exists between the film and the ring. Let us now focus on the top part of the ring. If the ring commences to rise in the film, so does the meniscus. From a thickness point of view, this implies that the thickness of the upper film regions must adapt itself to the meniscus thickness as the ring reaches those regions. The same effect takes place at the bottom of the ring. The top part of the ring is somehow enlarging the film as it moves through it while the bottom part shrinks it. This phenomena is reminiscent of lubrication interactions [1, 2].

The Navier-stokes equations written for flows between two almost parallel plates show that the plates encounter an opposing pressure which can be estimated as :

$$P_{lub} \sim \frac{\eta v l}{h^2} \quad (4.14)$$

if v is the flow velocity, h the distance separating the plates and l the typical distance over which the flow occurs [2]. Again, we can consider v as being equal to the relative speed of the ring. The length l can be approximated by D and the surface on which the lubrication pressure acts is $2\pi R D$, which is the apparent surface of the ring. The lubrication force then writes :

$$F_{lub}(H, Q) = \oint \frac{2\eta D^2}{e^2(H)} \left(\frac{Q}{e(H)L} + \frac{dH}{dt} \right) \mathbf{u} \cdot \mathbf{n} dl, \quad (4.15)$$

where \mathbf{u} is the unitary vector previously defined (see Eq.(4.5)). Adding this lubrication force in the dynamical equation of the ring gives :

$$m \frac{d^2 H}{dt^2} = F_\gamma(H, Q) - mg - F_f(H, Q) - F_{lub}(H, Q), \quad (4.16)$$

where all the physical quantities implied in those forces are known from experiments. Tests made about the effect of the lubrication forces revealed that those latter lead to very weak modification with respect to the numerical trajectories. In fact, this force does not act on the oscillations observed right after growth. Moreover, the modification of the numerical H^* are so weak (a few 10^{-4} m) that they could hardly be seen on a superposition of $H(t)$ with and without lubrication. It is then difficult to conclude on the relevancy of lubrication forces in our system, in the sense that their weakness does not allow to identify their presence in the total force acting on the rings. Nevertheless, given the interfacial nature of the soap film and the hair diameter value, it appears relevant to consider those forces in the dynamical model.

4.4.4 Dynamical analysis

Further insights on the contribution of the different forces implied in Eq.(4.16) on the ring behaviors can be obtained by plotting the evolution of those forces versus H , as presented in Figure 4.12. The curve for the driving force F_γ is almost the same as the one presented in Figure 4.7, except that it has been considered from $H \geq R$. The magnitude of this force overpasses the magnitudes of all the other forces involved in the ring dynamics, until it crosses the constant force mg corresponding to the total weight of the ring. It is interesting to note that the abscissa at which this crossing occurs almost corresponds to the equilibrium height H^* as shown on Figure 4.11. This feature is in agreement with the dynamical

equilibrium after growth as expressed by Eq.(4.8).

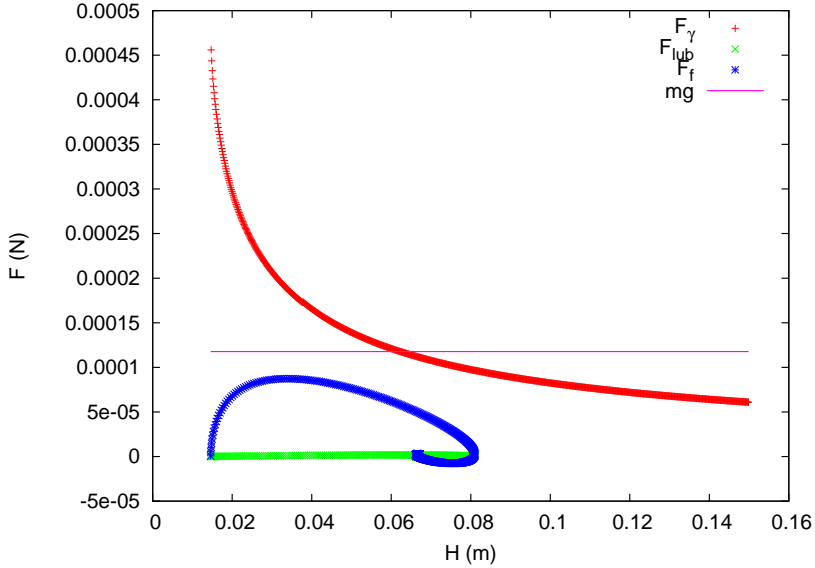


Figure 4.12: Evolution of the different forces involved in Eq.(4.16) versus H for $R = 14.56$ mm and $Q = 2$ ml/min. The changes in sign of the viscous drag F_f underlines its role with respect to the oscillations of $H(t)$. The weakness of the lubrication force F_{lub} illustrates its minor role on the H^* values. The abscissa of the crossing between F_γ and the weight of the ring corresponds to the value of H^* as presented in Figure 4.11.

The viscous drag F_f first rises for early H , then decreases and even changes in sign, before re-increasing to 0 for H close to H^* . This change in sign with H is equivalent to an oscillatory behavior around 0 versus t . Those variations identify F_f as being responsible for the oscillations of $H(t)$. The fact that the change in sign occurs for $H > H^*$ underline the damping nature of F_f .

As presented in Section 4.4, the larger ring does not exhibit any oscillation of $H(t)$, which goes straight to H^* while the smaller the ring exhibits damping. The viscous drag has been plotted in Figure 4.13 for various (R, Q) couples. Those curves show that the viscous drag does not exhibit any change in sign for the larger ring. As R and Q are decreased, sign fluctuations for F_f are more and more likely to happen, in agreement with experimental trajectories (see Fig. 4.8). Note that the viscous drag is never null in any case when $H(t) = H^*$, as a consequence of the presence of the drainage velocity $Q/e(H^*)L$ acting on the ring after its rise. To conclude the discussion on the different forces acting on the rings, it is necessary to draw a comment on the lubrication force. This latter evolution with H is

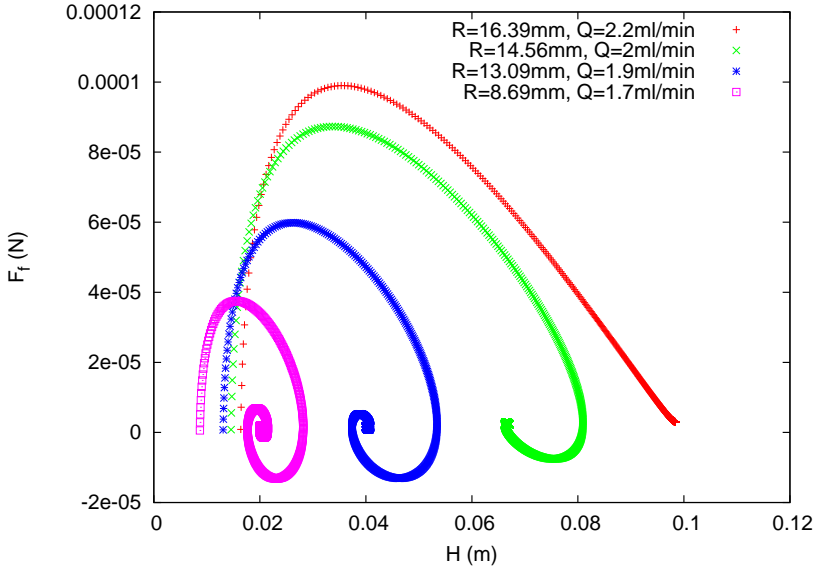


Figure 4.13: Evolution of the viscous drag F_f versus H for different (R, Q) couples. The smaller the (R, Q) values, the more changes in sign F_f exhibits.

plotted in Figure 4.14 and corresponds to the lubrication force plotted in Figure 4.12. Even if weaker in intensity, the lubrication force exhibit a behavior which is quite similar to the one of the viscous drag, in the sense that sign changes are observed as H increases. Note that this force stops to vary for $H = H^*$, which is analogous to the viscous drag case. In the cases considered here, F_f is always higher in magnitude than F_{lub} . However, there could be cases for which magnitudes could become similar (very small rings for example). Given the influence of those kind of oscillatory forces on the system, it might be possible that the lubrication force influences both the oscillations and the equilibrium height under different experimental conditions with respect to the one involved in the present work.

4.5 Equilibrium height and effective mass

Even if numerical predictions such as the one presented in Figure 4.11 are encouraging, the numerical solutions of Eq.(4.13) fail to quantitatively reproduce the equilibrium heights for the different rings. When considered for numerical solving, both members of Eq.(4.13) are divided by m , what implies that the mass slightly influences the force balance. Moreover, numerical tests revealed that the meniscus mass component of Eq.(4.9) must be rescaled by a prefactor in order to

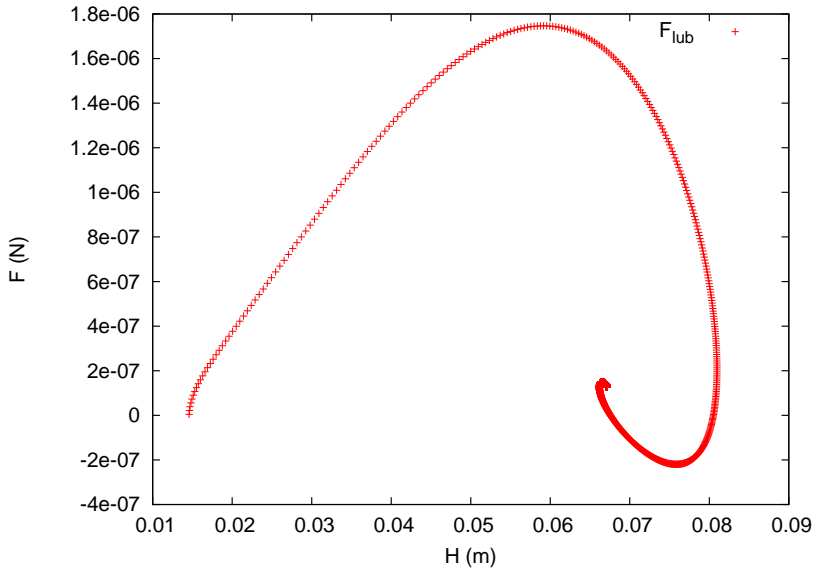


Figure 4.14: Lubrication force F_{lub} versus H for $R = 14.56$ mm and $Q = 2$ ml/min.

obtain relevant prediction of H^* . Typically, the mass of the meniscus must be reduced by 50 % for reproducing the value of the equilibrium heights of the larger ring, while it needs to be increased of almost 50 % for reproducing the equilibrium heights of the smaller ring. Since we wish to build a predictive model for the ring rises, we need to express their masses in a more straightforward way, and avoid the presence of any free parameter in our modelings.

On the other hand, the effective masses m^* as determined by considering the dynamical equilibrium of the ring after rise (Eq.4.8) reveal to faithfully predict the H^* values, whatever the R or Q values. These so-determined effective masses are plotted in Figure 4.15 as a function of H^* for the different ring diameters used in our experiments. Two main comments arise from those curves : (i) for a given H^* , the larger the ring, the larger m^* , and (ii) for a given m^* , the larger the ring, the larger the H^* . Those observations are in agreement with the fact that both the mass and the equilibrium height are supposed to increase with R . In order for Eq.(4.16) to be a predictive model for the ring rises, the effective masses m^* have to be determined independently from the dynamical equilibrium reached after the rise.

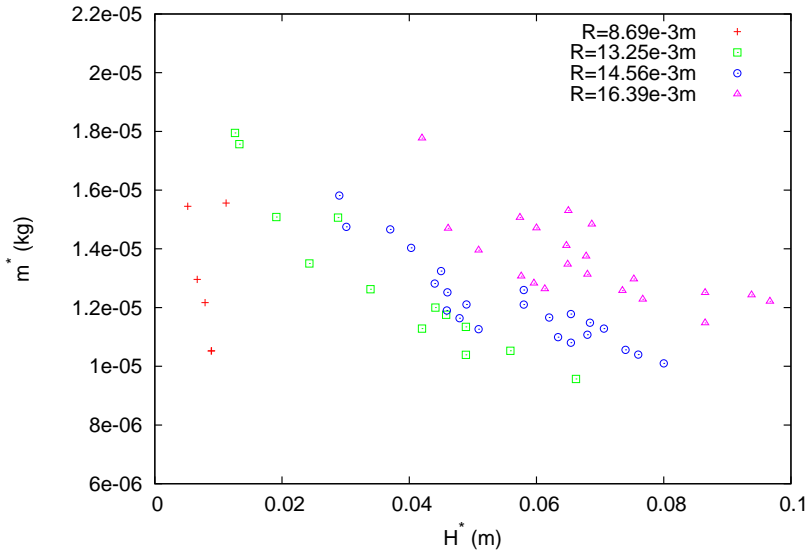


Figure 4.15: Evolution of the effective mass m^* of the rings with the equilibrium height H^* .

4.5.1 Liquid front and momentum

Careful observation of the successive images of the rings during their rise shows that they induce perturbations of the interferometric fringe pattern inside the film. This effect is visible in Figure 4.16, as well as in Figure 4.4. From the second image of Fig. 4.4, one sees that the fringe pattern lying above the ring is bent on a distance of the order of magnitude of R . This perturbation implies that a liquid front rises up in the film with the ring. The mass of this liquid front must be taken into account in order to consider the total mass involved in the rise.

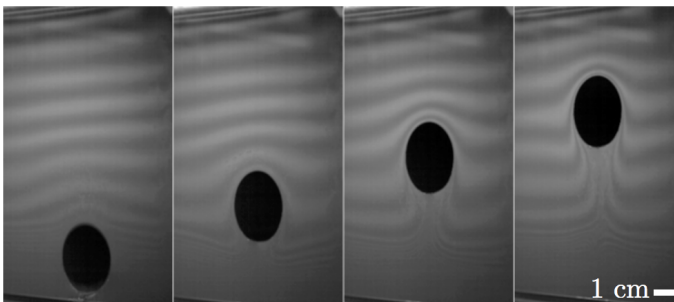


Figure 4.16: Illustration of the liquid front preceding the ring during its rise. The deformation of the fringe patterns evidences the existence of this front.

During the rise, the momenta of the ring (front included) and the drainage flow are facing each other. It has been shown in various situations [2,3] that the opposition of two flows characterized by different momenta can lead to the apparition of a steady point schematized in Figure 4.17. This point can be used in order to characterize the typical spatial extension ℓ of the front.

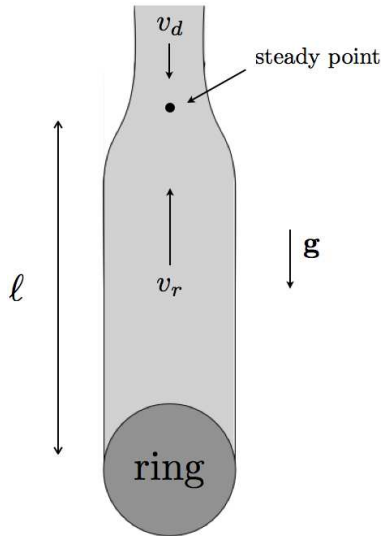


Figure 4.17: Transverse cut of the liquid front preceding the ring during its rise (not to scale).

Let us compare both momentum magnitudes of the ring and the drainage flow. If the fluid front thickness is assumed to be equal to the ring diameter on the whole front extend, then the front momentum can be expressed as $\rho\pi RD\ell v_r$, where v_r is the typical rising velocity of the ring. This momentum opposes the one of the liquid column lying above the ring, which depends on the position of the ring. If the width of this column is assumed to be equal to the diameter of the ring, the downward momentum can be expressed as :

$$2R\rho \int_H^L e(h)v_d dh \sim \frac{2R\rho Q(L-H)}{L} \quad (4.17)$$

if the drainage velocity is expressed as :

$$v_d \sim \frac{Q}{e(H)L} \quad (4.18)$$

thanks to flow conservation. Equaling both momenta leads to an expression for the typical extend of the front, being :

$$\ell \sim \frac{2RQ(L-H)}{L\pi R D v_r}. \quad (4.19)$$

Considering that the front thickness is equal to the diameter of the ring all along ℓ , the total mass of the rising ring writes :

$$m^* = m_0 + A \frac{2R\rho Q(L-H)}{L v_r}, \quad (4.20)$$

where m_0 is the mass of the ring as weighted before plugged in the film, and A is a multiplicative coefficient. In order to further simplify this expression, v_r can be approximated by the mean velocity of the ring during its rise. Doing so, it is possible to obtain an analytical expression for m^* as a function of H^* . The solid lines presented in Figure 4.18 are Eq.(4.20) plotted for the rings characterized by radii of 13.25, 14.56 and 16.39 mm. The nice agreement between experimental values of m^* and Eq.(4.20) is obtained for $A = 3$. Since Eq.(4.20) involves Q , several curves can be drawn for each ring. For a matter of visibility, we chose to illustrate only the curves corresponding to $Q = 2$ ml/min. Since this value represents the mean Q value used in experiments, the solid lines in Figure 4.15 illustrate the average trend followed by m^* with H^* .

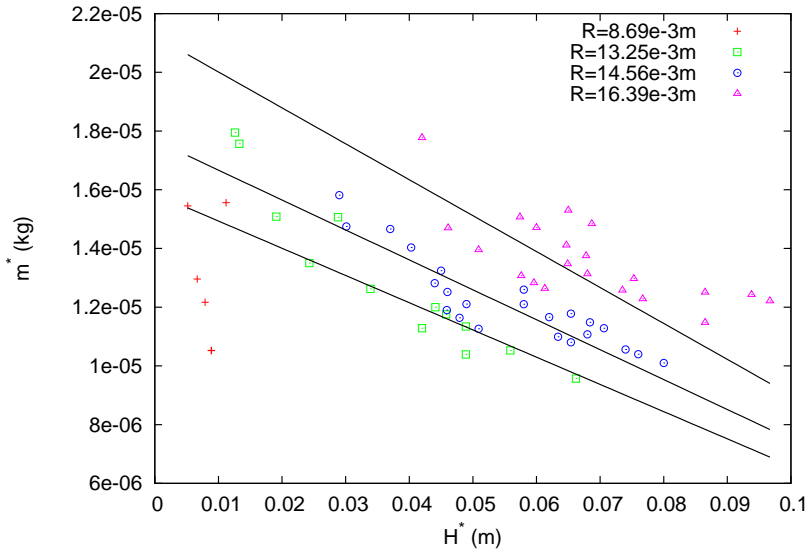


Figure 4.18: Comparison between the experimental effective masses and their theoretical expression as defined by Eq.(4.20).

Particular attention must be paid to the case of the smaller rings ($R=8.69$ mm). This rings effective masse exhibits a trend which is drastically different from the

one of larger rings, which our model for m^* clearly fails to reproduce. We have to note here this small ring exhibits very weak rises. In fact, for the weaker Q values, those rings difficultly take off from the bottom edge of the frame after the inner film is burst. In such conditions, the rising velocity v_r becomes quite ambiguous to define and our model for m^* , based on flow momenta, becomes irrelevant in that range.

One could wonder why m^* depends on H^* , i.e. why typical parameter values are not sufficient to describe the effective mass. We will see in next section that this effect results from the existence of a dispersion in H^* for fixed parameters.

4.6 Floating rings trajectories

Solid lines in Figure 4.19 are numerical results obtained from Eq.(4.16), computed using the corresponding experimental parameters and effective masses obtained by dynamic equilibrium at rest. Those curves show that our dynamical model for the rising rings is relevant in reproducing the equilibrium height H^* , the typical rising times and the damping oscillations for the different (R, Q) couples.

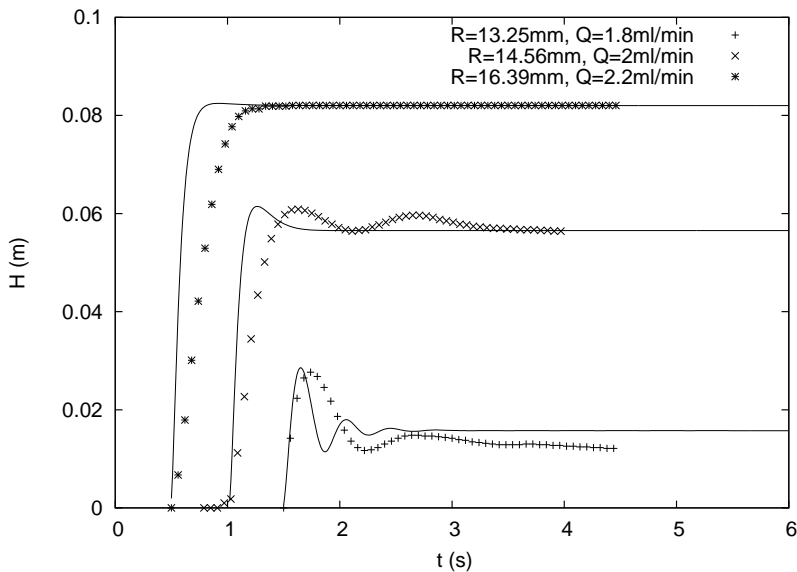


Figure 4.19: Comparison of the experimental and numerical trajectories obtained from Eq.(4.16) for a few (R, Q) couples.

In order to realize further tests for the validity of Eqs.(4.16) and (4.20), we considered the evolution of the averaged H^* versus Q for the different ring diameters, as plotted in Figure 4.20. These curves show that H^* increases with both R and

Q values, in agreement with the behavior of the driving forces with those parameters. The error bars in Figure 4.20 represent the variance of the corresponding H^* . The dispersion of H^* has to be regarded as a consequence of the dispersion of $e(H)$ and the corresponding $\gamma(H)$ with Q . Note that the error bar overlaps also shows that rings can only be separated by statistical considerations.

The solid lines in Figure 4.20 represent the numerical value of H^* obtained from Eq.(4.16), where the effective masses m^* have been determined thanks to Eq.(4.20). This figure shows that the numerical data are in quantitative agreement with the experimental values of H^* , underlining the validity of our model for the rise of hair rings in vertical soap films.

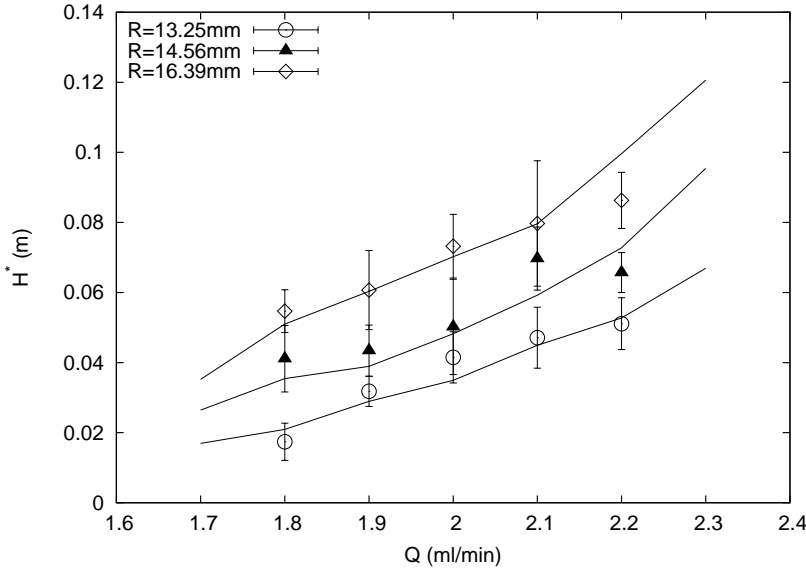


Figure 4.20: Equilibrium height H^* versus the feeding flux Q for the different ring diameters. Points are averaged experimental values, solid are lines the numerical solving of Eq.(4.16) considered for m^* as expressed by Eq.(4.20).

4.6.1 Critical ring radius

During the first tests we performed with the rings in soap film, we evidenced that the smaller the radius, the harder it is for the ring to rise in the film, whatever the Q value. A critical radius value should thus exist, under which it is impossible for the ring to rise in the film after the inner film is burst. This critical radius comes from the fact that the driving force decreases with R , added with the fact that initial viscous drag and lubrication forces (i.e. when $dH/dt = 0$) have to be counterbalanced in order for the ring to take off. At $t = 0$, the mechanical equilibrium for the ring writes :

$$F_\gamma = mg + F_f + F_{lub}. \quad (4.21)$$

For a purpose of simplicity, the lubrication force can be simplified as $F_{lub} \sim \eta UD/e^2 S$ with S the surface on which the lubrication pressure acts. After developments, the radius leading to this equilibrium reads :

$$R_c = \left(\frac{(\frac{\mu\pi Q}{eL} + 2\pi R\chi_{hair}g + \rho g 2\pi D l_c + \frac{\eta Q l_c \pi D}{e^3 L})(1 - \beta)}{\rho g a I} \right)^{\frac{1}{1-\beta}}, \quad (4.22)$$

with χ_{hair} the linear mass of the hair, l_c the capillary length, and I a constant value. The mass of the ring as been expressed as $m_0 + \rho g 2\pi R D l_c$, since no liquid front develops above the ring in this case. This quantity represents the limit value of R under which it is not possible for rings to rise up. This expression is plotted in Figure 4.21 as a function of Q . This Figure illustrates that R_c decreases with Q , which is consistent with previous observations. The dots in Figure 4.21 represent the R values used in our experiments. Those values are quite large with respect to the corresponding critical radii. This is intriguing since the smaller rings we built may exhibit difficulties to take off the bottom of the film for lower Q values. This gap between critical and actual values must be regarded as an indication that the friction and lubrication forces tend to damp buoyancy rather smoothly when R becomes small.

4.6.2 Discussion on the mass problem

Figure 4.15 illustrates that the order of magnitude of m^* is typically 10^{-5} kg, which is actually the same order of magnitude as the total mass m defined as the mass of the ring plus the mass of the meniscus (Eq.(4.9)). Following its very intuitive expression, one can then wonder why Eq.(4.9) fails to predict the mass of the rising rings. The curves presented in Figure 4.22 represent the evolution of the difference between m and m^* as respectively defined by Eq.(4.9) and Eq.(4.20) versus H . Those curves have been considered for $Q = 2$ ml/min. For a matter of simplicity, we considered that the capillary length defining the meniscus is fixed and equal to the capillary length of the surfactant solution.

The main observation on those curves is that $m > m^*$ for any ring. Given the relevancy of m^* with respect to numerical ring trajectories, m as expressed by Eq.(4.9) must be regarded as an overestimation of the total mass of the rising rings. Note that the growing behavior of $m - m^*$ with Q is in agreement with the fact that the more important H^* is, the more the mass of the rising ring is overestimated.

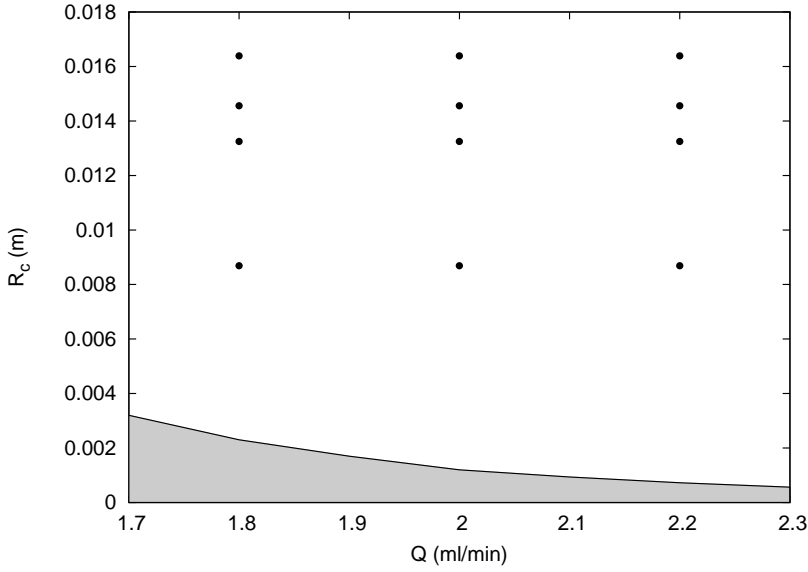


Figure 4.21: Critical radius R_c as a function of Q . The greyed area corresponds to R values which do not lead to ring rises for corresponding Q . The dots represents the R values used in experiments.

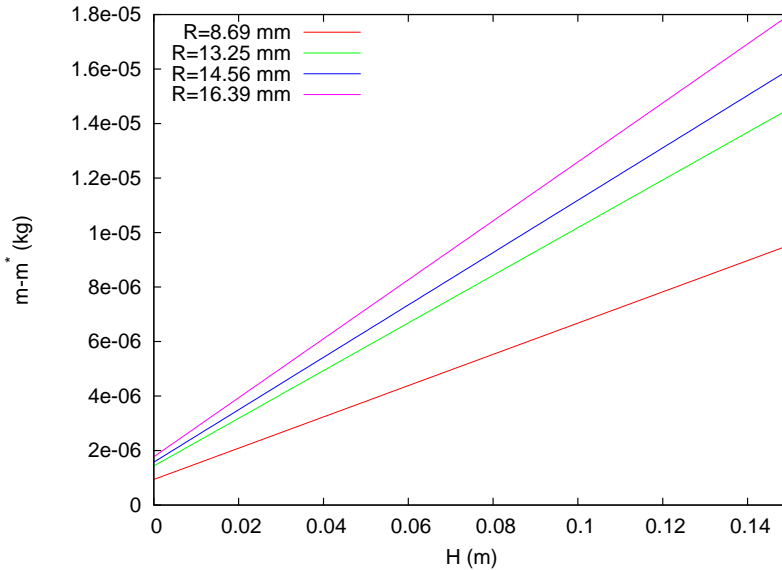


Figure 4.22: Difference between m (defined by Eq.(4.9)) and m^* (defined by Eq.(4.20)) versus H for a fixed flow rate ($Q = 2$ ml/min).

An explanation can be developed for justifying the relevancy of m^* with respect to m . In the particular case where the ring is at rest in the film (i.e. before and after its ascending motion), it is rather natural to consider that a meniscus surrounds the ring. The existence of this surroundings once the ring is set into motion might not be that obvious. As presented in previous sections, once the inner soap film in the ring bursts, the ring is set into motion quite violently. It is thus not impossible for the fluid contained in the meniscus to flow out of this latter once the rise is started. Following this assumption, the scenario proposed for the effective mass defined by the liquid front preceding the rings appears as natural. Experimental techniques such as fast camera imaging or PIV could be envisaged to justify the emptying of the meniscus right after the rise has started.

4.6.3 Discussion on the interfacial viscous drag

As evoked in Chapter 1, the surface viscosity of a SLES+CAPB solution is of the order of $2 \cdot 10^{-3} \text{ Pa} \cdot \text{s} \cdot \text{m}$ [36]. Let an air/water interface loaded with surfactant molecules be. If an object of size R is moving along this interface, the Boussinesq number compares the magnitude of the friction exerted by the bulk and the interface on the object. This number is defined as :

$$\text{Bq} = \frac{\eta_S}{R\eta_B}, \quad (4.23)$$

where η_S is the interface viscosity and η_B is the bulk viscosity. $\text{Bq} \ll 1$ means that the bulk friction is larger than the interfacial friction, which can then be neglected. On the other hand, if $\text{Bq} \gg 1$ the interfacial viscosity is larger than the bulk viscosity, and the object can be considered to move in a bi-dimensional fluid formed by the surfactant layer [110]. The evaluation of Bq for a typical ring radius $R \sim 10^{-2} \text{ m}$ and a bulk viscosity of $1.09 \cdot 10^{-3} \text{ Pa} \cdot \text{s}$ brings that $\text{Bq} \sim 10^2$. This value suggests that interfacial viscous effects should be taken into account in our modeling for the total viscous drag acting on the rings. However, as presented in the previous sections, the consideration of the only bulk viscosity has brought faithful predictions for the ring dynamics on the whole range of experimental parameters. This fact is in contradiction with the value of Bq linked to our rings. The viscous drags applied by the bulk and the interface on the ring can be evaluated in order to obtain further insights on this discrepancy. From Eq.(4.12), the drag applied by the bulk can be estimated as $D_B \sim \eta_B R V \sim 10^{-5} \text{ N}$, if V represents the relative velocity of the rising ring, estimated as $V \sim 10^{-1} \text{ m/s}$ from experimental data (see Fig. 4.4). The drag linked to the interface can be estimated similarly. Eq.(4.11) can be adapted to the case of the interfacial friction as :

$$D_S = \eta_S l \frac{dv}{dz}, \quad (4.24)$$

where l represents the length on which the interfacial friction is applied. Considering the same estimation for dv/dz as for the case of the bulk viscosity, one obtains :

$$D_S \sim \eta_S l \frac{V}{D} \sim 10^{-2} \text{ N}, \quad (4.25)$$

if $l \sim R$, what is consistent with the case of the ring. This estimation stands that the interfacial friction is of the order of 10^{-2} N, while the typical order of magnitude of the bi-dimensional buoyancy is 10^{-4} N (see Fig. 4.7 for example). In other words, if the surface friction linked to η_S applied on the rings, those latter would never rise up in the film, or would exhibit rises which would be much more smaller and slow than the ones evidenced in our experiments.

The explanation of this paradox comes from the experimental procedure we used to prepare our soap solution. As explained in Chapter 1, this latter must be mixed during several hours in order for the film to present the wanted characteristics, i.e. mobile interfaces and homogeneous fringe patterns along the horizontal direction. If this procedure is not applied to the solution, soap films with very viscous interfaces in the bottom regions, and mobile interfaces at the top are obtained. Figure 4.23 illustrates the typical aspects of the film obtained with and without mixing.

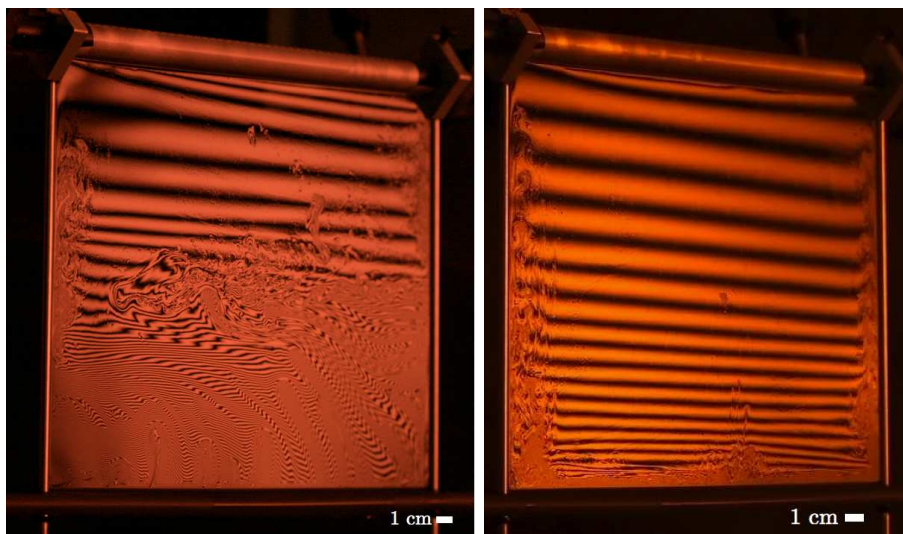


Figure 4.23: Pictures of vertical soap films obtained with our non mixed (left) and mixed SLES+CAPB solution (right).

These inhomogeneities reflect strong surface viscosity gradients for the film interfaces along H . We experienced the effects of those gradients by plugging our rings

in films such as presented in Figure 4.23 left. The result was that no ascending motion was observed in that viscous area, as a consequence of the large value of η_S .

The fact that the rings exhibit rises in all the experiment presented in this chapter implies that our experimental procedure (i.e. the mixing of the solution) strongly decreases the surface viscosity of the SLES+CAPB interfaces. Indeed, the absence of the interfacial drag defined by Eq.(4.25) in our model implies that this latter order of magnitude is at most comparable to the one of the in-bulk drag, say 10^{-5} N (see Fig. 4.13 for example). Introducing this order of magnitude in Eq.(4.25) brings that the surface viscosity linked to our film interfaces is of the order of 10^{-6} Pa · s · m at most, which is the order of magnitude of the surface viscosity of a SDS interface (see Chapter 1 and sett, barentin for example). This estimation reveals that the surface viscosity of our mixed solution is at least three order of magnitudes smaller than the one of the non-mixed solution as measured by Scheid and coworkers [36]. This estimation is consistent with both the absence of interfacial friction in our model and the mobile nature of our film interfaces. The difference between the mixed and non-mixed solution surface viscosities must be regarded as a particular behavior of the surfactant, induced by the mixing. To conclude this discussion, let us mention that further insights on the behavior of the SLES+CAPB mixture could be obtained by coupling surface viscosity measurements to scattering experiments (X-rays or neutrons [18]) in function of the mixing time.

4.7 Conclusion

In this Chapter, we have investigated the behaviors of hair rings plugged in vertical fed soap films. We have shown that those rings are submitted to the adapted so-called 2-D buoyancy linked to the interfacial nature of soap films. We have shown how it is possible to express this buoyancy in terms of the surface tension forces in the particular case of vertical soap films, enhancing the knowledge of the nature of the buoyant forces in those systems. Dynamical considerations about the rises of the rings in the films have revealed that both friction and lubrication forces are implied in their rising motion. Tests of dynamical models coupled to experimental observations have revealed that a liquid front develops before the rings and moves up with the rings, modifying the total mass to be taken into account to describe their ascents. We have shown that it is possible to model the behavior of this total mass as a function of the different experimental parameters. In the end, the coupling between the effective mass and the dynamical model have brought quantitative agreements between experimental and numerical data, underlying their relevancy to predict the behaviors of buoyant rings in vertical soap films.

Chapter 5

Thermal plumes in vertical soap films

We underlined in Chapter 1 that previous experiments have focused on thermal constraints in soap films. These studies revealed a turbulent behavior of the thickness, velocity and temperature fields of heated films [55–57]. In the particular case of vertical temperature gradients, the apparition of thermal plumes rising from the hot points to the upper regions of the films has been evidenced [57]. This chapter is devoted to the experimental study of those plumes, produced in our vertical fed soap films. We first describe how we generate single thermal plumes. We then explain how the infrared camera used in Chapter 2 for the film thickness measurements has been used to visualize those plumes. At the end of the chapter, we propose a model for predicting the characteristics of the plumes as a function of the applied temperature difference ΔT and of the feeding flow rate Q .

5.1 Thermal plumes

Let a tank be filled with water. We imagine that this tank is provided with a heating device allowing to apply a located heating at the bottom. The temperature difference between the water and the heating point is noted ΔT , and can be varied continuously from 0 to a maximum value ΔT_{max} fixed by the setup. Various behaviors can be observed following the magnitude of ΔT . Very weak heatings ($\Delta T < 1^\circ\text{C}$) lead to diffusive behaviors of the temperature field in the vicinity of the heating point [2, 112]. Extreme regimes ($\Delta T \geq 100^\circ\text{C}$) bring the water of the tank to the boiling state, characterized by a phase transition from the liquid to the gaseous state of water [2, 112]. For intermediate heatings values, the upward convective flow adopts a plume shape, such as the one represented in Figure 5.1 (extracted from [111]) [55–57, 108, 111–115]. Those plumes are characterized by a

typical mushroom shape. As shown in Figure 5.1, the mushroom head presents swirling fluid motions. These swirls come from the shear stresses between the ascending liquid and the fluid at rest in the vessel [113]. Plumes can either be created by temperature gradients or by chemical reactions, or both. The pictures of Figure 5.1 correspond to an autocatalytic reaction front : ascending from the bottom to the top of the tank and due to the local density gradients generated by the chemical reaction [111]. Plumes are also involved in larger fluid systems such as the Earth mantel [114, 115]. The temperature differences between the core of the Earth and its surface are supposed to be at the origin of large scale plumes in the mantel's magma [115]. Once those plumes reach the surface, they lead to the apparition of considerable constraints on the crustal. This theory, known as the “hot spot theory”, has been proposed in order to justify crustal phenomena such as the tectonic plate motions. From a theoretical point of view, plumes have been successfully modeled thanks to the classical convection equations [116].

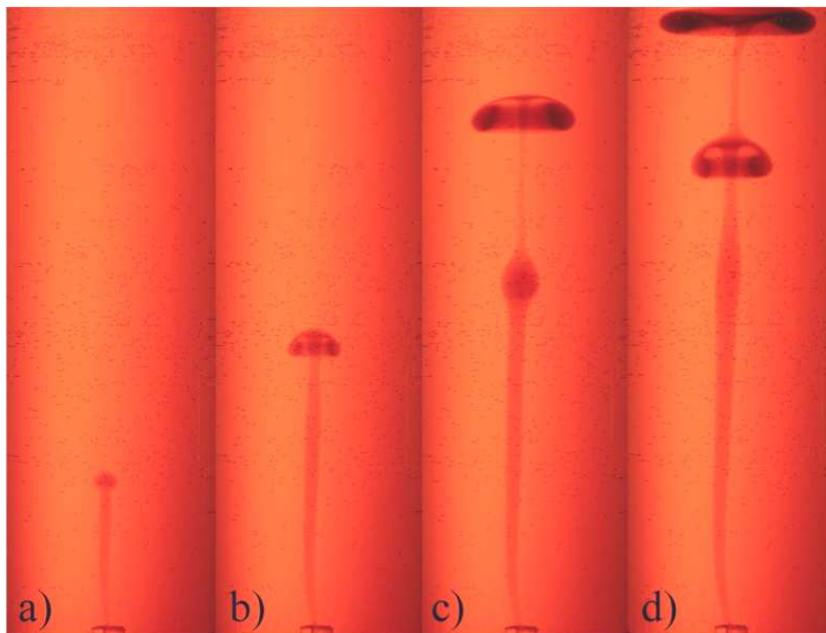


Figure 5.1: Successive images of an ascending plumes obtained from an autocatalytic reaction described in [111].

5.1.1 Thermal plumes in vertical soap films

As mentioned in Chapter 1, the thermal convection experiments performed with vertical soap films as nearly bi-dimensional Rayleigh-Bénard cells have been essentially realized for the needs of thermal turbulence theories [55–57]. Those experi-

ments have shown that thermal plumes intensively develop in the so-constrained films, leading to turbulent behaviors of thickness, velocity and temperature fields. Figure 5.2 is extracted from [55] and illustrates two shadowgraphs of such thermally constrained films.

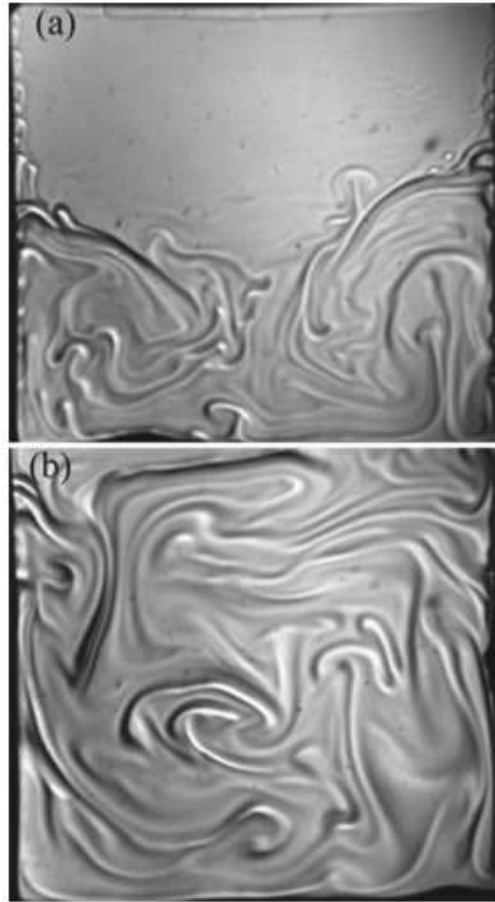


FIG. 2. Shadowgraphs of thermal convection patterns in soap films. The pictures were taken by a CCD camera with the shutter speed set at $1/1000$ s. The height and the width of the film were, respectively, 2 by 2 cm. The temperature differences are $\Delta T=31$ °C for (a) and $\Delta T=62$ °C for (b). In both cases, thermal plumes of various sizes are clearly observed. However, for the low temperature gradient case (a), the plumes can only climb half way up the film, leaving the top half essentially quiescent. One can occasionally observe, as seen in (a) that a small plume ascends from the lower mixing region into the upper quiescent region. This type of plume is not as energetic as the ones directly ejected from the bottom of the cell. In the presence of the large temperature gradient (b), the plumes can readily reach to the top of the film, causing vigorous mixing throughout the entire cell.

Figure 5.2: Shadowgraphs of heated soap films from [55].

Even if most of the experiments aiming to apply thermal constraints on vertical soap films have evidenced the presence of those plumes, they have not been considered as physical objects, so that precise understandings of their behaviors are nowadays lacking.

The pictures presented in Figure 5.2 suggest that a heating applied on the whole width of the film tends to generate plumes which can mix and interact with each others. As realized in the three-dimensional cases (e.g. [111]), we wished to investigate the behaviors of isolated thermal plumes in our fed soap films. The purpose of our experiments was to underline the influence of ΔT and Q on the plumes produced in soap films, keeping in mind that buoyancy exists in this nearly bi-dimensional system but not exclusively in the usual volume aspect.

5.2 Single thermal plumes in soap films

5.2.1 Experimental setup

In a purpose of studying the behaviors of the thermal plumes produced in our soap films as functions of ΔT and Q magnitudes, we have designed an experiment which allows to apply a local heating to the film on a spatial extend which is less than the width of the film. This situation is quite different from the classical Rayleigh-Bénard-like cases where the heat source extends all over the width of the setup. This configuration enables to focus on isolated thermal plumes, as physical objects, and independently of collective effects as presented in Figure 5.2. The setup used to produce and feed vertical films is the same as the one presented in the previous chapters (see Fig. 2.4).

The thermal constraint can be applied by any heating device provided it is possible to plug it in the film (electric resistors, soldering iron...). For example, one can introduce an electric resistor in the film and then inject a current to produce a local Joule effect. Although easy to realize, this method does not allow an accurate control of ΔT . Calibrated thermal resistors exist, but we experimented that they were not suited to realize our experiments. Indeed due to their sizes and wetting properties, it was almost impossible to plug them in the film without breaking it. We chose to use a hollow stainless steel pipe which goes through the film interfaces. Within this pipe, we impose a flow of thermalized water (see Figure 5.3). By controlling both the water temperature in the pipe and the temperature of the feeding solution, we control the magnitude of ΔT . We have performed series of tests with infrared imaging (see below), and have seen that the temperature of the metal constituting the pipe rapidly saturates once the thermalized flow is established (typically a few seconds). This implies that thermal inertia do not have to be taken into account in ΔT determinations. The distance between the bottom edge of the frame and the heating pipe is fixed to 20 mm for all the experiments.

The radius of the pipe is fixed to 6.35 mm, and its thickness is 2 mm. The ΔT values range in $[0, 40]^\circ\text{C}$. This range is fixed by the ability of our films to resist to the applied thermal constraint during a long time (several minutes) without bursting. In the following reported experiments, we mainly consider temperature differences of 14.1, 21.4, 27.3 and 36.8°C . Those values are arbitrarily chosen as representative with respect to the plume behaviors in our films.

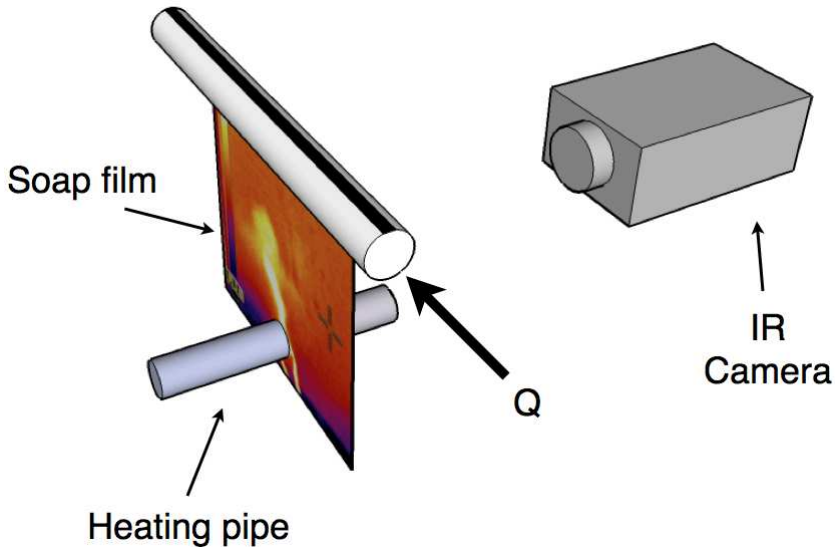


Figure 5.3: Sketch of the experimental setup used to apply thermal constraints to fed soap films.

The infrared camera used in Chapter 2 to measure the thickness of the films was used for imaging the thermal plumes produced by the heating. It can be determined that the thermal emissivity of thin water sheets is of the order of 96 % [81]. Nevertheless, it is rather difficult to visualize the plumes with the infrared camera : the infrared radiations emitted by the film surroundings are close in wavelength and higher in intensity than the one emitted by the plumes. This weak intensity is due to the fact that the film is very thin, what limits its emissive capacities. However (and hopefully), if a thermal contrast is created between the film and its surroundings, plumes should be easily imaged by the camera. We then designed a setup as schematized in Figure 5.4. The expected infrared contrast was created by putting a tank behind the film, exactly as presented in Chapter 2 for thickness measurements (see Fig. 2.9). The difference with the thickness measurement setup is that the water in the tank was cooled rather than being heated. Since the typical temperatures of the film and the heating pipe are of the order of 10°C , it is necessary to cool down the tank to temperatures below 0°C . This was achieved by filling the tank with a water, ice and salt mixture.

The amount of ice and salt was chosen so that the typical temperature of the tank stays close to -10°C . The temperature range displayed by the camera was then chosen so that the background temperature was out of range. Doing so, the plumes appear on infrared images as presented in Figure 5.5. This Figure shows a typical plume obtained for $\Delta T \sim 20^{\circ}\text{C}$ and $Q = 2\text{ml/min}$, several minutes after the heating was started. The global mushroom shape characterizing the plumes is reminiscent of the classical three-dimensional case (see Fig. 5.1). The typical spatial resolution obtained with this setup is 10^{-4} m . Infrared images are acquired with a frequency of 25 Hz, fixed by the infrared camera.

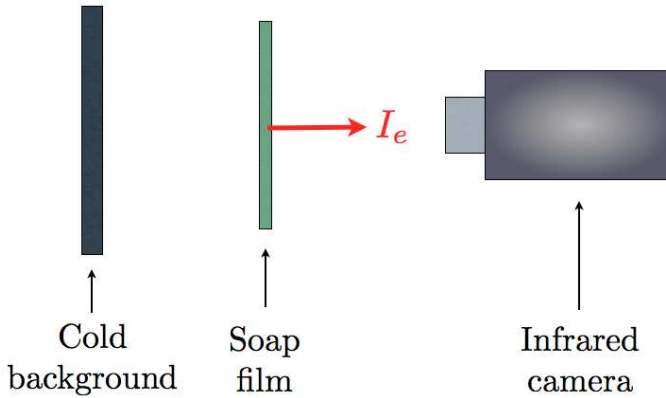


Figure 5.4: Schematics of the experimental setup used to visualize thermal plumes produced in soap films (not to scale). I_e represents the infrared intensity emitted by the film itself. Cooling the background allows to modify its emitted intensity range, creating thermal contrast between the film and its background.

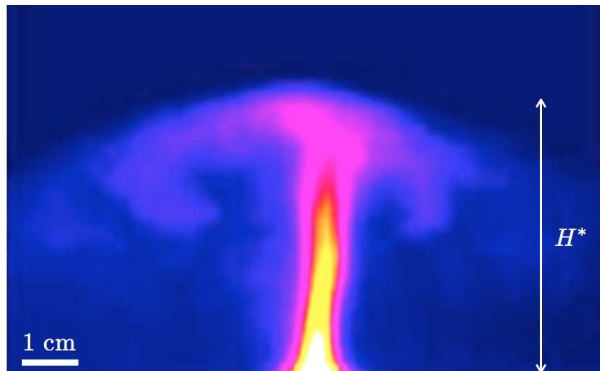


Figure 5.5: Typical infrared image of a thermal plume in fed soap film for $\Delta T \sim 20^{\circ}\text{C}$ and $Q = 2\text{ ml/min}$.

Figure 5.6 shows several images obtained by the camera right after the heating was started. These images reveal that the heating is followed by the growth of a thermal plume, starting from the heating pipe to the upper regions of the film. This growing regime is followed by a saturation of the size of the plume to an equilibrium value H^* , represented in Figure 5.5. This behavior is almost similar to the three-dimensional case such as presented in Figure 5.1, the main difference being that the growth stops before the plume has reached the top of the film. This saturation was observed in every experiment, whatever the values of ΔT and Q . Note that similar behaviors have been evidenced in Rayleigh-Bénard-like previous experiments (see Fig. 5.2, top and [57]).

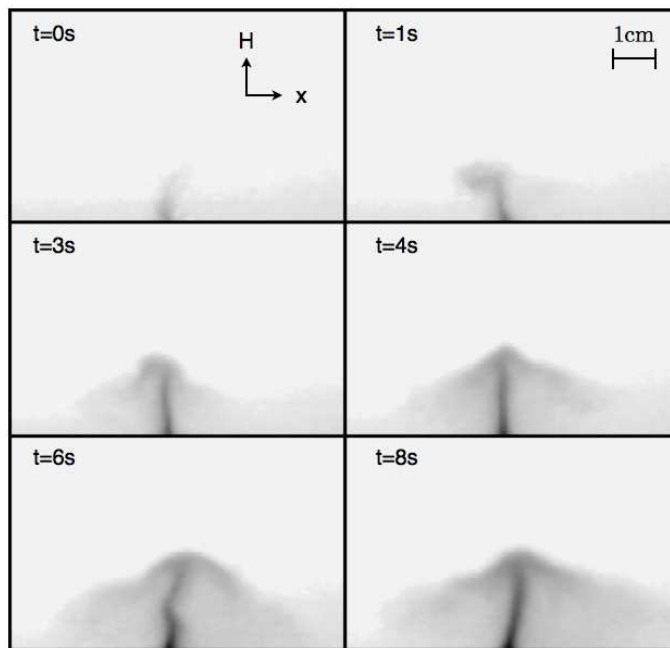


Figure 5.6: Successive images of the plumes during their growth. The temperature difference is fixed to $\Delta T = 23^\circ\text{C}$ and the feeding flux is fixed to $Q = 1.9 \text{ ml/min}$.

Images such as the ones presented in Figure 5.6 have been used to obtain the plume trajectories. We considered spatio-temporal diagrams such as the one presented in Figure 5.7. These diagrams are obtained by considering the infrared intensity right above the heating pipe along a vertical line of pixels. The corresponding image are then thresholded (Fig. 5.7, right) and processed thanks to home made image analysis routines. Figure 5.8 represents typical $H(t)$ curves for three different temperatures and a fixed Q . After their growth, the size of the plumes saturates but still fluctuates. The curves $H(t)$ oscillate around the equilibrium value H^* characterizing the global size of the plume after growth (see

Fig. 5.5). This behavior is analogous to those of the floating rings described in Chapter 4, except that the oscillations occurring after the growth are not damped and hold as long as the film “lives”. This analogy with the case of the floating rings suggests that those objects should share similar driving and damping effects (i.e. buoyancy and viscous drag). We will come back to this analogy in the next sections.

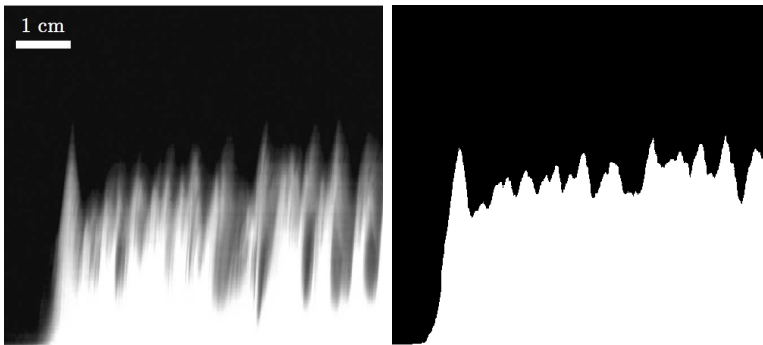


Figure 5.7: Left : Typical spatio-temporal diagram for a plume growth. Right : the same diagram after threshold, as used for experimental determination of the plume trajectories. Those images were obtained for $\Delta T = 18^\circ\text{C}$ and $Q = 1.8$ ml/min.

Figure 5.9 represents the aspect ratio of the plumes (i.e. the mean equilibrium height after growth H^* normalized by the height of the film L) as a function of ΔT for several values of the feeding flux Q . The H^* values are obtained by fitting a constant value on the different $H(t)$ curves once the growth of the plume is finished. The curves in Figure 5.9 show that H^* tend to increase with increasing ΔT . This feature can be understood by recalling the thermal dependency of the density of fluids versus temperature. This density is supposed to evolve with temperature as :

$$\rho(T) = \rho(T_0)(1 - \alpha(T - T_0)), \quad (5.1)$$

where T_0 is the temperature taken as the reference for the considered case and α is the dilatational coefficient of the material at T_0 [2,112]. As presented in Chapter 4, density fluctuations generate buoyant forces on fluid particles, the buoyancy force being proportional to the density difference. The density fluctuations resulting from the heating can thus be expressed from Eq.(5.1) as :

$$\Delta\rho = \rho(T_0)\alpha\Delta T, \quad (5.2)$$

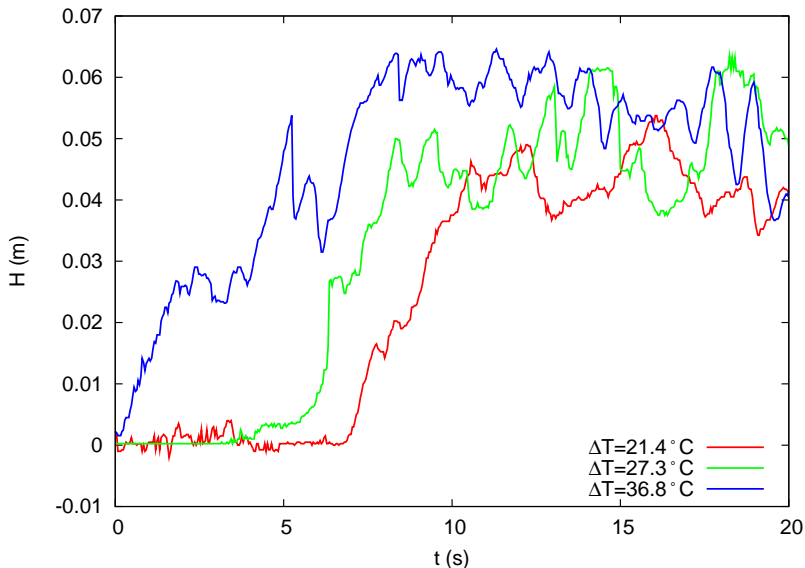


Figure 5.8: Examples of plume trajectories during their growth. The feeding flux is fixed to $Q = 1.7$ ml/min.

where $\Delta T = T - T_0$. Since Eq.(5.2) is a growing function of ΔT , the buoyant force acting on the heated particles increases with ΔT as well. It is then logical for the plumes to grow further if ΔT is increased.

On the other hand, H^* decreases with Q , what is the opposite behavior to the floating rings. This can be explained as follows. The heating pipe is linked to the film through a meniscus, meaning that any particle rising from this pipe toward the film is a regenerated particle. As discussed in Chapter 1, this implies that the particle thickness is smaller than the thickness of its surroundings. We underlined in Chapter 4 that these thickness differences lead to upward motions of regenerated particles. As a consequence, the thermal plumes must be seen as a collection of film particles which have been regenerated and heated at the same time by the pipe. Both two and three dimensional buoyancies then act on those particles. The difference with the case of the floating rings is that these heated particles are not empty. For any Q value, the thickness difference is thus much more smaller for the heated particles than for the rings. This limits the efficiency of the thermally enhanced bi-dimensional buoyancy. Moreover, this latter is proportional to the radius of the particle (see Eq.(4.3)). Observations of regenerated film particles (see Fig. 4.2) suggest that this radius is of the order of 10^{-3} m at most. As a conclusion, the driving force acting on heated fluid particles is likely to be weaker than the same force considered for the case of the floating rings.

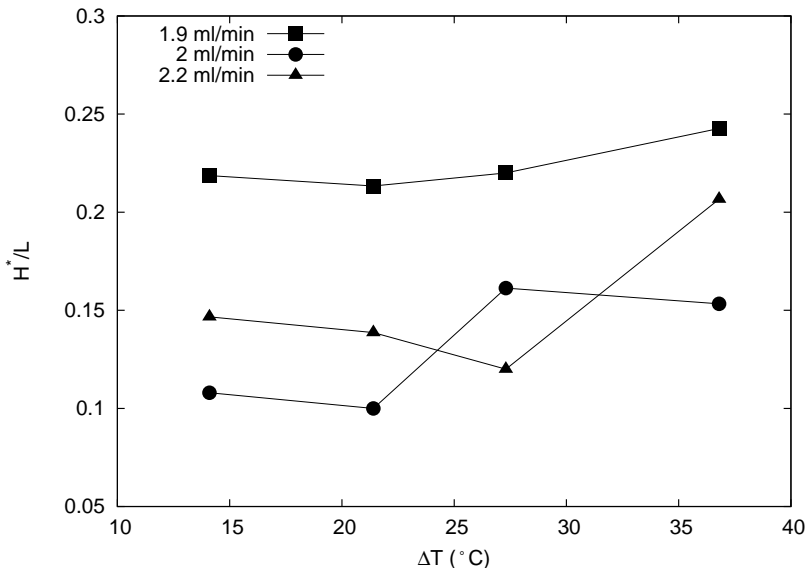


Figure 5.9: Aspect ratio H^*/L of the plumes versus ΔT for several Q values.

This weakness may lead to force balances which are so that the higher the flow, the lower the plumes are able to rise in the film.

The rather low values for the aspect ratios H^*/L of our plumes confirm the experimental observation that thermal plumes tend to be smaller than their containers in the particular case of soap films. Figure 5.9 also shows that the plume size does not exceed one quarter of the total size of the film, even with ΔT up to 40°C . It is possible to apply larger constraints to the films, but beyond $\Delta T \sim 50^\circ\text{C}$, the films may not be able to support the constraint and burst. Those particular results are valid for thermal plumes produced in fed soap films, i.e. which thickness profiles is stable in time and space. In fact, the bottom picture of Figure 5.2 shows that high thermal constraints (i.e. $\Delta T = 61^\circ\text{C}$) lead to plumes which can reach the top of the film. Those films are far way smaller than our fed soap film ($L \sim 1\text{ cm}$) and heated over their whole width, what may be less perturbative for the film than our local constraints.

5.2.2 Thermal rising criterion

Since H^* tends to decrease with increasing Q values at fixed ΔT implies that a critical temperature difference ΔT_c must exist in order for the plumes to develop in the film. We performed series of sweeps in ΔT , starting from 0, and evidenced ΔT_c for the different Q values involved in our experiments. Those values are plotted in Figure 5.10, showing that ΔT_c increases with Q , in agreement with

previous observations. A cross over occurs at Q rates higher than 2.2 ml/min. Observations show that inhomogeneities may appear in the downward flow, due to the gravitational streets discussed in Chapter 2. The downward drainage flow exhibits turbulent features in the presence of those streets, in which the thermal plumes hardly develop. The greyed area of Figure 5.10 indicates the limit of the laminar Q range in which our models are valid (see next section for details). Note that similar temperature thresholds behaviors have been evidenced in Rayleigh-Bénard-like works, both experimentally and theoretically [57].

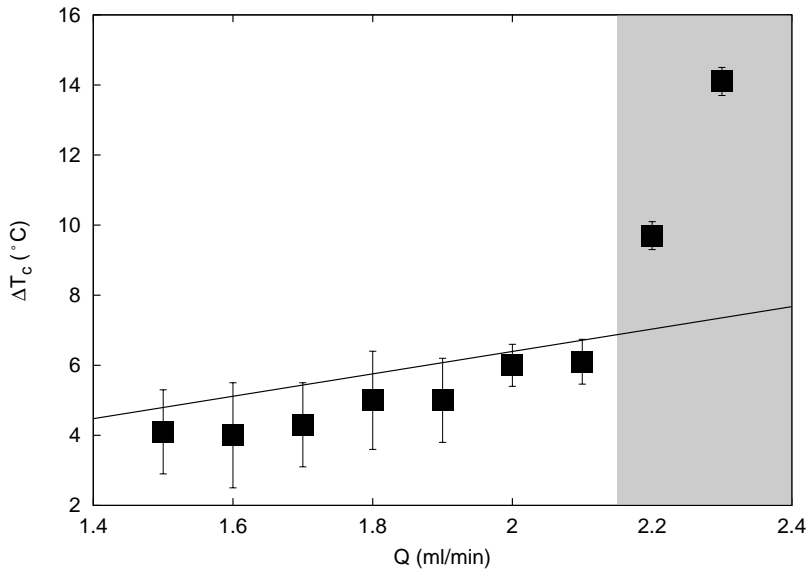


Figure 5.10: Critical temperature difference ΔT_c versus the feeding flux Q . The dots are experimental data while the solid line corresponds to the theoretical modeling (see next section for details). The greyed area corresponds to Q values for which inhomogeneities may appear in the downward flow.

5.3 Dynamics of thermal plumes in soap films

Similarly to the dynamical study made about rising rings in Chapter 4, we will now focus on the dynamics linked to the growth of the thermal plumes. To do so, we will consider the motion of a single film particle, which receives heat from the heating pipe. Due to the bi-dimensional nature of soap films, interfacial phenomena will be taken into account in order to describe the total driving force acting on this hot particle. The characteristics of the heated particles trajectories will then be compared to the growth of the plumes as represented in Figure 5.8, to ensure of the efficiency of our model.

5.3.1 Marangoni effect

Since the film interfaces are submitted to a vertical temperature difference, one could expect the Marangoni effect to account in the the upward motion of the hot film particles. We applied thermal constraints to horizontal soap films for testing the efficiency of this effect. These latter were created by pulling a square frame out of our solution. This frame was then set so that the film is horizontal without feeding. This configuration ensures to suppress any buoyancy component (both two and three dimensional) from eventual flows occurring in the film. The only convective flow that can occur are Marangoni flows, similar to the ones obtained in the ground pepper experiments described in Chapter 1. Figure 5.11 shows successive images of such heated horizontal films, taken with the infrared camera. While filming those horizontal constrained films, no flow was observed, at least within the ΔT range involved in our experiments. This simple test allowed us to state that global Marangoni effects are inefficient to generate thermally-driven flows in our system.

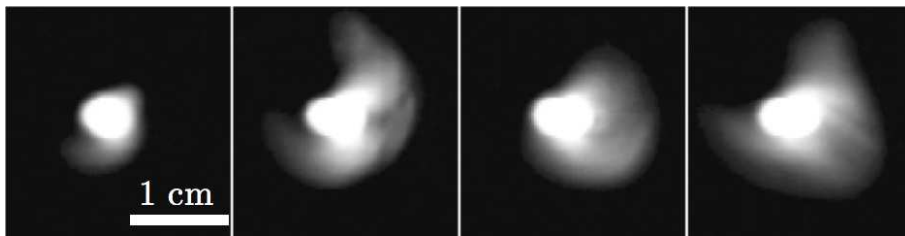


Figure 5.11: Successive images of an horizontal soap film during heating taken with the infrared camera ($\Delta T = 35^\circ\text{C}$).

5.3.2 Three-dimensional buoyancy

Since ΔT affects both the bulk and the interfaces of the film, the “usual” buoyancy should be taken into account. It is estimated as [2, 112] :

$$F_A \sim \rho\alpha\Delta Tg\Omega, \quad (5.3)$$

where ρ is the density of the solution, α the thermal dilatational coefficient and Ω the volume of a typical ascending particle. All those quantities are known, except Ω . Nevertheless, Ω can be removed by expressing the Newton’s law for a fluid particle of mass $\rho\Omega$. Let us assume that the particle moves from the pipe to a height H , within the typical time τ_A . The acceleration the particle experiences can then be approximated by H/τ_A^2 and the Newton’s law reads :

$$\rho\alpha\Delta Tg\Omega \sim \rho\Omega\frac{H}{\tau_A^2}. \quad (5.4)$$

This expression can be used to express τ_A as :

$$\tau_A = \sqrt{\frac{H}{\alpha\Delta Tg}}. \quad (5.5)$$

It is instructive to estimate the capillary time linked to Marangoni effect to compare its efficiency to the one of buoyancy. This time can be expressed as [1, 2] :

$$\tau_\gamma \sim \sqrt{\frac{\rho H^4}{\gamma e}}, \quad (5.6)$$

where γ and e are orders of magnitudes for the film surface tension and thickness, respectively. Introducing typical order of magnitude values for γ (10^{-2} N/m), e (10^{-5} m), α ($2.6 \cdot 10^{-4}$ °C $^{-1}$) and ΔT (1°C) allows to estimate that $\tau_A \sim 1$ s while $\tau_\gamma \sim 10^3$ s for $H \sim 10^{-2}$ m. Those values confirm that thermal buoyancy is more efficient to bring hot particles to the upper film regions than Marangoni effect.

5.3.3 Two-dimensional buoyancy

In addition to this in-bulk 3-D buoyancy, we have to consider the bi-dimensional buoyancy as well, as a consequence of the meniscus existence between the film and the heating pipe. As presented in Chapter 1, this meniscus produces regenerated buoyant particles, as a consequence of the marginal regeneration phenomenon. The film particles constituting the thermal plumes should then be considered as moved by both bi-dimensional and three-dimensional buoyant effects. As emphasized in Chapter 4, the bi-dimensional buoyancy can be expressed by considering the two-dimensional density ρ_2 . This force originates in the thickness difference existing between the buoyant particles and their surroundings [15, 107]. There could be some temptation to measure the thickness differences with the infrared camera as presented in Chapter 2, and then to deduce the bi-dimensional buoyant force from Eq.(4.3). Unfortunately, due to the temperature field associated to the thermal plumes, it is impossible to perform direct measurements of those thickness differences. Actually, the typical wavelengths emitted by the particles and used to perform thickness measurements are too close to each others. In other words, the temperature and the thickness fields are not discernible by the infrared camera while imaging thermal plumes in soap films.

Even if it is impossible to obtain an experimental characterization of the bi-dimensional buoyancy, it is possible to express it by the intermediate of the fluctuations of the bi-dimensional density ρ_2 . This is what is usually done in usual

formalizations of convection problems in soap films [55–57, 107]. Let us come back to the case of regenerated particles as presented in Chapter 1. Those particles exhibit a thickness difference with their surroundings, named de . This thickness difference originates in the extra coverage in surfactant molecules which characterizes the regenerated particles. As a consequence of this extra coverage, the interfaces of the regenerated particles exhibit a surface tension value which is smaller than the one of the unperturbed film interfaces. The regenerated particles should then somehow experience Marangoni stretchings from their surroundings. Those stretchings are responsible for both the thickness difference de and the increase of the area of the regenerated particles.

The variation of ρ_2 induced by local Marangoni stretchings can be expressed as [55, 57, 107] :

$$d\rho_2 = \rho_2 \alpha' de, \quad (5.7)$$

where α' is an effective expansion coefficient expressed as [57] :

$$\alpha' = \frac{1}{e(H=0)}, \quad (5.8)$$

where $e(H=0)$ is the thickness of the meniscus. From a phenomenological point of view, α' originates in the efficiency of the meniscus to produce regenerated particles. In addition to this usual origin for $d\rho_2$, we have to include the effects of ΔT , that is to say, considering a thermal origin for $d\rho_2$. This thermal origin can be justified by considering the capillary time related to a typical rising hot particle size. If the size of this latter is estimated by the resolution of the camera (10^{-4} m) one finds that $\tau_\gamma \sim 10^{-3}$ s. The weakness of this time traduces that regenerated particles are prone to be submitted to rather efficient Marangoni stretchings. The temperature difference applied to the film must then be considered as an extra contribution to the expand of regenerated particles, even for the weak ΔT considered in our experiments. We thus decided to express the ρ_2 variation of the heated particles as :

$$d\rho_2 = \rho_2 \alpha^* de, \quad (5.9)$$

with $\alpha^* = \alpha' \Delta T / \Delta T_c$. If ΔT is increased, $d\rho_2$ does so, what is consistent with typical behavior of density fluctuations with temperature. The linearity of Eq.(5.9) with ΔT is a kind of local linear approximation of a more general expression. This approximation is consistent with both facts that the ΔT range involved in our experiments is rather small and that surface tension (and so Marangoni stretching) varies smoothly with temperature.

5.3.4 Viscous drag

In opposition to the driving buoyancies, viscous friction forces act on the rising particles. As previously done in Chapter 4, it is possible to adapt the expression of the viscous drag on a surface S as defined by Eq.(4.11) to the particular case of heated particles. By analogy with the case of the floating rings, the surface on which the friction applies can be expressed as $S = \pi l e(H)$, with l the typical size of a heated particle. The velocity gradient dv/dz can be approximated by v/z , with v the relative velocity of the rising particle and z the extension of the gradient. Still by analogy with the case of the rings, z can be approximated by $e(H)$. The viscous drag acting on the heated particles eventually writes :

$$F_{drag} = \pi \eta l \left(\frac{Q}{e(H)L} + \frac{dH}{dt} \right). \quad (5.10)$$

Note that this equation is strictly the same as Eq.(4.12) for the particular case of the heated particles.

5.3.5 Dynamical model for the heated particles

Since all the forces acting on the heated particles can be expressed as functions of previously determined quantities, it is possible to write down a dynamical equation for the growth of the heated particles, under the classical form $ma = \Sigma F$. In the particular case of our heated particles, we have :

$$ma = \rho \Omega d^2 H / dt^2 = \Sigma F. \quad (5.11)$$

The volume Ω of the particle can be expressed as :

$$\Omega = \pi l^2 (e(H) - de(H)), \quad (5.12)$$

with clear notations. It is now interesting to develop the different forces acting on the heated particle for emphasizing the control parameters of the problem. If the three dimensional buoyancy was the only force to act on the particle, we would have :

$$\rho \Omega \frac{d^2 H}{dt^2} = \rho \Omega \alpha \Delta T g. \quad (5.13)$$

This expression reduces to $d^2 H / dt^2 = \alpha \Delta T g$, which is the usual acceleration produce by thermal buoyancy.

The same algebrae can be performed for the case of the bi-dimensional buoyancy. In this particular case, we have :

$$\rho_2 \Omega \frac{d^2 H}{dt^2} = \Delta \rho_2 \Omega g. \quad (5.14)$$

The ratio $\Delta\rho_2/\rho_2$ can be developed using Eq.(5.9), leading to :

$$\frac{d^2H}{dt^2} = \frac{1}{e_0} \frac{\Delta T}{\Delta T_c} de g, \quad (5.15)$$

where $e_0 = e(H = 0)$. Doing the same for the viscous drag gives :

$$\rho\Omega \frac{d^2H}{dt^2} = \pi\eta l \left(\frac{Q}{e(H)L} + \frac{dH}{dt} \right). \quad (5.16)$$

Using Eq.(5.12) as a definition of Ω , we obtain :

$$\frac{d^2H}{dt^2} = \frac{\nu}{l(e(H) - de(H))} \left(\frac{Q}{e(H)L} + \frac{dH}{dt} \right), \quad (5.17)$$

where ν is the kinematic viscosity of the solution, defined as $\nu = \eta/\rho$ [2]. The motion of the heated particles in our soap films should then be modeled by :

$$\frac{d^2H(t)}{dt^2} = g\Delta T \left(\alpha + \frac{de(H)}{e_0\Delta T_c} \right) - \frac{\nu}{l(e(H) - de(H))} \left(\frac{Q}{e(H)L} + \frac{dH}{dt} \right). \quad (5.18)$$

Logically, e_0 is taken as the capillary length to attest for the existence of a meniscus between the film and the heating pipe. Since $de(H)$ cannot be experimentally measured, we chose to express it as the derivative of the thickness profiles described by Eq.(2.7). This derivative describes the thickness gradient in the film. Even if generated by a specific phenomena, the thickness difference between the rising particles and their surroundings must somehow obey the general behavior of the film, what justifies our estimation for $de(H)$. The typical size of the particle can be estimated from images such as presented in Figure 4.2, since the mechanism generating the hot particles is similar to the one which creates regenerated particles. This Figure allows to estimate that l is close to $3 \cdot 10^{-4}$ m.

Equation (5.18) assumes that ΔT is constant during the whole rise of the particle. This assumption is consistent with the fact that thermal imaging of the plumes reveals that their intensity remains almost constant during this growth (see Figs. 5.5 and 5.6). In addition to this argument, the thermal diffusivities of air and water can be used to estimate the typical heat diffusion times by the solution and the ambient air. Using $\kappa_{air} = 1.4 \cdot 10^{-7}$ m²/s and $\kappa_{film} = 2 \cdot 10^{-5}$ m²/s, it is possible to determine the diffusion times in the air and in the film. If one considers a thermal plume of size $H^* \sim 10^{-2}$ m, it comes :

$$\tau_{\kappa_{film}} \sim \frac{H^{*2}}{\kappa_{film}} \sim 10^5 \text{ s} \quad \text{and} \quad \tau_{\kappa_{air}} \sim \frac{H^{*2}}{\kappa_{air}} \sim 10^3 \text{ s}. \quad (5.19)$$

Those times are several order of magnitude larger than the typical rising time, this latter being thus of the order of 1 s. Thermal losses are then negligible during the particle ascension.

5.3.6 Dimensional estimations

At first, dimensional calculations can be performed on Eq.(5.18) in order to check its relevancy. The particle acceleration can be approximated as H/τ^2 and the rising velocity by H/τ . The time τ is the typical rising time as estimated from experiments. Introducing typical order of magnitude values in Eq.(5.18) brings $H^* \sim 10^{-2}$ m, which is consistent with experimental observations.

The critical temperature ΔT_c in order to obtain rising plumes in the films can also be estimated from Eq.(5.18). At $t = 0$ s, the speed of the particle is null, whereas its acceleration results from a balance between viscous friction and driving forces at position $H = 0$. Since no rise has occurred yet, no thickness difference has been experienced by the particle, so that $de(H = 0) = 0$. Thus, ΔT_c can be written as :

$$\Delta T_c = \left(\frac{\nu Q}{lLe_0^2} + \frac{H}{\tau^2} \right) \frac{1}{g\alpha}, \quad (5.20)$$

where Q is the downward drainage flow. Introducing order of magnitude values in this expression brings that $\Delta T_c \sim 1^\circ\text{C}$, in good agreement with experimental results (see Fig. 5.10). Eq.(5.20) exhibits a linear dependency versus Q , which is represented by the solid line in Figure 5.10. A quantitative agreement is noted between the experimental data and the predicted values. Since Eq.(5.18) implicitly assumes that flows in soap films are laminar, Eq.(5.20) only brings faithful prediction for ΔT_c values measured with laminar flows ($Q < 2.2$ ml/min). This result is in agreement with more formal descriptions of convection experiments in soap films [57].

5.3.7 Thermal plume trajectories

A numerical solving of Eq.(5.18) thanks to a Runge-Kutta method can be performed, since all the relevant quantities involved in are known from experiments or relevant estimations. Figure 5.12 shows typical theoretical curves superposed to the corresponding experimental data. The flux Q has been fixed to 1.8 ml/min for these curves. Many comments could be made about those curves. First, Figure 5.12 shows that the typical rising timescale is well reproduced by the model. However, one notices that experimental and theoretical trajectories are rather different during the growth, the experimental ones being first convex and then concave (see also Fig. 5.8), and the numerical ones being exclusively concave. This difference between both can be justified by the fact that a threshold is realized on the spatio-temporal diagrams (see Figure 5.7). Such image analysis operations are subjective by nature, what limits the precision of the experimental trajectories. Nevertheless, the fact that both experimental and theoretical rising

times are in agreement must be regarded as a sign of validity of our model.

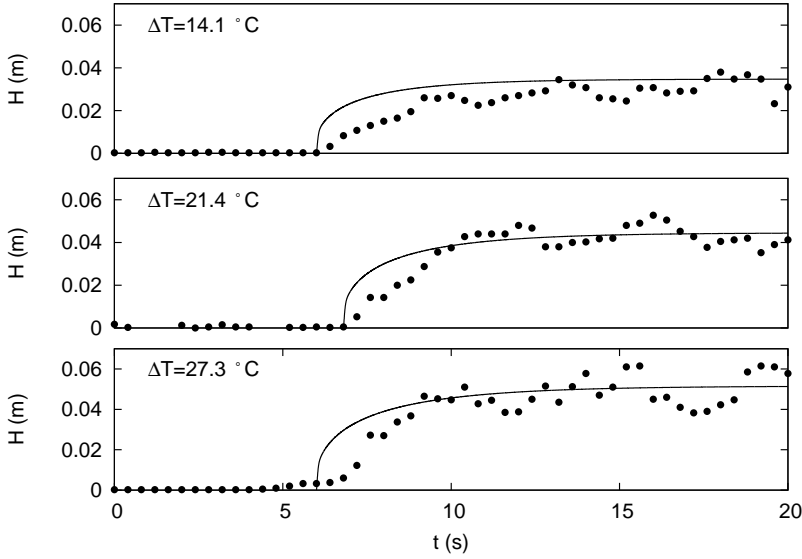


Figure 5.12: Comparison between experimental and theoretical $H(t)$ for several temperatures and Q fixed to 1.8 ml/min. The time origins, defined as the beginning of the rises, have been shifted for visibility.

A second feature which is well predicted by the model is the H^* value as a function of the experimental parameters. Beside this, the model fails to reproduce the oscillations of $H(t)$ around H^* after growth. We showed in Chapter 4 that the oscillations of the rings originate in the viscous drag, due to the changes in sign it exhibits during the growth. Figure 5.13 presents the evolutions of the different terms of Eq.(5.18) during the plume growth. In opposition to the case of the floating rings, the viscous drag acting on heated particles does not exhibit any change in sign, what explains the absence of oscillations in the numerical $H(t)$. Note that no damping oscillations could be produced in theoretical trajectories, as it was the case for rings. This effect as to be regarded as the result of a balance between buoyancy and friction, which is such that friction forces cannot develop their oscillatory character on the particle trajectories.

This oscillatory regime should then be seen as being a different one from the rise. As explained previously, the size of the thermal plumes results from a balance between friction and buoyant forces. Once the plume is fully developed, the driving and damping forces are prone to present fluctuations (coming from local fluctuations of Q and ΔT) which are not taken into account in our model for the rise. In addition, we have to mention that fully developed plumes are formed of a

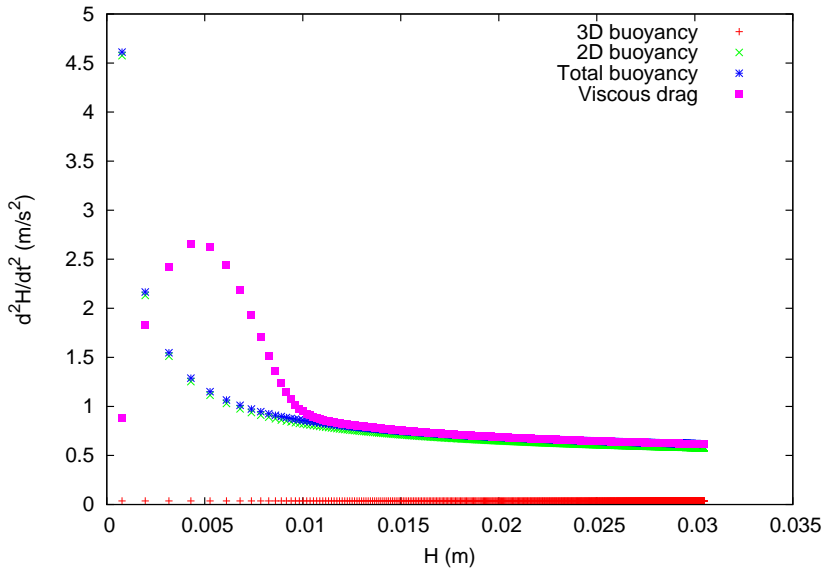


Figure 5.13: Evolution of the different terms of Eq.(5.18) versus H , for $\Delta T = 14.1^\circ\text{C}$ and $Q = 1.8$ ml/min.

bunch of rising particles. Their global dynamics should then result from the collective motion of their constitutive heated particles. Since our model is built for a single heated particle, it is somehow logical that oscillations are not reproduced. Though interesting, those oscillations are not further discussed here and are left as the subject of future investigations.

From Figure 5.13, it is clear that the three-dimensional buoyancy influence on the heated particle motion is quite weak with respect to its bi-dimensional analog. This fact underlines the preponderant role of interfacial phenomena in soap films. The weak efficiency of the three-dimensional buoyancy can be interpreted by evoking this interfacial nature. In three dimension, the heating causes density fluctuations. From a phenomenological point of view, those fluctuations represent a spreading of heated fluid particles with respect to the non-heated particles. In three dimensions, the heated particles are likely to spread in every directions, leading to the apparition of buoyant spheres of fluid within a fluid. In the case of soap films, this spreading is fairly reduced due to the weakness of the thickness of the films. This reduction is even further applied by the thickness diminution due to the regeneration.

The numerical computation of Eq.(5.18) allows to obtain further informations on the forces acting on the particles and their dependency on the Q and ΔT values. In a first time, Q can be fixed and ΔT varied. This gives the curves presented

in Figure 5.14 and Figure 5.15. Those curves have been built for $Q = 2$ ml/min. Figure 5.14 represents both buoyancy forces versus H for different ΔT values. As this latter increases, both forces increase as well. This is justified by the dependency of Eq.(5.3) and Eq.(5.9) on ΔT . These curves also show that increasing ΔT leads to larger values for the bi-dimensional buoyancy then for the three-dimensional one, in agreement with the preponderant role played by interfacial phenomena. These increases are in agreement with results of Figures 5.8, 5.9 and 5.12.

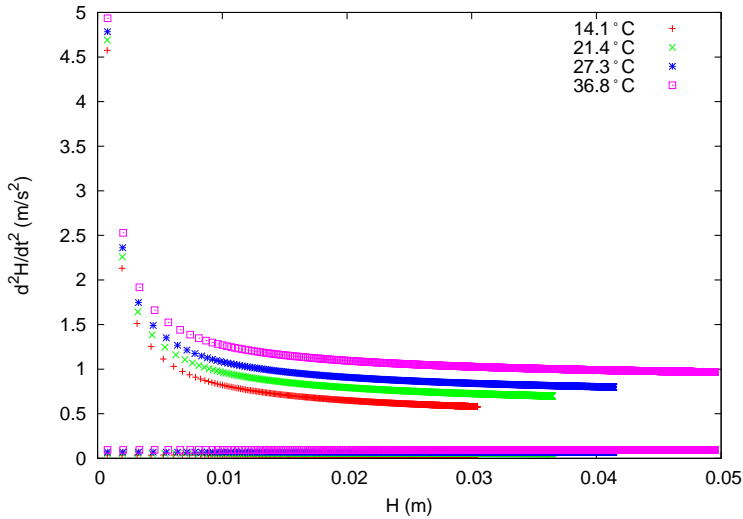


Figure 5.14: Buoyancy forces acting on the heated particles for different temperatures. The flow value has been fixed to 2ml/min.

Figure 5.15 illustrates the corresponding drag forces. These latter increase as well with ΔT . This can be explained by the fact that as the corresponding driving forces increase as well, the velocity of the heated particle must somehow increase with ΔT . This increase in velocity then leads to an increase of the viscous drag (see Eq.(5.10)).

It is also possible to fix ΔT to investigate the changing magnitude of those forces with Q . Numerical results are presented in Figure 5.16. Those curves has been computed for $\Delta T = 27.3^\circ\text{C}$. One can see that the higher the flow, the lower the buoyancy. This is a consequence of the dependency of ΔT_c on Q . As Q is increased, ΔT_c is increased as well (see Eq.(5.20) and Figure 5.10). This growth of ΔT_c tends to decrease the bi-dimensional buoyancy (see Eq.(5.9)). The corresponding drag forces decrease as well with increasing Q , and the explanation is

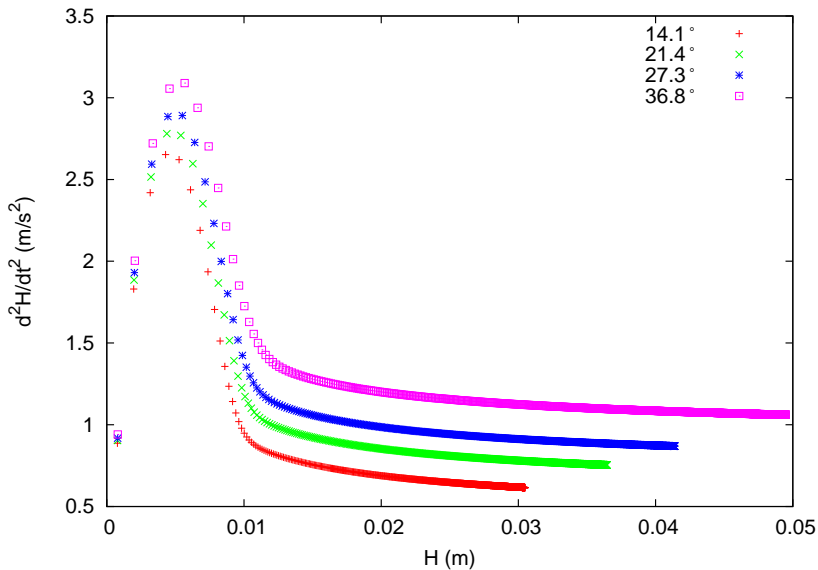


Figure 5.15: Viscous drags acting on the heated particles for different temperatures. The flow value has been fixed to 2ml/min.

exactly the same as discussed for the temperature dependency. Note that these dependencies versus Q are in good quantitative agreement with the dependency of the aspect ratio of the plumes versus Q , as presented in Figure 5.9.

These analyses performed in terms of force dependencies versus Q and ΔT confirm the validity of our theoretical model for the growth of the heated film particles in our fed soap films.

5.3.8 Comparison with the floating rings

In Chapter 4, we proposed a model which describes the rise of rings plugged in vertical fed soap films. Analyses of the different forces acting on the rings revealed that the friction forces are responsible for the damping oscillations for intermediate and small (Q, R) values, and that lubrication forces only account for a weak contribution to the equilibrium height reached by the rings H^* . The case of heated particles slightly differs from the previous one in several points. First, no lubrication forces were taken into account in the rising dynamics of heated particles. This is justified by the fact that no perturbative objects are introduced in the film in the present case : the heated particles do not have to swerve the film interfaces from each other to rise up. Another way to emphasize the absence of swerving is that there is no triple line linking the heated particle to the film,

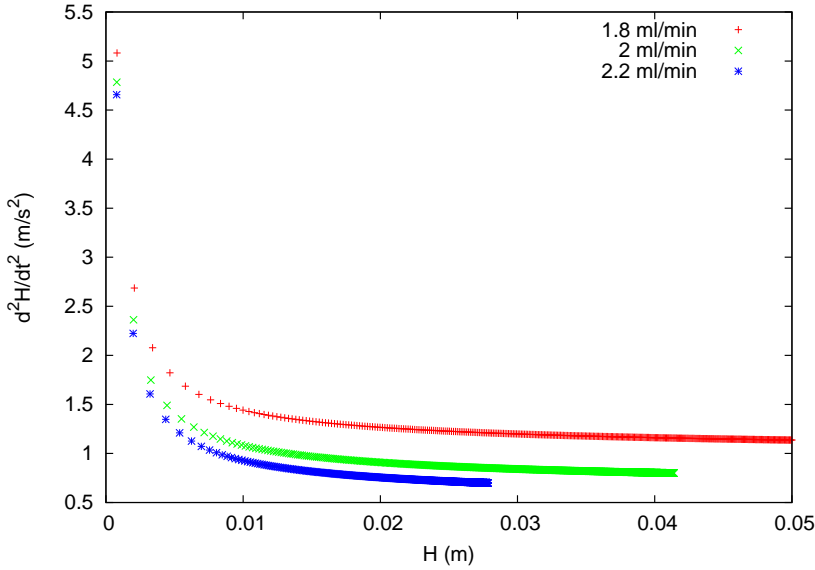


Figure 5.16: Bi-dimensional buoyancy force acting on the heated particles for different Q values. The temperature difference has been fixed to 27.3°C .

while there is one in the case of the rings. Figure 5.17 is a scheme of a transverse cut of a hot rising particle. The rising particle can be considered as composed of the dark grayed area shown in Figure 5.17. It is composed of a central part, representing the thickness difference de between the particle and its surroundings, and two linking parts ensuring the junction of the particle with the rest of the film. The difference with the floating rings is that the thickness variation is continuous between the particle and its surroundings, so that the linking parts adapt their shape to the de value at the considered H . This adaptation is rather different from the case of the meniscus displacement for the floating rings, in the sense that the continuous character of the thickness involves no film interface swerve.

The second major difference comes from the fact that the masses of the heated particles have not been evaluated here. The reason is that the thickness and the size of the heated particles have been estimated from known measurements. As emphasized previously, the thickness of hot particles cannot be measured with our setup, for infrared contrast reasons. Eq.(5.18) sums the accelerations imposed by the different forces acting on the particles. This relationship results from the mathematical simplification of the mass between the different terms so that the mass is no more needed to describe the dynamics of the heated particles. Nevertheless, their knowledge would have allowed to realize further tests about the relevancy of Eqs.(4.3) and (4.5) to describe the bi-dimensional buoyancy in soap films.

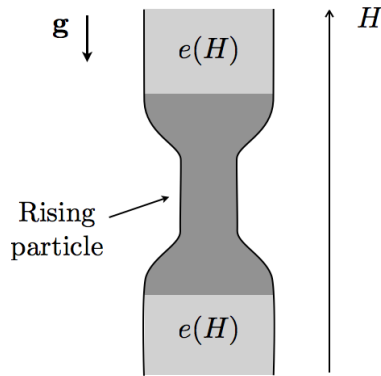


Figure 5.17: Transverse cut of a heated particle rising in the film (not to scale).

To conclude this comparison, let us mention that the interfacial viscosity has not been taken into account in the modeling of the hot particle rise. This discussion on this quantity is exactly the same as the one made for the case of the rings (see Chapter 4), since the friction forces are obtained from Eq.(4.11) in both cases.

5.4 Conclusion

In this chapter, we have studied the rising dynamics of thermal plumes in vertical fed soap films. Local heating have been shown as efficient for producing single thermal plumes in those films. A suited experimental configuration allowed us to image the rise and growth of the thermal plumes thanks to an infrared camera. The recorded images showed that the heating is followed by a rapid growth, which is followed by an oscillatory regime around an equilibrium size of the plumes. This equilibrium size depends on both the magnitude of the injected flow Q and the applied temperature difference ΔT . In order to predict the rising dynamics of the thermal plumes, Newton's equations were written and numerically solved. In addition to the usual buoyancy, bi-dimensional buoyancy, based on the thickness differences between the particles and their surroundings, have been adapted in order to account for the temperature dependence of the thickness differences. To oppose the hot particle rise, friction forces have been introduced. Order of magnitude calculations performed on this model are in good agreement with the typical experimental values, especially for the equilibrium height H^* of the plumes after growth. The critical temperature difference ΔT_c to be reached in order for thermal plumes to exist in the soap films is also successfully modeled, as a function of Q . Finally, a numerical resolution of our model brought that typical rising times and equilibrium heights are quantitatively predicted, as well as their dependency on Q and ΔT .

Conclusion and perspectives

This last chapter briefly summarizes the main results brought by our works, chapters after chapters. Perspectives are finally proposed.

Conclusions

In the first chapter, we proposed a brief state of the art concerning soaps, surfactant monolayers and basic soap film phenomenology. We presented the basic quantities used to characterize those monolayers : surface coverage, surface tension, elasticity and viscosity. We underlined that those quantities strongly depend on the experimental conditions, through the highly sensitive and complex chemical equilibria between the surfactant molecules in the bulk and at the interface. Those equilibria depend on numerous parameters such as the temperature, the bulk concentration in surfactant, the PH... We also underlined that organized structures such as micelles influence these interfacial equilibria. Soapy objects like soap films and soap bubbles have been evoked, as well as the role of surfactant molecules with respect to their existence. Finally, we explained qualitatively how interfacial quantities such as surface elasticity and surface viscosity influence the global thinning of vertical soap films. We ended this chapter by proposing a non-exhaustive list of some recent experiments performed about vertical soap films. We then presented how our works include in the vertical soap film thematic.

Even if not fully understood, it is possible to characterize soapy objects by judicious experimental investigations, so that further experiments can be realized and partially interpreted. Such experiments often require typical times which are at least one order of temporal magnitude larger than the typical soap film lifetimes. In the second chapter, we proposed a method to maintain soap films over large timescales. Continuously feeding the films with their building solution proved to fit this goal. We showed that fed films present usual soap film behaviors on a relatively narrow flow range. We proposed a method, based on water infrared absorption, to characterize thickness profiles of such maintained films in the laminar flow regime. Those experiments allowed us to conclude that the thickness follows

a power law versus the vertical coordinate. Fits of averaged profiles corresponding to the different flow values emphasized that the exponent of the law remains almost unchanged in the considered flow range. This implies that the shape of our films do not change with the magnitude of the feeding flow. Beside this, the multiplicative constant of the power law was observed to increase with the flow rate. In other words, increasing the feeding inflates the films without changing their shape. This features should be related to the molecular dynamics between the bulk and interfaces of the film, as evoked in Chapter 1. Since we did not perform any studies about those molecular equilibria for our soap solutions, we were not able to model the thickness profiles as functions of surfactant-related quantities. Nevertheless, our thickness measurements have been considered as suited for characterizing the state of our soap films (i.e. their thickness profiles) without taking into account the physical chemistry at the interfaces. This result is of first importance with respect to the possibility to realize more complex experiments on soap film, as well as to build models in order to explain experimentally emphasized behaviors.

Mechanical considerations made in the late 1870's by Gibbs brought that soap film interfaces must exhibit vertical surface tension profiles in order to satisfy the mechanical equilibrium in the film. This assumption is, among other, a consequence of the vertical thickness profiles they exhibit. The third chapter was devoted to the description of an experiment aiming to measure those surface tension profiles. Recent works about soft material elasticity evidenced that capillary constraints may consequently deform those objects. We then imagine elastic objects which would deform when plugged in soap films, with the aim to relate their deformed shape to the corresponding surface tension values. This work was done in collaboration with José Bico and Benoit Roman from ESPCI in Paris. First, we applied typical surface compression to those objects, by the mean of controlled surface pressure of an ideal surfactant monolayer. Those preliminary tests were performed in order to validate the ability of our objects to deform under capillary constrains. A numerical solving of the elasticity equations faithfully reproduced those results. We then adapted those equations to the case of objects plugged in vertical soap films. The experiments showed that those objects exhibit very weak, but still optically accessible shape variations when moved along the vertical direction within our films. The relation between those deformations and the surface tension was then calibrated thanks to a numerical solving of the elasticity equations. Finally, the coupling between the experimental deformation and this numerical calibration allowed us to obtain surface tension profile measurements. The relatively poor accuracy of the method did not allowed us to extract the dependency of those profiles as functions of the feeding flow magnitude, as mechanical equilibrium and thickness profiles suggest. Nevertheless, we built a

simple model for surface tension profiles, involving the thickness measurements presented in the second chapter. This model revealed that the overall trend of surface tension profiles is in agreement with the concept of mechanical equilibrium within the films. Statistical considerations about both the thickness and the surface tension profiles included in our model underlined that both measurements are in agreement with the mechanical equilibrium in the film, as proposed by Gibbs in the late 1870's. To our knowledge, this is the first time that this idea is experimentally confirmed.

Being fluid objects, soap films are subject to present buoyancy phenomena. Marginal regeneration as been pointed out by Mysels and coworkers to be a spontaneous generation of buoyant film particles, originating in the menisci. Thickness differences have been identified as the source of those buoyancies and have been formalized using the bi-dimensional density of the film, defined as the product of the bulk density by the film thickness. This density appeared particularly well suited to express the typical buoyancy by taking into account those thickness differences. In the fourth chapter, we proposed to reconsider an experiment initially tested by Couder and coworkers in order to obtain insights on the behavior of buoyant particles as a function of experimental parameters such as the magnitude of the feeding flux. The experiment consists in introducing a very light ring in the film and then to burst the eventual soap film sustained by that ring. This burst modifies the total weight of the ring, leading to a net upward force. Since surface tension profiles have been characterized, we then wondered how they influence this driving force. Mechanical considerations including those profiles revealed that the surface tension forces acting on the ring are the origin of the buoyant forces in the film. We then proposed a model in order to reproduce the ring trajectories as a function of the ring radii and injected flow rates. Dynamical considerations brought that viscous friction and lubrication forces must be taken into account in order to faithfully predict the ring trajectories. The numerical data brought by our model are in quantitative agreement with the experimental measurements. In addition, this experiments confirms the validity of both thickness and surface tension measurements, since the related driving phenomena can equivalently be expressed in terms of these two profiles.

During the last decades, vertical soap films have been used as ideal bi-dimensional Rayleigh-Bénard cells, for the purpose of thermal turbulence experiments and theories. Applying vertical temperature differences to such films led to the turbulence of temperature, thickness and velocity profiles. Those turbulences have been associated with the apparition of thermal plumes as a consequence of the heating. These plumes are mushroom-shaped upward fluxes caused by density fluctuations engendered by the heating. We described in Chapter 5 an experiment aiming

to produce single thermal plumes. We designed a setup which allowed us to investigate the behavior of such plumes in our fed soap films as functions of the temperature difference and the feeding magnitudes. Using infrared imaging, we grasped the experimental features of the plumes versus time. A model for the rise of a heated film particle was then proposed, involving adapted global buoyancy described in Chapter 4. This model predicts the dynamics of the plumes. Numerical solving brought that rising times and equilibrium sizes of the plumes are quantitatively predicted by our model. As a consequence, the aspect ratios of the plumes with respect to the size of the tank were predicted. Always being smaller than unity, those aspect ratios have to be considered as a direct consequence of the soap film geometry, since the three dimensional analogs usually present aspect ratio equal to unity.

Perspectives

Following the considerations about the physical chemistry evoked in Chapter 1, the main perspective about our surfactant solution would be to analyze it into more details, i.e. to determine the kinds of micelles present in the bulk (sphere, sheets...), and what are their interactions with the interfaces (adsorption and/or disintegration at the interface). As emphasized in the conclusions of this first chapter, there may be technological lacks in such investigation methods. Nevertheless, techniques like small angle neutrons and X-ray scattering have already been successfully used in order to evidence the presence and the geometry of micelles in soapy solutions. Such experiments would be a first step in order to obtain further characterizations about the physical chemistry involved in our films. Note that it would be interesting to couple such measurements with simultaneous elasticity measurements, to possibly identify both consequences and effects of interfacial phenomena.

Still in the thematic of interfacial equilibria, such measurements would be useful in order to build models for the thickness profiles presented in Chapter 2. In fact, as mentioned in Chapter 1, soap film drainage must be regarded as a combination of fluid flow plus stretching of the film under its own weight. A precise knowledge of the elastic and viscous properties of the corresponding interfaces would certainly help in including those effects in a model for thickness profiles.

We proposed thickness measurements for our films, which are all built with the same solution. An interesting perspective would be to realize the same experiments with other mixtures. The influence of molecular interactions at the interface on the thickness profile behaviors would then be quantified. In addition, surface tension measurements could be realized as well, in order to verify the relevancy

of the mechanical equilibrium for various molecules. Note that both experiments have been tested with films made of SDS solution, without any success. Those experiments have revealed that it is almost impossible to build long-living fed soap films made of SDS thanks to our setup. Introduce any object in them also proved to be rather difficult. This result underlines that the solidity of the films strongly depends on the nature of the surfactant used to build them. Investigations of thickness and surface tension profiles with other molecules may then bring interesting results.

The thickness measurements were performed only with squared films. Experimental works have shown that soap film lifetimes can be considerably enlarged if the film is set in a cylindrical configuration [30]. It is believed that those larger lifetimes are due to the suppression of marginal regenerations along the lateral borders of the films. It would be interesting to couple those lifetime measurements with adapted thickness measurements, thanks to experimental setups such as presented in Figure 5.18. The idea is to create a cylindric box which would be closed by the presence of vertical soap film (i.e. the soap film is the lateral edge of the box). The inner cylindrical rod presented in Figure 5.18 could be heated, so that its infrared intensity is absorbed by the film.

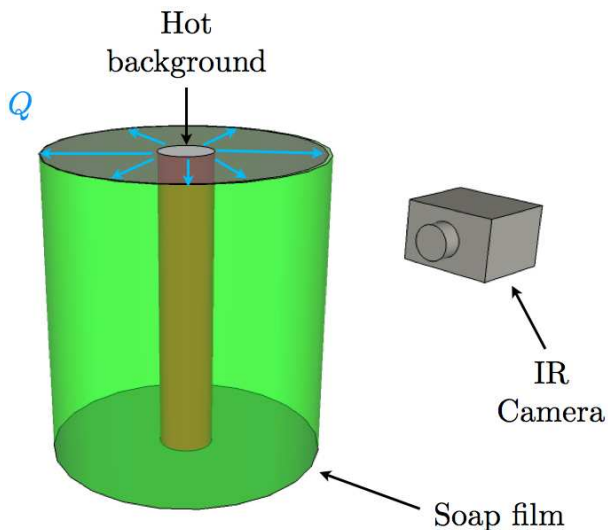


Figure 5.18: Sketch of the experimental setup to be used to perform thickness measurements in cylindrical soap films.

The feeding of the film would be ensured by the top of the box, by an overflowing technique similar to the one presented in Chapter 2. Note that either the top or

the bottom of the box must be mobile to allow the film initialization. A pressure valve (not represented in Fig. 5.18) would also be required to impose an inner pressure to the box. This pressure would prevent the film to adopt the natural catenoid shape usually exhibited when no pressure difference exists between the inside and the outside [1]. Free drainage cases could also be investigated, both in the planar and cylindrical configuration. Note that the surface tension profile in these cylindrical films could exclusively be deduced from the thickness profiles, since introducing an elastic ring such as presented in Chapter 4 would annihilate the pressure difference ensuring the cylindrical shape of the film.

The thermal plumes presented in Chapter 5 present several kinds of oscillations, being (i) oscillations of their size around their equilibrium size after growth and (ii) oscillations of the direction of the plume with respect to the gravity direction. As emphasized in Chapter 5, our model does not reproduce those oscillations. We believe that they are due to local parameter fluctuations after growth, coupled with collective effects regarded to the behavior of heated particles forming the plumes. A particular treatment of these effects would be required in order to link those size fluctuations to the experimental parameters. However, it is possible to realize preliminary investigations about those oscillatory behaviors. Von Karman streets developing in the wakes of cylindrical objects are known to be emitted at a frequency which depends on the velocity of the global flow. The Strouhal number is then used to describe the dependency of this frequency on the velocity of the flow. It reads [2] :

$$\text{Sr} = f \frac{d}{U}, \quad (5.21)$$

where f is the frequency at which the streets are emitted, d the size of the perturbative object and U the velocity of the global flow. This number is used to describe situations where f is proportional to U . Analyzing the frequencies linked to our thermal plumes lead to the curves presented in Figure 5.19. Those curves reveal that both the oscillations in size and direction present frequencies which are proportional to U , but characterized by different values of Sr. Even if not yet modeled, those results have to be considered as encouraging with respect to the plume oscillations phenomenology.

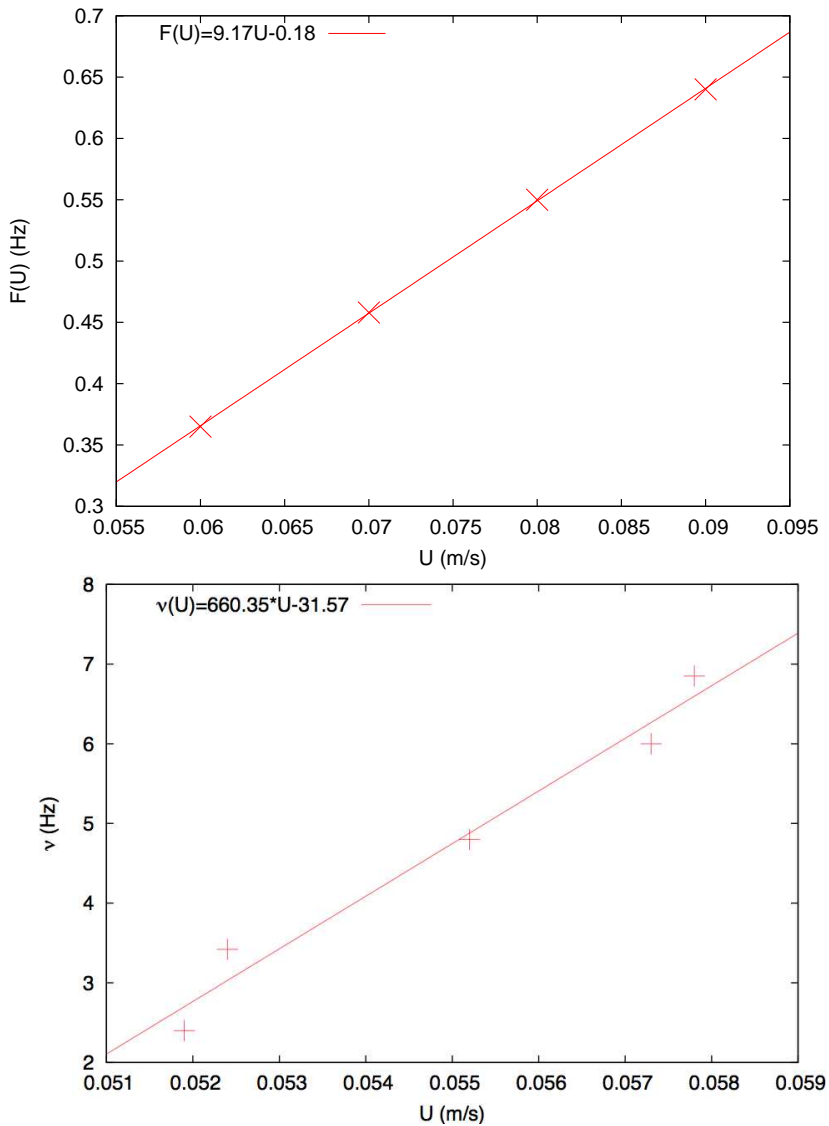


Figure 5.19: Top : frequency of the direction of the plume versus U . Bottom : frequency linked to $H(t)$ versus U .

As evoked in Chapter 5, it is impossible to measure the thickness and the position of hot rising film particles, due to their temperature. However, it is possible to create regenerated particles upward flows, such as presented in Figure 4.2 (i.e. some kind of “ambient temperature plumes”). Following the marginal regeneration phenomenon, those upward flow can be induced by creating menisci anywhere in a vertical film. This is actually what is done in Fig. 5.20.

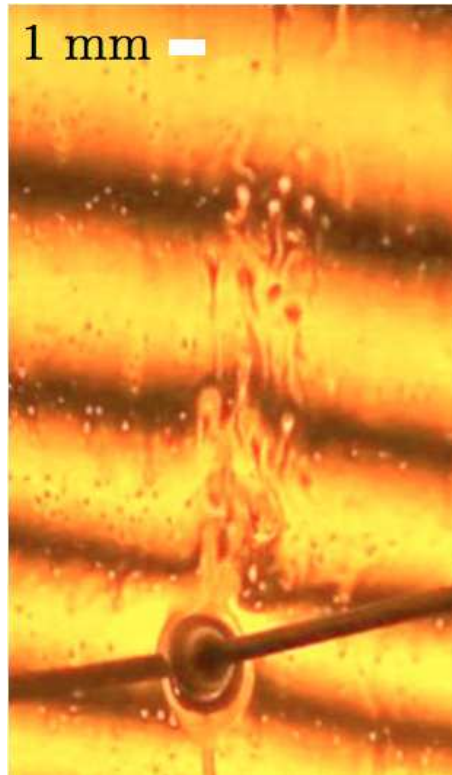


Figure 5.20: Generation of buoyant film particles by introduction of a perturbative object through the film interfaces.

Since the pressure difference between the meniscus and the bulk of the film is the motor of the marginal regeneration, we wondered if it is possible to avoid the marginal regeneration, i.e. if it is possible to introduce objects in the film without regenerating the film particles. We designed cylinders characterized by different height values e_P and a radius R . Introducing such objects into the film leads to the situations presented in Figure 5.21. If $e_P > e(H)$ a meniscus develops, which width is limited by e_P if e_P is smaller than the capillary length $l_c(H)$, and limited to $l_c(H)$ otherwise. Those cases are supposed to lead to marginal regeneration, since a meniscus exists between the film and the cylinder. In the particular case

where $e_P = e(H)$, there should be no meniscus, since the film cannot spread on the cylinder on a size larger than its local thickness. If $e_P < e(H)$ the film is assumed to present an inverse meniscus such as presented in Fig. 5.21, right. This latter case is particular in the sense that it imposes a thickness to the film, which is smaller than its local thickness value. This local condition on the film thickness creates film elements which are thinner than the film elements which are located right above the linking region. It is rather difficult to know what the marginal regeneration phenomenon becomes in that context. However, the cylinder tends to generate thin particles, which could then become buoyant if released from the linking region. Even if still hypothetical, this latter situation would generate naturally buoyant film particles which are created by an intrusive object but without marginal regeneration.

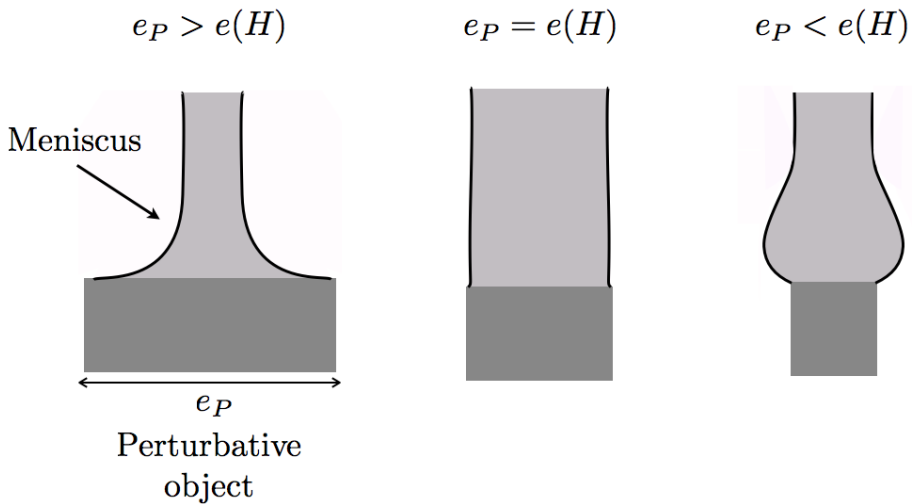


Figure 5.21: Schematics of the different menisci generated in the film as a function of the height e_P of the perturbative cylinder. Left : $e_P > e(H)$, the meniscus is fully developed with a width limited by e_P if $e_P < l_c(H)$ and equal to $l_c(H)$ if $e_P \geq l_c(H)$. Center : $e_P = e(H)$, no meniscus should be created by the cylinder. Right : $e_P < e(H)$, some kind of inverse meniscus is assumed to be created to link the cylinder to the film.

This experiment can easily be realized in our maintained soap films. A few early results are shown in Figure 5.22. This figure shows that the maximum height reached by the buoyant thin particles, H^* , decreases when e_P becomes smaller than the typical capillary length of our solution ($l_c \sim 1.7$ mm). This is rather expected because the meniscus is not fully developed in that range, so that the corresponding pressure gradient is supposed to be weaker than for fully developed

menisci. The Rhodoïd-2mm, Rhodoïd-6mm and Aluminum sheet cylinders correspond to the weaker thicknesses, being $9.1 \mu\text{m}$ and $1.3 \mu\text{m}$, respectively. Even if their thickness is close to the one of the film, those latter object still generate buoyant particles in the film. This might be because their thickness is still too important to suppress marginal regeneration (Rhodoïd) or weaker than the film thickness (Aluminum). It is difficult to conclude on the possibility to annihilate the marginal regeneration from these data. Nevertheless, the fact that H^* tends to decrease as ϵ_P is decreased and then to re-increase if further decrease of ϵ_P is applied suggests that a minimum should exist for the efficiency the perturbative cylinder to generate buoyant particles in the film. Further investigations are needed in order to confirm this trend. The results presented in Figure 5.22 must be considered as encouraging with respect to the basic idea sustained by the experiment.

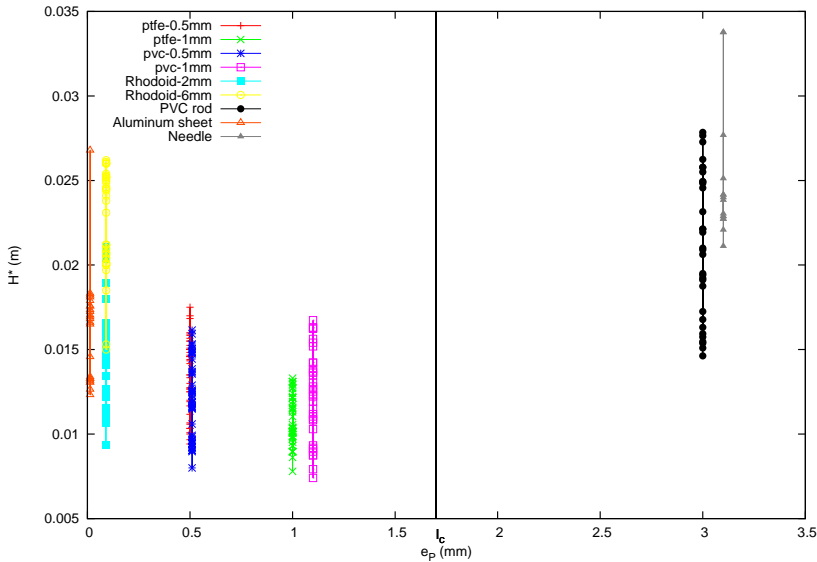


Figure 5.22: Critical height H^* reached by the regenerated particles as a function of the thickness of the perturbative object. The figures in the key refer to the diameter of the cylinder. The straight vertical line is a guide for the eye, illustrating the value of the capillary length linked to our SLES+CAPB solution (~ 1.7 mm).

Bibliography

- [1] P.-G. De Gennes, F. Brochard-Wyart, D. Quéré, *Gouttes, bulles, perles et ondes* (Belin, Paris, 2002).
- [2] E. Guyon, J.-P. Hulin, L. Petit, *Hydrodynamique physique* (cnrs éditions savoirs actuels, Paris, 2001).
- [3] F. Charru, *Instabilités hydrodynamiques* (cnrs éditions, savoirs actuels, Paris, 2007).
- [4] R. A. Serway, *Physics for scientists and engineers*, 9th edition (Cengage Learning, Boston, 2013).
- [5] F. S. Crawford, *Waves, Berkeley physics course, volume 3* (McGraw-Hill book company, Newton, 1968).
- [6] P. Atkins, J. de Paula, *Physical Chemistry*, 8th edition (W. H. Freeman, New York, 2006).
- [7] J. Drelich, C. Fang, C. L. White, *Measurement of interfacial tension in fluid systems* (Encyclopedia of Surface and Colloid Science, Houghton, 2002).
- [8] L. Wilhelmy, *Ann. Phys. Chem.* **4**, 177 (1863).
- [9] K. Huang, *Statistical mechanics*, 2nd edition (John Wiley & sons, New York, 1987).
- [10] D. Myers, *Surfactant science and technologies*, 3rd edition (John Wiley & Sons, Hoboken, 2006).
- [11] K. Tsujii, *Surface activity : principles, phenomena and applications* (Academic press, San Diego, 1998).
- [12] K. S. Birdi, *Handbook of surface and colloid chemistry* (CRC press, Boca Raton, 2009).

- [13] I. Cantat, S. Cohen-Addad, F. Elias, F. Graner, R. Höhler, O. Pitois, F. Rouyer, A. Saint-Jalmes, *Les mousses : structure et dynamique* (Belin, Paris, 2010).
- [14] K. Golemanov, N. D. Denkov, S. Tcholakova, M. Vethamuthu, A. Lips, *Langmuir* **24**, 9956 (2008).
- [15] Y. Couder, J.-M. Chomaz, M. Rabaud, *Physica D* **37**, 384 (1989).
- [16] I. Langmuir, V. J. Schaefer, *J. Am. Chem. Soc.* **59**, 10 (1937).
- [17] V. M. Kaganer, H. Möhwald, P. Dutta, *Rev. Mod. Phys.* **71**, 3 (1999).
- [18] S. Mehan, A. J. Chinchalikar, S. Kumar, V. K. Aswal, R. Schweins, *Langmuir* **29**, 11290 (2013).
- [19] C. S. Vassilieff, B. N. Nickolova, E. D. Manev, *Coll. Pol. Sci.* **286**, 475 (2008).
- [20] K. D. Danov, P. A. Kralchevsky, K. P. Ananthapadmanabhan, A. Lips, *Col. Surf. A* **282**, 143 (2006).
- [21] B. A. Noskov, *Adv. Col. Int. Sci.* **95**, 237 (2002).
- [22] J. Lucassen, *Faraday Discuss. Chem. Soc.* **59**, 76 (1975).
- [23] C. M. Knobler, R. C. Desai, *Ann. Rev. Phys. Chem.* **43**, 207 (1992).
- [24] S. L. Duncan, I. S. Dalal, R. G. Larson, *Biochim & Biophys. Acta* **1808**, 2450 (2011).
- [25] E. Ruckenstein, B. Li, *J. Phys. Chem.* **100**, 3108 (1996).
- [26] E. H. Lucassen-Reynders, A. Cagna, J. Lucassen, *Col. Surf. A* **186**, 63 (2001).
- [27] J. Lucassen, M. Van Den Tempel, *Chem. Ing. Sci.* **27**, 1283 (1972).
- [28] S. Sett, S. Sinha-Ray, A. L. Yarin, *Langmuir* **29**, 4934 (2013).
- [29] J. Meunier, L. T. Lee, *Langmuir* **7**, 1855 (1991).
- [30] K. Mysels, K. Shinoda, S. Frankel, *Soap Films* (Pergamon press, London, 1959).
- [31] L. Saulnier, F. Restagno, J. Delacotte, D. Langevin, E. Rio, *Langmuir* **27**, 13406 (2011).

- [32] F. Seychelles, Y. Amarouchene, M. Bessafi, H. Kellay, *Phys. Rev. Lett.* **100**, 144501 (2008).
- [33] L. E. Scriven, *Chem. Eng. Sci.* **12**, 98 (1960).
- [34] S. Naire, J. Braun, *Phys. Fluids* **13**, 9 (2001).
- [35] E. A. Van Nierop, B. Scheid, H. A. Stone, *J. Fluid Mech.* **602**, 119 (2008).
- [36] B. Scheid, S. Dorbolo, L. R. Arriaga, E. Rio, *Phys. Rev. Lett.* **109**, 264502 (2012).
- [37] J. T. Petkov, K. D. Danov, N. D. Denkov, *Langmuir* **12**, 2650 (1996).
- [38] C. Barentin, C. Ybert, J.-M. Di Meglio, J.-F. Joanny, *J. Fluid Mech.* **397**, 331 (1999).
- [39] J. Plateau, *Statique expérimentale et théorique des liquides soumis aux seules forces moléculaires* (Gauthier-Villars, Paris, 1873).
- [40] D. Weaire, S. Hutzler, *The physics of foams* (Clarendon press, Oxford, 1999).
- [41] V. A. Nierstrasz, G. Frens, *J. Col. Int. Sci.* **215**, 6226 (1999).
- [42] V. A. Nierstrasz, G. Frens, *J. Col. Int. Sci.* **207**, 209 (1998).
- [43] A. A. Aradian, *Quelques problèmes de dynamique d'interfaces molles*, thèse de doctorat, université de Paris 6, 2001.
- [44] N. Adami, H. Caps, arXiv:1310.0320 [physics.flu-dyn].
- [45] H. Kellay, X. I. Wu, W. I. Goldburg, *Phys. Rev. Lett.* **74**, 3975 (1995).
- [46] H. Kellay, W. I. Goldburg, *Rep. Prog. Phys.* **65**, 845 (2002).
- [47] W. I. Goldburg, A. Belmonte, X. L. Wu, I. Zusman, *Physica A* **254**, 231 (1998).
- [48] H. Kellay, X. L. Wu, W. I. Goldburg, *Phys. Rev. Lett.* **80**, 277 (1998).
- [49] B. K. Martin, X. L. Wu, W. I. Goldburg, M. A. Rutgers, *Phys. Rev. Lett.* **80**, 3964 (1998).
- [50] W. I. Goldburg, M. A. Rutgers, X. L. Wu, *Physica A* **239**, 340 (1997).
- [51] M. A. Rutgers, X. L. Wu, W. I. Goldburg, *Phys. Fluids* **8**, S7 (1996).
- [52] M. Rivera, P. Vorobieff, R. E. Ecke, *Phys. Rev. Lett.* **81**, 1417 (1998).

- [53] M. Lesieur, *Turbulence in fluids*, 4th edition (Springer, Dordrecht, 2008).
- [54] X. L. Wu, R. Levine, M. A. Rutgers, H. Kellay, W. I. Goldburg, *Rev. Sci. Instr.* **72**, 5 (2001).
- [55] J. Zhang, X. L. Wu, N. Rashidnia, *Phys. Fluids* **18**, 085110 (2006).
- [56] J. Zhang, X. L. Wu, K. Q. Xia, *Phys. Rev. Lett.* **94**, 174503 (2005).
- [57] B. Martin, X. L. Wu, *Phys. Rev. Lett.* **80**, 1892 (1998).
- [58] J. Q. Zhong, J. Zhang, *Phys. Rev. E* **76**, 016307 (2007).
- [59] M. Winkler, G. Kofod, R. Krastev, S. Stökle, M. Abel, *Phys. Rev. Lett.* **110**, 094501 (2013).
- [60] S. Alben, M. Shelley, J. Zhang, *Nature* **420**, 479 (2002).
- [61] M. J. Shelley, J. Zhang, *Ann. Rev. Fluid Mech.* **43**, 449 (2011).
- [62] L. W. Schwartz, R. V. Roy, *J. Col. Int. Sci.* **218**, 309 (1999).
- [63] M. Fermigier, *Hydrodynamique physique : problèmes résolus avec rappels de cours* (Dunod, Paris, 1999).
- [64] S. T. Tobin, A. J. Meagher, B. Bulfin, M. Möbius, S. Hutzler, *Am. J. Phys.* **79**, 8 (2011).
- [65] F. Elias, J. C. Barci, C. Flament, E. Janiaud, D. Talbot, W. Drenchkan, S. Hutzler, D. Weaire, *J. Col. Surf.* **263**, 65 (2005).
- [66] D. E. Moulton, J. Lega, *Physica D* **238**, 2153 (2009).
- [67] O. Bonhomme, O. Liot, A. L. Biance, L. Bocquet, *Phys. Rev. Lett.* **110**, 054502 (2013).
- [68] R. C. Ernst, C. H. Watkins, H. H. Ruwe, *J. Phys. Chem.* **40**, 5 (1936).
- [69] N. Le Grand-Piteira, P. Brunet, L. Lebon, L. Limat, *Phys. Rev. E* **74**, 026305 (2005).
- [70] J. S. Roche, N. Le Grand, P. Brunet, L. Lebon, L. Limat, *Phys. Fluids* **18**, 082101 (2006).
- [71] P. Brunet, J. M. Fesselles, L. Limat, *Eur. Phys. J. B* **55**, 297 (2007).
- [72] P. Brunet, *Structure et dynamique non-linéaire de liquides tombants*, thèse de doctorat, Université Paris 6, 2002.

- [73] O. Krichevsky, J. Stavans, Phys. Rev. Lett. **74**, 14 (1995).
- [74] O. Krichevsky, J. Stavans, Phys. Rev. E **55**, 6 (1997).
- [75] V. Greco, G. Molesini, Meas. Sci. Tech. **7**, 96 (1996).
- [76] P. D. Huibers, D. O. Shah, Langmuir **13**, 5995 (1997).
- [77] G. Ropars, D. Chauvat, A. Le Floch, App. Phys. Lett. **88**, 234104 (2006).
- [78] S. Berg, E. A. Adelizzi, S. M. Troian, Langmuir **21**, 3867 (2005).
- [79] A. W. Reinold, Nature **48**, 624 (1893).
- [80] A. Saint-Jalmes, D. Langevin, J. Cond. Mat. **14**, 9397 (2002).
- [81] FLIR ThermovisionTM 160 user's guide.
- [82] G. M. Hale, M. R. Querry, Appl. Opt. **12**, 555 (1973).
- [83] J. W. Gibbs, *The collected works* (Longmans Green, New York, 1931).
- [84] N. Adami, H. Caps, arXiv:1310.0454 [physics.flu-dyn cond-mat.soft].
- [85] J. Bico, B. Roman, L. Moulin, A. Boudaoud, Nature **432**, 690 (2004).
- [86] A. Boudaoud, J. Bico, B. Roman, Phys. Rev. E **76**, 060102 (2007).
- [87] T. Cambau, J. Bico, E. Reyssat, Eur. Phys. J. **96**, 24001 (2011).
- [88] F. Choidi, B. Roman, J. Bico, Europhys. Lett. **90**, 44006 (2010).
- [89] E. de Langre, C. N. Baroud, P. Reverdy, J. Fluid. Struct. **26**, 205 (2010).
- [90] J. B. Grotberg, O. E. Jensen, Ann. Rev. Flu. Mech. **36**, 121 (2004).
- [91] Y. Hu, K. Y. Lee, J. Israelachvili, Langmuir **19**, 100 (2003).
- [92] J. Hure, B. Roman, J. Bico, Phys. Rev. Lett. **106**, 174301 (2011).
- [93] S. Neukrich, B. Roman, B. de Gaudemaris, J. Bico, J. Mech. Phys. Sol. **55**, 1212 (2007).
- [94] M. Pineirua, B. Roman, J. Bico, Soft Matter **6**, 4491 (2010).
- [95] C. Py, P Reverdy, L. Doppler, J. Bico, B. Roman, C. N. Baroud, Phys. Rev. Lett. **98**, 156103 (2007).
- [96] C. Py, P Reverdy, L. Doppler, J. Bico, B. Roman, C. N. Baroud, Eur. Phys J. **166**, 67 (2009).

- [97] B. Roman, J. Bico, *J. Phys. Cond. Matt.* **22**, 493101 (2010).
- [98] Y. Yang, Y. F. Gao, D. Y. Sun, M. Asta, J. J. Hoyt, *Phys. Rev. B* **81**, 241407 (2010).
- [99] Z. A. Zell, S. Q. Choi, L. G. Leal, T. M. Squires, *App. Phys. Lett.* **97**, 133505 (2010).
- [100] A. A. Evans, S. E. Spagnolie, D. Bartolo, E. Lauga, *Soft Matter* **9**, 1711 (2013).
- [101] L. D. Landau, E. M. Lifshitz, *Theory of elasticity*, 3rd edition (Butterworth-Heinemann, Oxford, 1986).
- [102] S. Timoshenko, J. N. Goodier, *Theory of elasticity* (McGraw-Hill book company, New-York, 1951).
- [103] A. N. Gent, *Trans. Inst. Rubber Ind.* **34**, 46 (1958).
- [104] A. W. Mix, A. J. Giacomin, *J. Test. Eval.* **39**, 1 (2011).
- [105] P. S. Raux, P. M. Reis, J. W. M. Bush, C. Clanet, *Phys. Rev. Lett.* **105**, 044301 (2010).
- [106] N. Adami, A. Delbos, B. Roman, J. Bico, arXiv:1310.0329 [physics.flu-dyn].
- [107] R. Bruinsma, *Physica A* **216**, 59 (1995).
- [108] N. Adami, S. Dorbolo, H. Caps, *Phys. Rev. E* **84**, 046316 (2011).
- [109] C. V. Boys, *Soap bubbles and forces which mould them* (Anchor Books, New York, 1959).
- [110] G. G. Fuller, *Rheology Review* 2007, 77.
- [111] M. C. Rogers, S. W. Morris, *Phys. Rev. Lett.* **95**, 24505 (2005).
- [112] J. S. Turner, *Buoyancy effects in fluids* (Cambridge university press, Cambridge, 1973).
- [113] E. Moses, G. Zocchi, A. Libchaber, *J. Fluid Mech.* **251**, 581 (1993).
- [114] B. R. Morton, G. Taylor, J. S. Turner, *Proc. Roy. Soc. A* **234**, 1 (1956).
- [115] A. T. Ismail-Zadeh, A. I. Korotkii, D. P. Krupsky, I. A. Tsepelev, G. Schubert, *Dokl. Earth Sci.* **411**, 1442 (2006)
- [116] S. Zhong, *Geo. J. Int.* **162**, 289 (2005).